

Interfacial Phenomena in Adhesion and Adhesive Bonding Investigated by Electron Microscopy



Shin Horiuchi

Abstract Using electron microscopy techniques described in Chap. 2, we investigate interfacial phenomena in adhesion and adhesive bonding. Polymer–polymer interfaces formed via interdiffusion are visualized and characterized by EFTEM. Fractographic studies using high-resolution SEM investigate entanglements at the polymer–polymer interfaces, and the adhesion mechanism is discussed about the interfacial entanglements. The effect of surface treatments of polymers for adhesion improvement is studied in terms of the surface roughness and the chemical functionality of the adherend created by the surface pretreatments. We then describe the role of chemical interactions between polymers and metals on bonding by the analysis of fracture surfaces by the STEM-replica technique. Bonding mechanisms of adhesive bonding and recently developed direct bonding of metal and plastic are also investigated by STEM-EELS/ELNES and STEM-tomography. Finally, we evaluate the toughness and durability of adhesive joints between metal and carbon fiber reinforced plastics (CFRP) and discuss the durability of the adhesive bonding.

Keywords Adhesion · Bonding · Interface · Diffusion · Entanglement · Fracture · Electron microscopy · EELS · EDX · Tomography

Supplementary Information The online version contains supplementary material available at https://doi.org/10.1007/978-981-99-4456-9_3. The videos can be accessed individually by clicking the DOI link in the accompanying figure caption or by scanning this link with the SN More Media App.

S. Horiuchi (✉)

Research Laboratory for Adhesion and Interfacial Phenomena (AIRL), National Institute of Advanced Industrial Science and Technology (AIST), 1-1-1, Higashi, Tsukuba 305-8565, Ibaraki, Japan

e-mail: s.horiuchi@aist.go.jp

© The Author(s) 2024

S. Horiuchi et al. (eds.), *Interfacial Phenomena in Adhesion and Adhesive Bonding*, https://doi.org/10.1007/978-981-99-4456-9_3

1 Visualization of Homopolymer/Random Copolymer Interfaces by EFTEM

Polymer interdiffusion is important for both fundamental research [1–3] and practical applications, such as adhesion, welding, coating, and laminated films. The success of these applications depends on the interfacial layer's entanglement structure formed via inter-chain penetration during the interdiffusion process. Although Transmission Electron Microscopy (TEM) is a potential tool for polymer material morphology characterization, it requires heavy metal staining to obtain sufficient phase contrasts due to the low yields of elastically scattered electrons in organic polymer specimens. However, heavy metal staining may alter the original structure. Therefore, an alternative technique with high spatial resolution, real space observation, non-toxic preprocessing, and no limitations on specimen geometry could be a promising approach to studying polymer interdiffusion.

We employ energy-filtering transmission electron microscopy (EFTEM) for the development of advanced applications of TEM for the investigation of polymer structures. Interfaces formed via diffusion of dissimilar polymers were characterized by transmission electron microscopy (TEM) equipped with an imaging filter [4–7]. A type of microscope known as Energy Filtering TEM (EFTEM) allows for the acquisition of images showing the two-dimensional intensity distribution of inelastically scattered electrons within a given energy-loss range [8]. This Electron Spectroscopic Imaging (ESI) technique allows for mapping chemical elements with almost the same resolution as TEM.

In this study, we examine the adhesion and interfaces created between poly(methyl methacrylate) (PMMA) and styrene-acrylonitrile random copolymers (SAN). This system helps explore the correlation between adhesion and interfacial thickness because the miscibility between PMMA and SAN can be adjusted by the acrylonitrile (AN) content in SAN. The “repulsive effect” of random copolymers, which causes highly favorable interactions between its blends with homopolymers, affects the miscibility of blends with homopolymers. SAN possesses positive and negative interaction parameters, χ , depending on the AN content in SAN [9]. Flory–Huggins χ parameter describes the excess free energy of mixing and governs phase behaviors of polymer blends. The χ parameter of homopolymer (A)/random copolymer (B) blends, where copolymer B is composed of monomers C and D, is expressed by Eq. (1), where φ is the composition of homopolymer A. The high segmental repulsive effect in the random copolymer, which gives a high positive χ_{CD} , results in a negative χ_{AB} value.

$$x_{AB} = \varphi x_{AC} + (1 - \varphi)x_{AD} - \varphi(1 - \varphi)x_{CD}. \quad (1)$$

Figure 1a shows the χ_{AB} values as a function of AN content in SAN calculated by three groups, indicating that PMMA is miscible with SAN containing 10–35 wt% AN [9, 10]. Figure 1b is a phase diagram of the blend of PMMA and SAN with 33 wt% AN content, showing a lower critical solution temperature (LCST)-type phase diagram [11]. Thus, various interfacial situations can be created by adjusting the SAN composition and annealing temperature in this system. EFTEM is employed to visualize the interfacial formations between PMMA/SAN while varying the AN content in SAN. The PMMA and SAN plates were prepared by compression molding between silicon wafers at 150 °C to create smooth-surfaced sheets. The PMMA/SAN laminates were annealed in the air under slight pressure at 140 °C for 2 h to ensure contact between the plates. After the specimens were quenched to room temperature to terminate the interdiffusion, they were cut into thin sections of approximately 50 nm thickness perpendicularly to the interface using ultramicrotomy. To aid in focus adjustment during TEM operation and drift correction for element mapping, 10 nm diameter gold nanoparticles were spread onto the thin sections by dropping a thin gold colloid solution onto them.

To perform the imaging and spectral recording, we use an in-column energy-filtering transmission electron microscope with a LaB₆ cathode and an Omega-type energy filter at an accelerating voltage of 200 keV. A 2 K × 2 K slow-scan CCD camera records the energy-filtered images and ELES spectra, and 512 × 512-pixel images are acquired by summing up 4 × 4 pixels into one effective pixel to gain sensitivity. All observations are performed cryogenically at 120 K to minimize radiation damage to the specimens.

This study aims to generate high spatial-resolution oxygen and nitrogen maps. When two polymers are thermodynamically immiscible, their interface has a thickness in the nanometer range. To examine such thin interfaces using EFTEM,

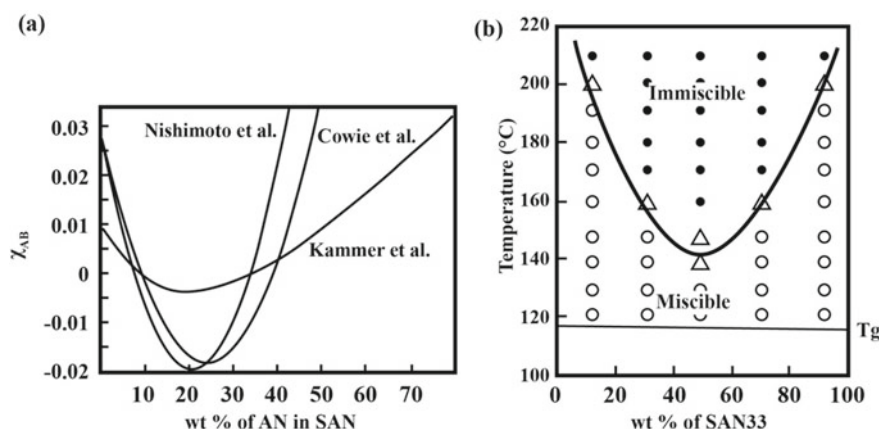


Fig. 1 AN content dependence of χ parameter of PMMA/SAN blends (a) and phase diagram of PMMA/SAN33 (b)

improving the spatial resolution and quantitiveness of elemental maps is necessary. Image-EELS techniques and elemental mapping to visualize the interfaces are used for that purpose. Elemental mapping relies on the fact that each core-loss edge of an EELS spectrum occurs at an energy characteristic of a particular chemical element. Extracting elemental information for mapping requires separation from the background (BG), which is superimposed on the core-loss edge due to plural scattering. The two-window and three-window methods are utilized to calculate the BG components [12]. In the three-window process, the BG curve is estimated by assuming power law (2) or exponential law (3) dependences using the two energy windows (E_1 and E_2), where the factors A and r are calculated pixel by pixel from the signals $S(E_1)$ and $S(E_2)$.

Power law

$$S(E) = A \cdot E^{-r} \quad (2)$$

Exponential law

$$S(E) = A \cdot \exp(-r \cdot E) \quad (3)$$

In this study, we perform Image-EELS to obtain EELS spectra from small areas with arbitrary shapes and locations in an image [7, 13–15]. As illustrated in Fig. 2, tens of energy-filtered images are recorded sequentially across a broad energy loss range to build a three-dimensional dataset containing spatial information $I(x, y)$, acquired in parallel, and spectral information $I(E)$, which is recorded serially. The average gray values of the same pixels are calculated in each energy-filtered image across the whole range of acquired images, giving an EELS spectrum from a chosen region in the image. A typical condition for Image-EELS is an energy width of 5 eV and an energy increment of 4 eV. A series of energy-filtered images sequentially across a broad energy loss range is taken with such a condition. The images are acquired, for example, with magnification at 50,000 and the acquisition time for each image of 5 s. These images are stacked and extracted the intensities at the same pixel in each image across the series to construct an EELS spectrum by plotting the intensities against the corresponding energy loss values. To correct the drift of the specimen, the individual images have to be shifted pixelwise over the entire acquired images.

To enhance the quality of elemental maps, it is essential to increase the signal-to-noise ratio (SNR). A method to achieve this is by utilizing the three-window approach, which involves selecting suitable widths and energetic positions for elemental mapping. In this particular investigation, Image-EELS is utilized to pick energy windows and background fitting methods for elemental maps that covered the nitrogen and oxygen K-edges. The interfacial region of the PMMA/SAN laminate is imaged by applying an energy loss range of 350–600 eV, while the zero-loss image, which lacks specific features and has low contrast, is not suitable for focus adjustment. Instead, the focus can be adjusted on gold nanoparticles located outside of the interfacial region to avoid damage from radiation. EELS spectra are generated

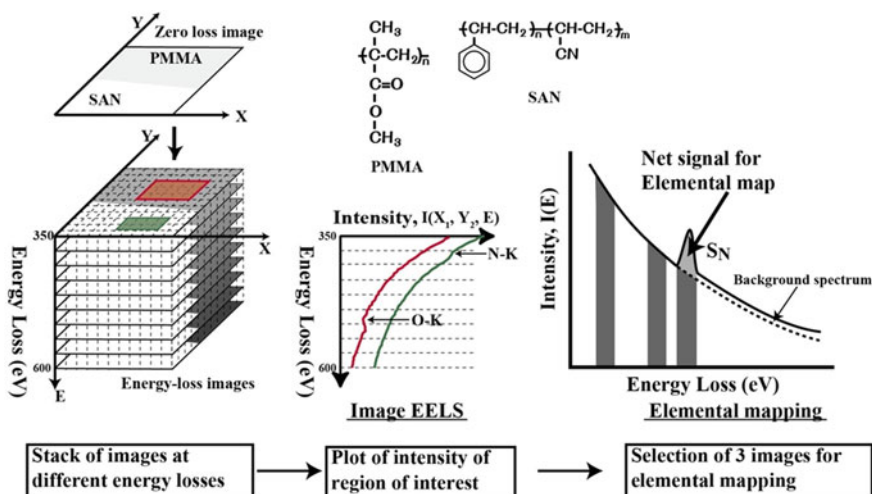


Fig. 2 The procedure for the creation of EELS spectra and elemental maps from the stack of energy-filtered images by Image-EELS

from the PMMA and the SAN regions by utilizing a series of images collected using Image-EELS. The nitrogen and oxygen ionization edges are noticeable at approximately 400 and 530 eV, respectively. Based on these spectra, energy windows for the core-loss image and background images for curve fittings can be determined appropriately. As illustrated in Fig. 3b, the exponential law is more effective in fitting the background curves compared to the power law.

Figure 3c and d display the nitrogen maps generated using the two-window and three-window methods, respectively. The two-window method provides a nitrogen map with better clarity and higher SNR than the three-window method. This is due to the higher statistical fluctuation of inelastically scattered images compared to elastically scattered images, as inelastic scattering has a lower cross section. However, in the nitrogen map produced by the two-window method, the gold nanoparticles are still present, whereas they are eliminated in the nitrogen map created using the three-window method. This inaccuracy in the two-window map can be attributed to the dissimilar slopes of the background curves for the polymer and the gold nanoparticles. In contrast, the three-window method computes the background curves on a pixel-by-pixel basis, which accurately subtracts the background contribution from the core-loss image. Therefore, for precise elemental mapping analysis, the three-window method should be utilized. Additionally, the successful removal of 10 nm gold nanoparticles in the elemental map confirms that the map has a spatial resolution exceeding 10 nm.

A range of energy-filtered images is taken from the region around the interface of the sample that is annealed for 2 h at 140 °C, with energy losses ranging from 350 to 600 eV. Next, spectra are extracted from the areas with 10 nm in diameter

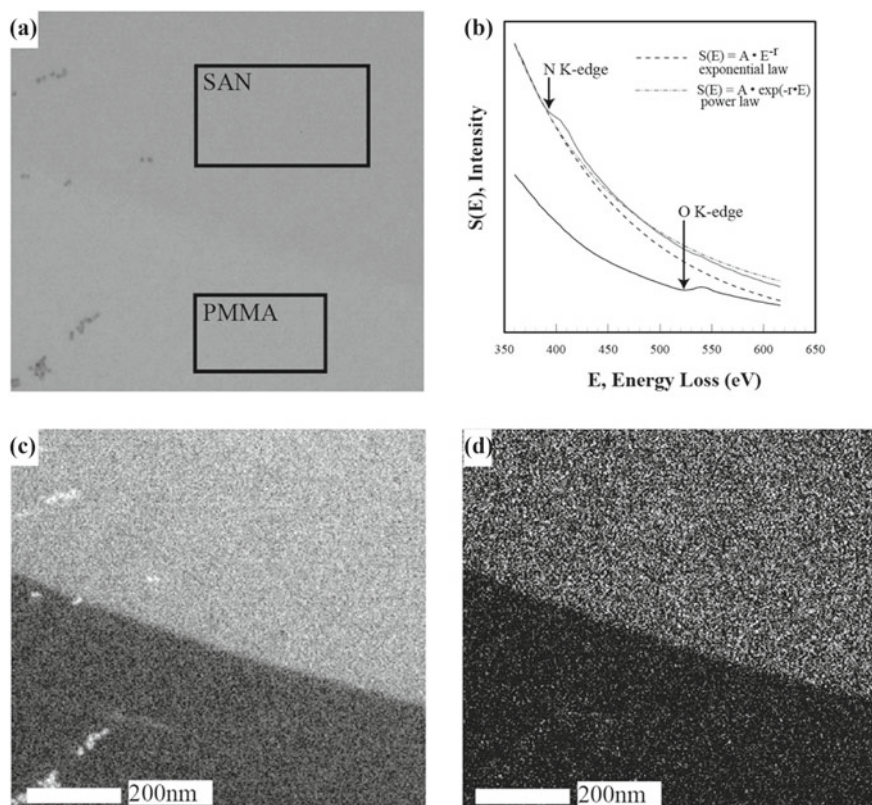


Fig. 3 Zero-loss image of the PMMA/SAN laminate annealed at 160 °C (a) and Image-EELS spectra (b) obtained from the regions shown in (a) with BG fitting curves for the nitrogen K-edge calculated by the exponential and power laws (b). Nitrogen maps created by the two-window (c) and the three-window exponential (d) methods. Reprinted with permission from [16]. Copyright 2005 John Wiley & Sons. All Rights Reserved

arranged across the interface, as presented in Fig. 4a. The nitrogen and oxygen K-edges are observed in areas 2 and 4, respectively, from which spectroscopy analysis of the interfacial region is performed with a spatial resolution exceeding 10 nm. In Fig. 4b, the nitrogen and oxygen K-edges are displayed after curve fitting based on the exponential law and background (BG) intensity subtraction. The width of the region where both polymers coexist was estimated to be approximately 65 nm.

In the next step, the interfacial regions are analyzed by elemental mapping—three suitable images for nitrogen and oxygen maps from the stack of energy-filtered images obtained by Image EELS. The energy windows, including the nitrogen and oxygen ionization edges, are chosen from the spectra and the BG fitting method. We select one pre-edge image close to the ionization edges and another with a broad energy range for a safer fit. An energy window for the core-loss image is determined to yield a high signal-to-noise ratio (SNR) elemental map. The concept

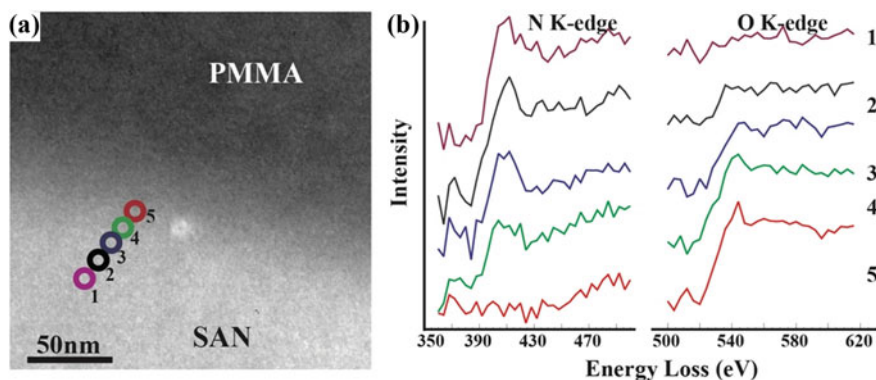


Fig. 4 Structure-sensitive image at 250 ± 10 eV energy loss of the PMMA/SAN laminate annealed at 140°C (a). Image-EELS spectra of the nitrogen and the oxygen K-edges after subtracting the BG contributions (b) acquired from the regions marked in (a). Reprinted with permission from [16]. Copyright 2005 John Wiley & Sons. All Rights Reserved

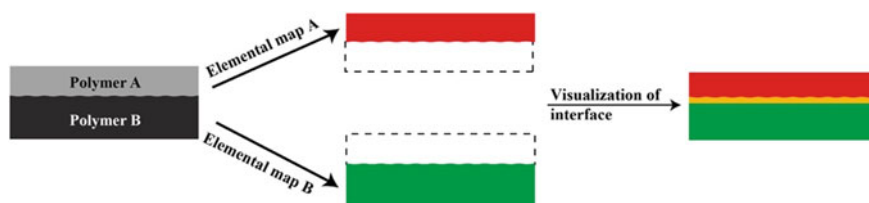


Fig. 5 Visualization of an interface by the simple RGB technique with two elemental maps

for the visualization of an interface is shown in Fig. 5. Using the RGB (red–green–blue) method, one of the basic color components represents the nitrogen map (green). In contrast, the oxygen map is represented in red. Combining the two maps displays the interfacial area as yellow due to the overlap of green and red pixels.

Figure 6's top section displays the RGB-composition images formed from the nitrogen (red) and oxygen (green) maps of the lamination of PMMA and SAN with varying AN content. Figure 6a, b and c correspond to the laminations containing 29, 34, and 40 wt% AN contents, respectively. The intensity profiles along the lanes highlighted in the maps are presented underneath their corresponding images (middle part). These profiles show the intensity variations in the nitrogen and oxygen maps across the interfaces and their ratios (O/N). The images and the profiles reveal that the interfacial width increased as the AN content decreased. Using Image-EELS, EELS spectra are generated from the spots on the interfacial regions. The nitrogen and oxygen core-loss peaks obtained after the background subtraction are shown in the bottom part. The intensity of the nitrogen core-loss peaks gradually decreases from left to right in their images, whereas the opposite trend is seen for the oxygen core-loss peaks. This result confirms that the pixel intensities in the elemental maps

represent the elemental concentrations. Although the two original intensity profiles are noisy and fluctuating, smooth curves with reduced noises are obtained from their ratios. These ratios allow us to estimate the interfacial widths: approximately 130, 50, and 20 nm for SAN29, 34, and 40, respectively. This finding indicates that the fluctuation in the original profiles of the specimens is due to variations in the specimen thickness.

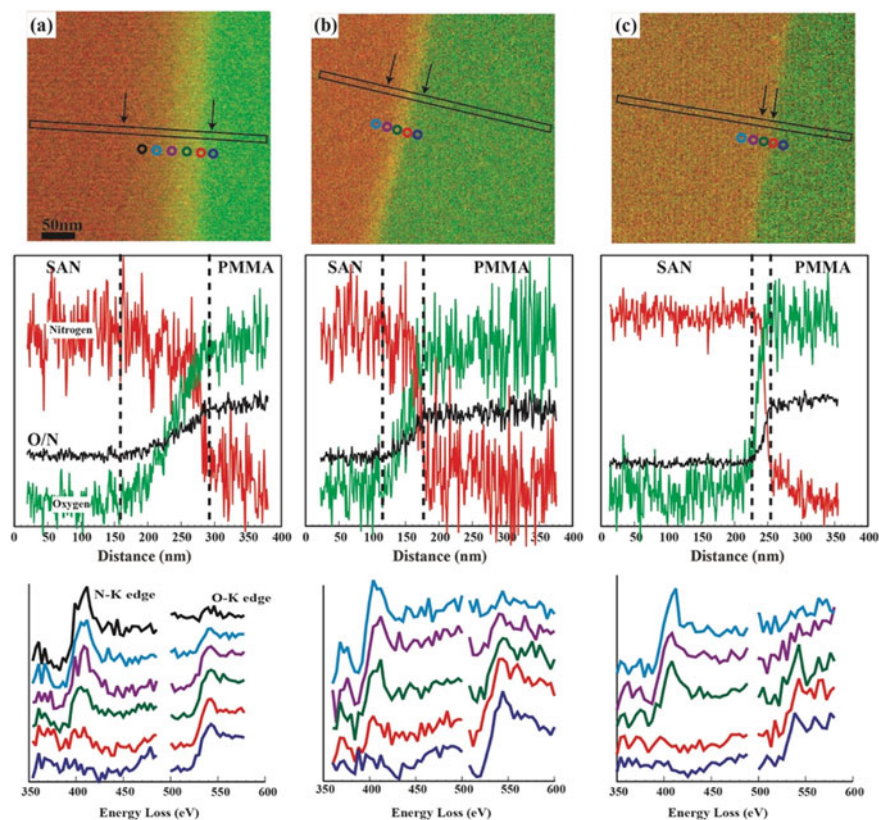


Fig. 6 Results of EFTEM analyses of PMMA/SAN interfaces; **a** SAN29; **b** SAN34; **c** SAN40. The top row features RGB composite images, with nitrogen and oxygen maps displayed in red and green, respectively. The maps were combined to highlight the formation of yellow interphase resulting from the overlap of red and green pixels. Arrows in the corresponding top images indicate the interfacial regions. The middle row exhibits intensity profiles acquired from the areas shown in oxygen and nitrogen maps and their ratios (O/N). The bottom row shows the changes in the intensities of nitrogen and oxygen core-loss peaks. The data was obtained using Image-EELS from the spots shown in the corresponding images. Reprinted with permission from [17]. Copyright 2007 John Wiley & Sons. All Rights Reserved

2 Thermodynamic Acceleration of Interdiffusion in Miscible Polymer Pairs

As presented in the previous section, the interfaces formed by the interdiffusion of PMMA and SAN can be visualized and the composition profiles across the interfaces were presented [17]. Here, the dynamics of interdiffusion in a miscible polymer pair (PMMA/SAN29) are discussed [18]. Figure 7 presents the developments of the interfacial layer between PMMA and SAN29 by thermal annealing with different periods and temperatures. The interfacial layer is visible as yellow due to overlapping green (oxygen) and red (nitrogen) pixels in the RGB composite images. The figure displays the development of the interfacial layer with welding time at temperatures above the glass transition temperatures (T_{gs}) of both polymers. The composition profiles across the interfaces for the relatively short welding times (Fig. 7a, b, and e) exhibit smooth single gradients that can be well-described by a hyperbolic tangent function [19]. As the welding time increases, the interfacial zones are widened with the profiles exhibiting two-step gradients with a plateau part in the middle. During the interdiffusion process, an equivalent composition of PMMA/SAN is formed at the central part of the layer. This layer appears after 12 h at 130 °C (Fig. 7c), while at 140 °C, it appears after only 4 h (Fig. 7f). The higher temperature accelerates the diffusion and promotes the plateau layer's formation. At temperatures significantly above the T_{gs} , the composition profiles with the plateaus at the midpoint are obtained in the earlier stage of the diffusion (Fig. 7 h and i, respectively).

Image-EELS enables to estimate the composition variation across the interface by the intensity ratios of the two core-loss peaks at the points of interest on the image [17]. In Fig. 8, the intensity changes of the nitrogen and oxygen core-loss peaks across the interface of the sample welded for 12 h at 130 °C are displayed, with the analyzed spots marked in the image. The integrated areas under the oxygen core-loss peak are compared to those of nitrogen using an energy window of 60 eV, giving the S_O/S_N ratios. It is evident from the data that the integrated intensity ratios of the core-loss peaks remain fairly constant in the central region with a plateau in the profile.

The following Eq. (4) describes the atomic ratios of two elements by the calculation of the ratio of the integrated intensities of the core-loss peaks (S_i) in an EELS spectrum:

$$\frac{N_1}{N_2} = \frac{S_1(\Delta, \alpha) \sigma_2(\Delta, \alpha)}{S_2(\Delta, \alpha) \sigma_1(\Delta, \alpha)} \quad (4)$$

where σ_i is the inelastic partial cross section, Δ is the energy window, and α is the collection angle. The core-loss peak ratios for oxygen and nitrogen (S_O/S_N) are determined experimentally via EELS using PMMA/SAN homogeneous blend films with known compositions. Subsequently, a master curve was constructed to represent the PMMA/SAN composition dependence of the integrated intensity ratio of the core-loss peaks, as depicted in Fig. 9. To ensure a specimen thickness of 50 nm, a

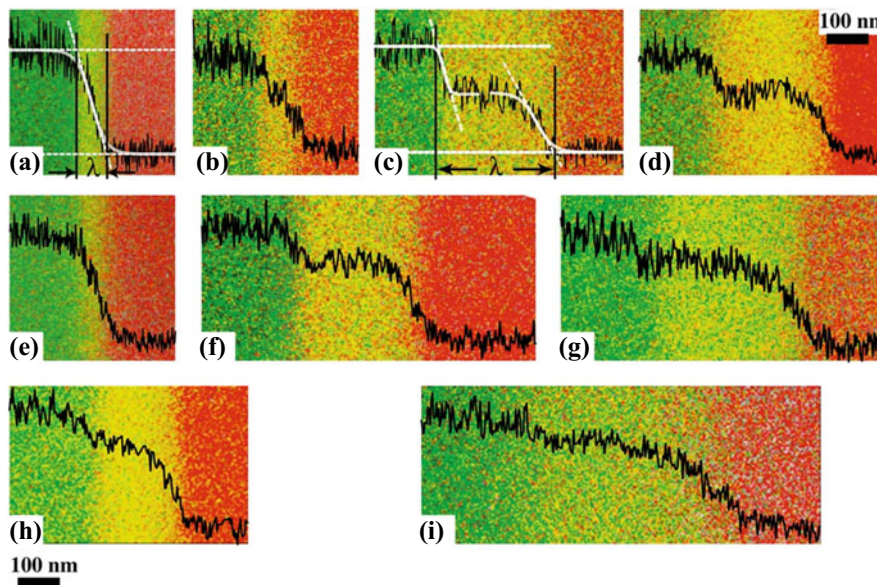


Fig. 7 RGB composite images of PMMA/SAN29 laminates, with green representing oxygen maps and red representing nitrogen maps. The laminates were annealed at various temperatures and times: **a**) 130 °C for 1 h; **b**) 130 °C for 4 h; **c**) 130 °C for 12 h; **d**) 130 °C for 24 h; **e**) 140 °C for 1 h; **f**) 140 °C for 4 h; **g**) 140 °C for 8 h; **h**) 150 °C for 2 h; **i**) 160 °C for 2 h. The oxygen-to-nitrogen concentration profiles are overlaid on the corresponding image. **a** and **c** demonstrate the process of determining the interface width (λ) by fitting the profiles with a hyperbolic tangent function. Reprinted with permission from [18]. Copyright 2007 American Chemical Society. All Rights Reserved

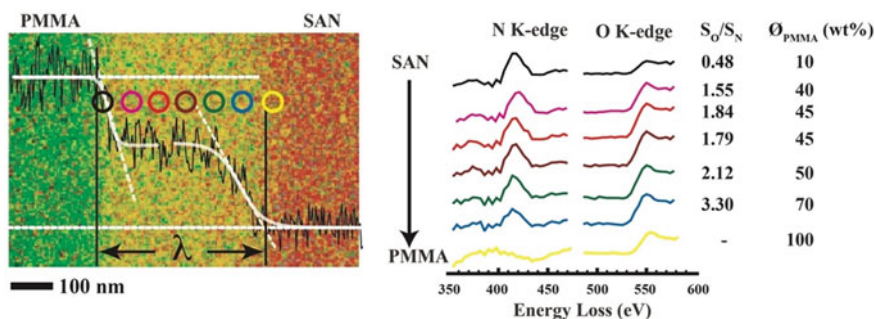
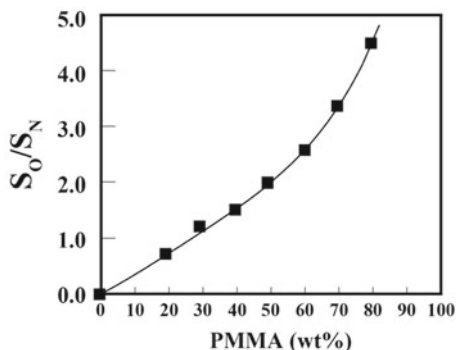


Fig. 8 The variations in N and O K-edges across the interface of a PMMA/SAN29 laminate annealed at 130 °C for 12 h (*middle*) and the ratios of integrated intensities (S_O/S_N) and estimated PMMA compositions (O_{PMMA}) (*right*). The analyzed positions are highlighted in the image (*left*), with the same colors as the corresponding spectra. Reprinted with permission from [18]. Copyright 2007 American Chemical Society. All Rights Reserved

Fig. 9 Ratio of the integrated intensities of N and O core-loss peaks (S_O/S_N) in EELS versus the PMMA composition in blend films of PMMA/SAN acquired by parallel EELS. Reprinted with permission from [18]. Copyright 2007 American Chemical Society. All Rights Reserved



THF solution was utilized for spin-coating onto a cleaved NaCl single crystal. Based on the findings, we were able to estimate the approximate compositions (ϕ_{PMMA}) in the interfacial region, which revealed that the central part of the interface with a low composition gradient contained PMMA at 40–50 wt%, as shown in Fig. 8. Similar levels of composition were also estimated for the other samples along the low gradient profile.

At temperatures above the T_g s of both PMMA/SAN polymers, their interdiffusion reveals unique composition profiles that differ from the classical profile by Fick's law, which is characterized by a constant diffusion coefficient and a maximum composition gradient at the profile midpoint. The occurrence of the unique composition profile obtained in this study is known to be the thermodynamic "acceleration". This acceleration arises from attractive interactions between the different segments, greatly enhancing the interdiffusion process relative to self-diffusion. The attractive interactions are proportional to the Flory–Huggins interaction parameter, χ , and the volume fraction of one polymer, ν , multiplied by $(1-\nu)$. The composition-dependent diffusion coefficient, $D_m(\nu)$, exhibits a maximum value at $\nu = 0.5$. The expression for $D_m(\nu)$ is obtained through an analysis of Flory–Huggins theory for the free energy of mixing of a polymer blend [3]:

$$D_m(\nu) = D_0[1 - 2\chi N\nu(1 - \nu)], \quad (5)$$

where D_0 represents the self-diffusion coefficient when the materials have the same mobility. When the absolute value of χ is roughly one order greater than $1/N$, where N stands for the polymerization index for PMMA or SAN, the second term in (5), i.e., the enthalpy term, becomes dominant, except for extremely low concentrations. This induces a thermodynamic "acceleration" diffusion behavior and results in a mutual diffusion coefficient D_m that varies with concentration, exhibiting a much higher diffusion constant in the middle of the concentration range [20].

Poly(vinyl chloride)/poly(ϵ -caprolactone) (PVC/PCL) is an example of this occurs where a notable negative χ parameter (-0.38) leads to a mutual diffusion coefficient (D_m) that is highly dependent on composition and diffusion constants that are much higher in the central concentration range [21]. Consequently, interdiffusion is hastened in the middle of the interfacial zone, resulting in a zone with an equivalent composition. The interaction parameter between PMMA and SAN can be calculated using Eq. (1) with the segmental interaction parameters obtained from the literature, which are -0.021, -0.028, -0.028, and -0.012 at temperatures of 130, 140, 150, and 160 °C, respectively. Though the χ parameters are not large negative values as those of PVC/PCL, they are still considerably higher than $1/N$, which is the primary reason for the thermodynamic “acceleration” phenomenon.

Polymer interdiffusion can be classified into normal Fickian diffusion (Case-I) and Case-II diffusion [22], based on diffusion and segmental relaxation rates. Case-I occurs when the diffusion rate is much lower than segmental relaxation, as in liquid–liquid interdiffusion. This type of diffusion can be described by the reptation model proposed by Edwards [1] and de Gennes [2], where polymer chains move within a virtual tube made up of the entanglement network of surrounding chains, constrained by this tube. These chains move in a Rouse-type motion [23] along their contour within the tube, and normal Fickian diffusion is observed after a time longer than the reptation time, according to equation [3],

$$\lambda = 2(D_m t)^{1/2}. \quad (6)$$

In contrast to normal Fickian diffusion, Case-II diffusion occurs when the diffusion rate is faster than the segmental relaxation rate. In the case of liquid/glassy polymer pairs, the diffusion is influenced by the polymer’s time-dependent mechanical response to the osmotic swelling stress at the penetrant diffusion front. This forms the core aspect of Case-II diffusion, where the interfacial width scales with time ($\lambda \sim t$).

To determine the interfacial width in our study, we calculated the tangent at the inflection point of the fitted curves to form a wedge shape and defined the interfacial width (λ) as shown in Fig. 7a. In situations where the composition profile has a middle plateau part, the profile was divided into two single hyperbolic tangent shapes and individually fitted by the function shown in Fig. 7c. Figure 10a illustrates that λ grows linearly with the square root of the welding time ($t^{1/2}$). Despite the local diffusion being driven by a thermodynamic “acceleration” mechanism resulting in an “anti-Fickian” profile, the overall interdiffusion in our study appears to obey Fickian diffusion, rather than Case-II diffusion with a scaling of $\lambda \sim t$ [3]. Using Eq. (7), we can calculate the apparent D_m as 4.26×10^{-15} , 1.66×10^{-14} , 3.76×10^{-14} , 1.82×10^{-13} cm²/s at 130, 140, 150, and 160 °C, respectively. The data in Fig. 10b is fitted with an Arrhenius expression, and the resulting solid line represents the best fit. The activation energy, E_a , was calculated to be 175 ± 15 kJ/mol.

$$D_m = D_0 \exp(E_a/RT) \quad (7)$$

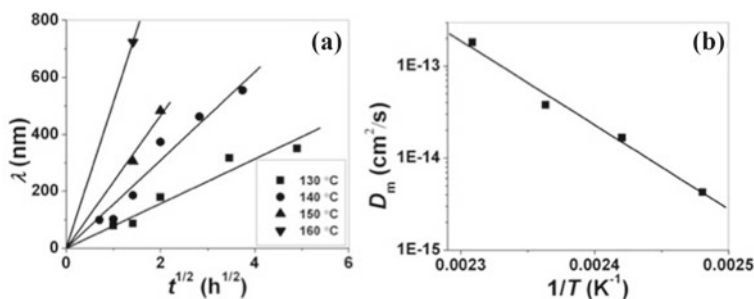
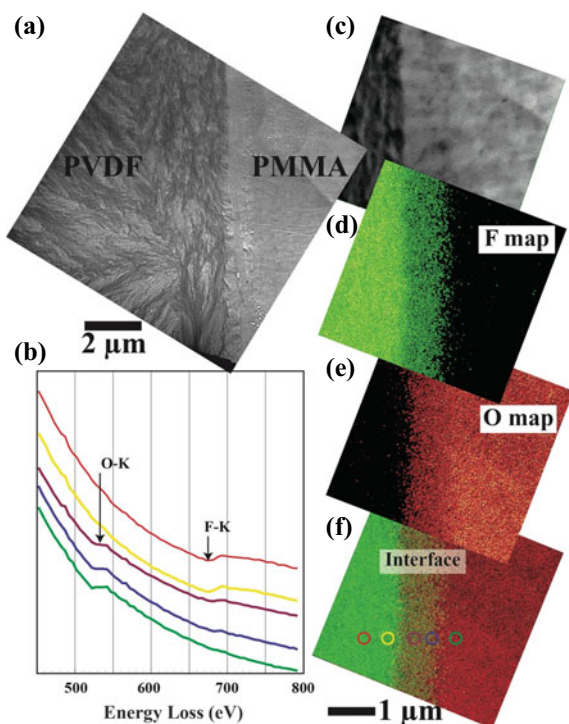


Fig. 10 Interfacial width (λ) versus square root of diffusion time for PMMA/SAN interfaces annealed at various annealing temperatures (a) and semilogarithmic plot of mutual diffusion coefficient (D_m) as a function of $1/T$ (b), where the solid line represents the best fit of an Arrhenius equation. Reprinted with permission from [18]. Copyright 2007 American Chemical Society. All Rights Reserved

To compare our findings to previously reported data, we utilized the approach proposed by Qiu and Bousmina [24], converting all four values of D_m to the reference temperature of 120 °C. These converted values ranged from 0.62 to 2.43×10^{-16} cm²/s, which were roughly one order of magnitude higher than the results obtained by Kim et al. (1.1×10^{-17} cm²/s) [25] using FRES and are in agreement with the values obtained by Yukioka et al. (1.0×10^{-16} cm²/s) [26, 27] using ellipsometry and by Qiu et al. (3.7×10^{-16} cm²/s) using rheometry [24]. These results suggest that EFTEM is a highly effective method for studying polymer interdiffusion.

The next section states that interfacial diffusion between identical polymers is extremely slow compared to dissimilar miscible polymer pairs. For example, when PS is bonded together, the thickness is 8 nm after 45 min at 120 °C and 15 nm after 36 h [28, 29]. On the other hand, PMMA/SAN29 forms a diffusion layer with an extraordinarily thick layer with 100 nm or more in 1 h. PMMA/polyvinylidene fluoride (PVDF) [30] is a unique miscible combination. It is possible to characterize the interfacial diffusion behavior by analyzing oxygen and fluorine elemental distributions by Image EELS. As shown in Fig. 11a, since PVDF is a crystalline polymer, it exhibits a morphological feature derived from spherulites, making it easy to identify the boundary as the crystalline/amorphous interface. The diffusion of each polymer can be characterized by the combination of oxygen (O) and fluorine (F) distributions. Both O and F ionization edges appear in the 500–800 eV energy loss range as shown in Fig. 11b, which were extracted from the spots indicated in Fig. 11f. Superimposing the F map, representing the PVDF location, on the energy-loss image shown in Fig. 11c indicates that PVDF diffuses toward the PMMA side over the crystalline/amorphous boundary (Fig. 11d). No penetration of PMMA into the crystalline PVDF phase seems to be taken place, as shown in Fig. 11e. It was found that an extremely thick interfacial layer with a thickness of about 1 μ m was formed in a very short time (Fig. 11f). Diffusion between identical polymers is caused only by the contribution of combinatorial entropy change, which is relatively small for high molecular weight polymers. As no significant increase in entropy is expected for diffusion between

Fig. 11 Image-EELS analysis of thermally-treated PMMA/PVDF interface at 180 °C for 5 min: **a** TEM image of the cross section; **b** energy-filtered image at 70 ± 10 eV energy losses; **c** fluorine map, **d** oxygen map, **e** RGB composite image with overlaying fluorine map (green) and oxygen map (red) on the energy-filtered image



polymers, interdiffusion is slowed. On the other hand, mixing dissimilar miscible polymer pairs adds the effect of exothermic interaction (negative χ parameter), and this enthalpic effect promotes fast diffusion.

3 Role of Interfacial Entanglements on Interfacial Toughness Studied by Nanofractography

3.1 Interfacial Thickness and Toughness in PMMA/SAN Interfaces

The entanglement structure is a crucial feature of polymer materials. However, the detailed topological structure still needs to be fully understood, as it cannot be observed experimentally even with high-resolution electron microscopes. It is especially difficult to characterize the local entanglement structures formed through the interdiffusion of polymers. The correlation between the structure of polymer chains at the interface and its resistance to crack propagation is significant for practical applications and scientific investigations. The adhesion between polymers is

controlled by intermolecular chain entanglements across the interface, which can provide physical links. The work of adhesion can be calculated based on surface and interfacial energies between two polymers. Still, experimental adhesion values are much higher than the calculated work of adhesion, indicating the significant contribution of polymer chain entanglements to the toughness of the interface [28, 29, 31–35]. For example, the work of adhesion between polystyrene (PS) and poly(methyl methacrylate) (PMMA) was measured to be 78.6 mJ/m^2 [36], while the measured interfacial toughness was 12 J/m^2 which is more than two orders of magnitude [28]. This means that the contribution of polymer chain entanglements to the toughness of the interface is significantly essential.

This study investigates the correlation between adhesion property and interfacial structure between PMMA and SAN, considering interfacial thickness and diffusion. The interfacial toughness is evaluated by an asymmetric double-beam cantilever (ADBC) test. The failure behavior in the test is inspected by the observation of fracture surfaces by high-resolution SEM. The interfacial fracture toughness (G_c) is measured by using asymmetric double cantilever beam (ADCB) specimen geometry as illustrated in Fig. 12a [37, 38]. This method has proved to be a simple but effective way of testing the toughness of interfaces between two polymer sheets. The specimens were prepared by compression molding of PMMA and SAN between silicon wafers. The interfacial toughness was measured by propagating an interfacial crack from a pre-crack inserted in a thin film of PTFE. The minimum G_c value was found by varying the thickness of the PMMA beams, and the appropriate thickness ratio of the two beams was determined to calculate the interfacial toughness using Eq. (6), where a is crack length, Δ is the thickness of the razor blade, E_i is the elastic modulus, h_i is the beam thickness, and $C_i = 1 + 0.64(h_i/a)$. The subscripts 1 and 2 refer to the PMMA and the SAN beams, respectively.

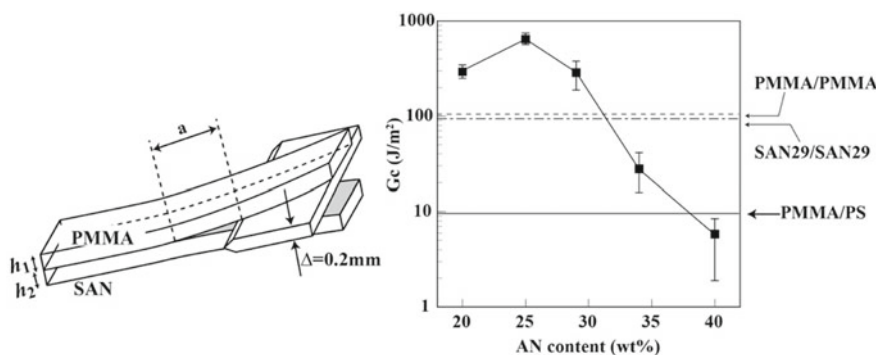


Fig. 12 Schematic drawing of the ADCB test specimen (left) and fracture toughness (G_c) of PMMA/SAN interfaces as a function of AN content in SAN annealed at $140 \text{ }^\circ\text{C}$ for 2 h (right). 8–10 measurements were taken for each polymer pair, and average values with maximum and minimum values are shown. Reprinted with permission from [17]. Copyright 2007 John Wiley & Sons. All Rights Reserved

To ensure contact between the two plates, the specimens underwent annealing at 140 °C for 2 h in the air under slight pressure. The interdiffusion was terminated by rapidly cooling the specimens to room temperature. A razor blade was pushed into the pre-crack to propagate an interfacial crack. Upon cessation of the crack propagation, the length ahead of the blade was measured with a microscope to determine the critical energy release rate, G_c . To determine the appropriate thickness ratio of the two beams so that the crack propagates along the interfacial plane, G_c values are calculated by varying the thickness of the PMMA beams between 1.7 to 2.3 mm, while the thickness of the SAN beams is fixed at 1.7 mm. Among these measurements, the minimum value is defined as interfacial toughness.

$$G_c = \frac{3\Delta^2 E_1 h_1^3 E_2 h_2^3}{8a^4} \frac{E_1 h_1^3 C_2^2 + E_2 h_2^3 C_1^2}{(E_1 h_1^3 C_2^3 + E_2 h_2^3 C_1^3)^2} \quad (8)$$

$$C_i = 1 + 0.64(h_i/a) \quad (9)$$

The ADBC test was performed to investigate how interfacial toughness is affected by the composition of random copolymer SAN. Figure 12 shows the specimen geometry in the left panel and the plot of G_c values against the AN content in SAN in the right panel. A significant increase in interfacial toughness is achieved as the AN content in SAN decreased, indicating that the interfacial toughness between PMMA and SAN is highly sensitive to the composition of SAN. The G_c values for PMMA/SAN29 were notably higher than those for identical polymers, i.e., PMMA/PMMA and SAN29/SAN29. In contrast, PMMA/PS showed a poor adhesion level similar to PMMA/SAN40, suggesting that the maximum adhesion strength could be achieved with AN content of 29 wt% or less. The high interfacial toughness of PMMA/SAN29 indicates that the interdiffusion is more rapid in the miscible pair than in the identical polymer pairs. This finding is attributed to the polymer pair with a negative χ parameter providing an additional favorable enthalpic driving force for a highly tough interface as mentioned in Sect. 2.

The EFTEM analyses of the PMMA/SAN interfaces indicate that increasing the interfacial width by around 100 nm significantly improves interfacial toughness. To investigate the cause of this improvement, we examined the fractured surfaces using SEM. SEM micrographs of the fractured surfaces of AN29, SAN34, and SAN40 are presented in Fig. 13a, b, and c, respectively. These micrographs were obtained near the crack tips after coating with OsO₄ plasma polymerized film to prevent charging, which is advantageous for high-resolution imaging by SEM due to its ability to provide sufficient conductivity with thinner films than the conventional gold-sputtered film [39]. The samples display various surface features, and the opposite PMMA surfaces show similar features as the counterpart SAN surfaces. The fracture surface of SAN29 contains numerous cell-like units of approximately 5 μm, identical to those found in bulk material fractures.

In contrast, SAN34 and SAN40 exhibit a macroscopically uniform and smooth surface. At the same time, higher magnification images reveal the presence of many

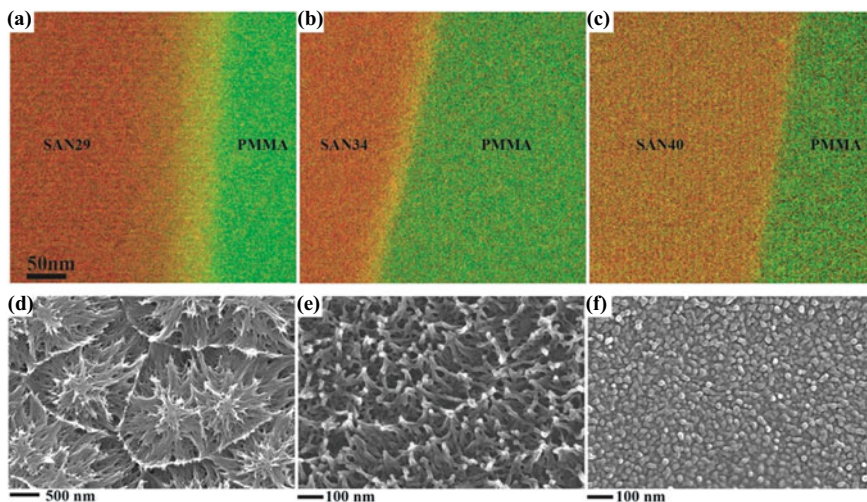


Fig. 13 Visualization of PMMA/SAN interfaces by EFTEM (*upper row*) and SEM micrographs showing fracture surfaces (*bottom row*): **a, d** SAN29; **b, e** SAN34; **c, f** SAN40; nitrogen and oxygen maps represented as red and green, respectively, and the yellow layers correspond to the interfacial layers

small fibrils with diameters of approximately 20 nm over the entire surface. These fibrils are elongated normally to the smooth surface, as shown in Fig. 13e and f. The length of the fibrils of SAN34 is greater than that of SAN40, suggesting that higher toughness could yield more extended elongation. These fine features on the fracture surface with relatively low toughness are observed for the first time using the high-resolution SEM (HR-SEM, Carl Zeiss, Ultra 55) technique with the in-lens SE detector and OsO₄ coating described in Sect. 2.6.1. According to the fractographic characteristics of SAN29, crack nucleation appears at the cell centers, followed by propagation from the inside outwards. The crack propagation process could involve several “crack nucleation and growth” cycles, which lead to cell-like patterns on the fractured surface. Ahead of the primary crack, microvoids may merge to form a continuous crack. The resulting dimple pattern is assumed to be produced from the combination of the primary crack front that develops due to the interface separation process, and the secondary crack generated by the microvoids’ nucleation ahead of the primary crack, as suggested by reference [40].

To understand this drastic change, the fracture surfaces of PMMA/SAN29 and PC/SAN29 are compared. The former is a miscible system, while the latter is an immiscible system. The G_c values of PMMA/SAN29 and PC/SAN29 are 290 and 10 J/m², respectively. The fracture behavior of immiscible PC/SAN29 differs from that of miscible PMMA/SAN29. The difference in the miscibility of those two systems exhibits significantly different failure appearances. The PC/SAN29 has a weak interfacial toughness due to its immiscibility. The fracture surface is so smooth that no topographic features can be seen in the micrometer scale (Fig. 14a). However, a

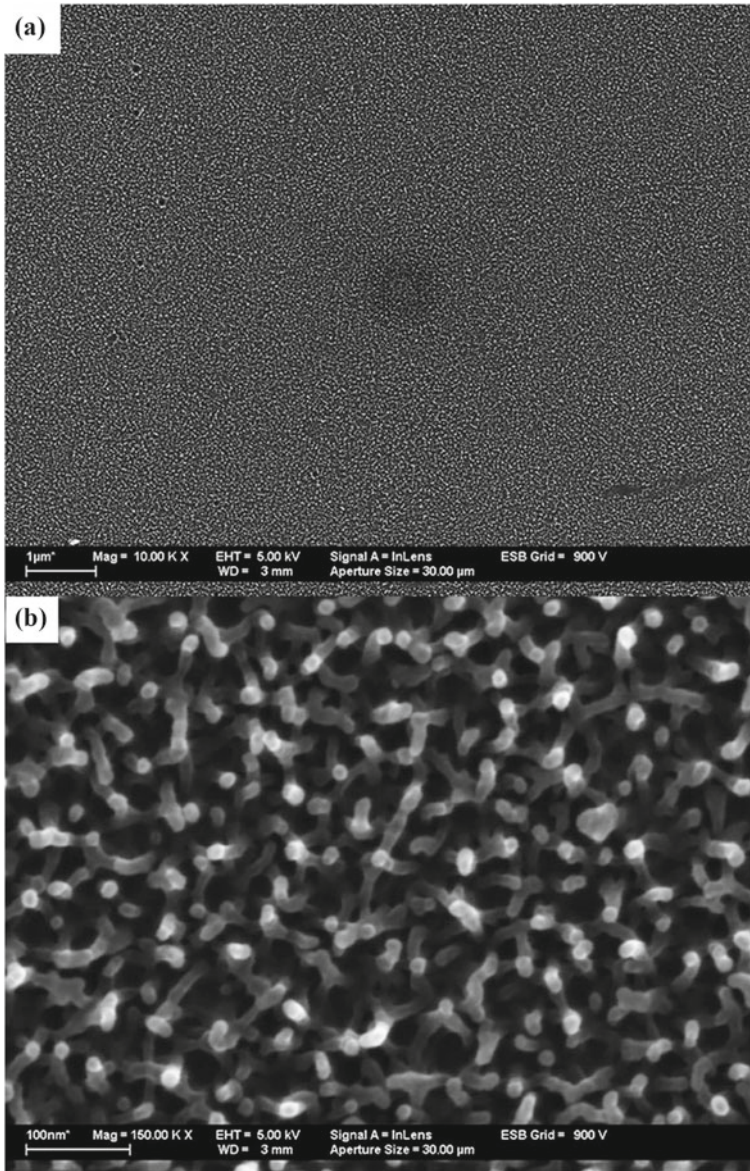


Fig. 14 SEM micrographs showing the fracture surface of SAN29 produced in the failure of PC/SAN29 interface. **b** is a magnified image of the central part of **(a)**

high-magnification view allows us to find the formation of nano-fibrils with approximately 20 nm diameter (Fig. 14b). XPS measurements of the fracture surfaces of PMMA/SAN29 showed comparable intensities of N1s and O1s peaks on both fracture surfaces, while the SAN29 surface was extremely rich in nitrogen, and the PC side was vice versa in PC/SAN29. This indicates that cohesive failure, where the crack progressed within the thick interfacial layer, occurred in PMMA/SAN29, while interfacial failure is the primary failure mode in PC/SAN29. Therefore, it can be mentioned that the transition from the micrometer-scale “dimple pattern” to the “nano-fibrous pattern” in fracture surfaces represents the changes in the miscibility of polymers.

3.2 *Interfacial Entanglements at PS/PS Welded Interfaces*

When interfaces fracture via interfacial failure, a “nanofibrillar” structure forms on the surface. A simple system is used for a basic study to understand the mechanism for the formation of this structure and its relationship with the interfacial entanglement structure. The system varying m involves welding two sheets of the same homopolymer with a narrow molecular weight distribution for periods at a temperature above T_g . This symmetrical system can clarify the criteria for producing the “nanofibrillar” surface structure when the interface fails.

Our study aims to examine the relationship between fracture surface patterns, interfacial width, and toughness by conducting welding experiments between identical molecular weights between the PS sheets [41]. The polymer chains diffuse across the interface during the experiment, increasing interfacial thickness over the welding time. Figure 15 depicts a double logarithmic plot of the interfacial toughness between the PS sheets, which have an M_w of 541 k and M_w/M_n of 1.07, versus welding time at 120 °C. Additionally, the figure includes HR-SEM images of the fracture surfaces obtained at various welding times. Schnell et al. conducted a study to explore the correlation between interfacial toughness and PS/PS interface thickness utilizing neutron reflectivity and fracture toughness measurement techniques [28]. The interfacial thicknesses they measured between protonated PS (752 k) and deuterated PS (660 k) are plotted on the same figure [42].

Schnell et al. proposed a three-stage model to explain the dependence of G_c on welding time [29]. In the first stage, G_c increases slowly and steadily. During the second stage, G_c increases rapidly within a short time, reaching a value close to that of bulk PS’s toughness. In the third stage, G_c remains constant and independent of welding time. Our findings show a similar trend, but the fracture toughness values during the initial stage are lower than those reported in the literature where the adhesion energy of 93 J/m² was measured after only 6 min. This may be due to the induction period for softening and wetting the thick (2 mm) specimens used in the ADCB test, which mainly occurs before chain interdiffusion is allowed, resulting in relatively lower interfacial toughness values. However, the measured G_c values are comparable to those attained with various immiscible polymer pairs with interfacial

thicknesses less than 10 nm [29, 32]. For example, the G_c between PS and PMMA is about 12 J/m^2 with an interfacial thickness of 5 nm. The toughness enhancement during the second stage occurs over a narrow range of interfacial thicknesses between 9 and 12 nm. Further polymer interdiffusion contributes little to the enhancement, consistent with Schnell et al.'s findings [29]. The HR-SEM images depict the dynamic change of fracture surface patterns with welding time and the relationship between interfacial toughness and the fracture surface. Figure 16a shows the production of the “nanofibrillar” pattern during the early stage when the interdiffusion and toughness are relatively low (90 min). In the second stage, the fibrils become elongated as G_c increases, as seen in Fig. 16b (5 h), followed by the appearance of micrometer-scale dimples in the later part of the second stage (6 h). Finally, during the third stage, the “nanofibrillar” surface disappears, and the micrometer-scale dimple pattern dominates, as observed in the PMMA/SAN29 miscible pair (Fig. 13).

According to previous research, a significant increase in interfacial toughness is associated with a change in the molecular failure mechanism [29]. Specifically, the fracture mechanism transitions from “chain pullout” to crazing at the critical interfacial thickness. Therefore, the “nanofibrillar” pattern is formed when “chain pullout” is the primary failure mechanism. In the second stage, when the interfacial toughness increases rapidly with increasing interfacial thickness, the transition from

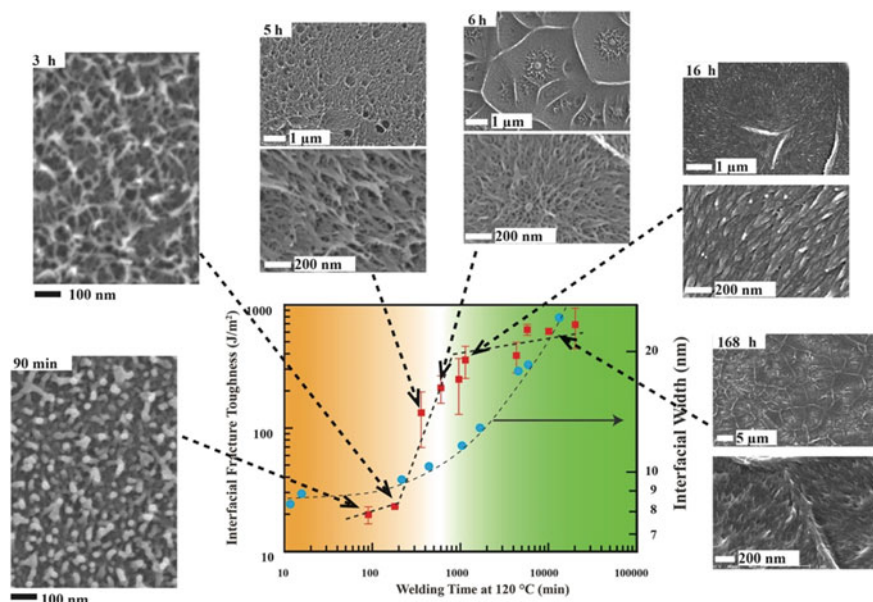


Fig. 15 The plot displaying the interfacial toughness (G_c) of PS/PS 541 k as a function of welding time at 120°C . The corresponding SEM micrographs of the fracture surface at different welding times are also presented. The plot additionally includes interfacial thickness measurements by Stamm et al. [42] using neutron reflectivity. Reprinted with permission from [41] Copyright 2008 American Chemical Society. All Rights Reserved

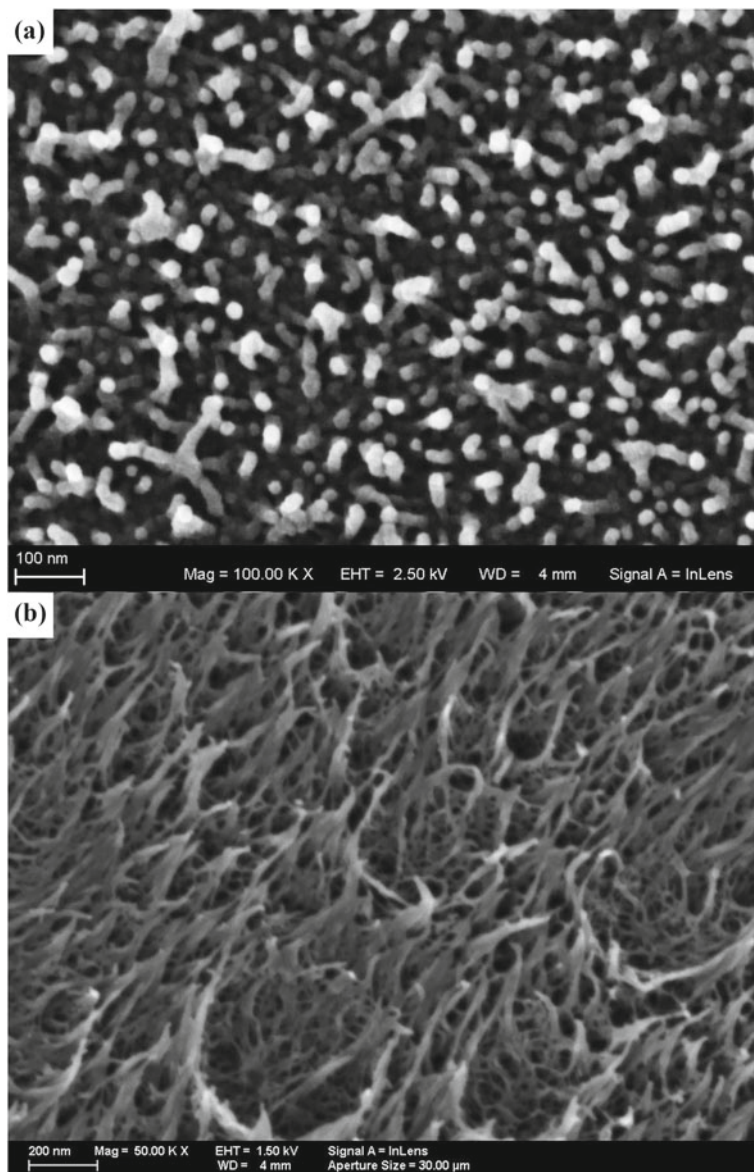


Fig. 16 SEM micrographs showing the fracture surface of PS-PS interfaces annealed at 120 °C for 90 min (a) and 5 h (b)

“chain pullout” to crazing occurs, and the fracture surface exhibits a combination of “nanofibrillar” and “dimple” features. As demonstrated in Fig. 17, the interfacial toughness of the polymer interface increases following an *S*-shaped curve as the interface thickness increases. It has been reported that when the interface thickness exceeds 10–15 nm, polymer chains become sufficiently entangled at the interface to form a plastic deformation zone at the crack tip, leading to toughness comparable to that of the bulk. In this plastic deformation region, crazing occurs, producing interpenetrating microvoids, cross-ties fibrils, and dissipating a significant amount of energy before the interface fails. It is believed that the nanofibrillar structure is formed when a thin interface separates with the disentanglement of polymer chains before crazing initiation.

The range of the critical interfacial thickness, which leads to a significant increase in interfacial toughness, is between 9 and 12 nm. This thickness is closely related to the average distance between the entanglement points in PS, estimated at 9.3 nm [43]. Thus, it is possible to achieve sufficient interfacial toughness with narrow interfaces that are considerably smaller than the radius of gyration of the polymer molecules, which is around 21.3 nm for 570 k PS [28]. These findings suggest that the polymer

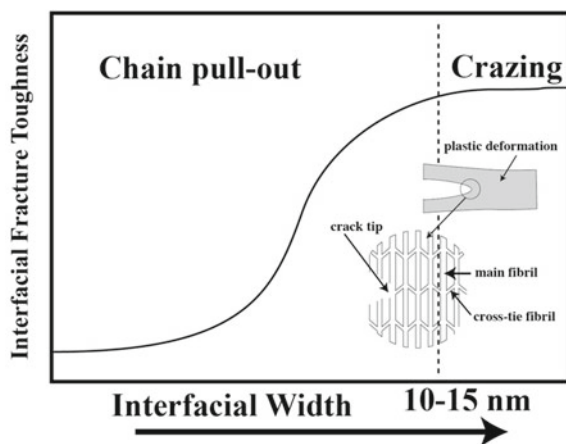


Fig. 17 Correlation between interfacial toughness and interfacial thickness

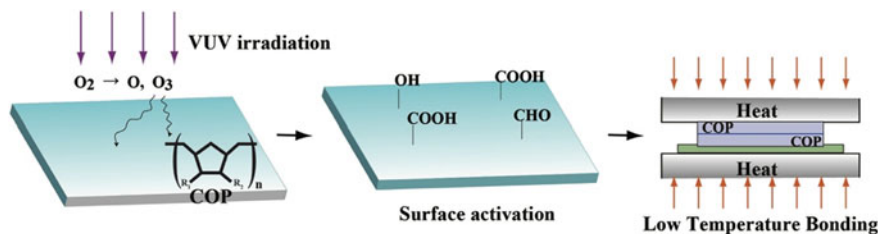


Fig. 3.18 Process of the low-temperature bonding of COP plates

chains must penetrate only roughly one entanglement distance to achieve optimum interfacial toughness.

Silvestri et al. proposed the term “partial crazing” to describe a scenario where crazing begins but does not fully develop, resulting in the breaking of some load-bearing strands during plastic deformation without creating cross-tie fibrils to transfer lateral stress [31]. The early stage of toughness development involves plastic deformation, and even in this initial stage, fracture energies are significantly larger than the work of adhesion, indicating the need for plastic deformation to dissipate a large amount of fracture energy. It is believed that the nanoscale fibrils result from plastic deformation created in the partial crazing regime before complete crazing occurs. In cases where polymer chains are not sufficiently entangled at the interface to initiate crazing, plastic deformation may occur at the crack tip, but the polymer chains may slip away, resulting in failure without forming lateral cross-tie fibrils. The diameter of craze fibrils is reported to be 5–30 nm, similar to the thickness of nanofibrils formed by chain pullout. The nanofibrils formed by the failure of thin interfaces are thought to be remnants of partial crazing. When crazing does occur, the fibrils elongate until they become thin enough that their traces are not visible.

To achieve an interfacial toughness (G_c) value similar to the bulk PS fracture energy (approximately 600 J/m²), annealing of the identical PS interface is required for over 10 h [28]. This indicates that in identical high molecular weight polymers, the driving force for diffusion is primarily the combinatorial entropy change, which is relatively low.

The “nanofibrillar” pattern found in narrow interfaces corresponds to the local entanglement structures that are similar to the entanglement spacing. This kind of surface feature has been observed in the failure of narrow dissimilar interfaces between immiscible polymers with block copolymers localized at the interface [44]. Classical fractography can only provide information on fracture mechanisms at micrometer scales, whereas HR-SEM enables the study of interfacial entanglement structures, which enables us to perform “Nanofractography.” This method has the potential to advance our understanding of adhesion and bonding mechanisms.

3.3 Mechanism of Low-Temperature Bonding of VUV-Activated COP

Surface structures similar to nanofibrils are observed in the failure of the interfaces in surface-activated cyclo-olefin polymer (COP). COP is a low-cost amorphous polymer with high transparency, heat resistance, and low water absorption [45]. However, due to its simple chemical structure lacking effective polar functional groups for adhesion, surface modification is necessary for achieving high adhesion strength. Sugimura et al. investigated the COP surface activation by vacuum ultraviolet (VUV) treatment, which generates oxygen-containing ether, ketone, and carboxyl units on the surface to produce a hydrophilic surface and enable adhesive-less direct bonding

at low temperatures below the T_g [46]. Low-temperature bonding is an effective method for preserving sub-micrometer-scale features created in the COP plates, but the detailed bonding mechanism remains unknown [47]. This bonding mechanism is presumed to involve attractive interactions between chemical functional groups on the surface, enabling bonding without sufficient interdiffusion.

The bonding mechanism of low-temperature surface-activated COP is investigated by the nanofractography technique [48]. Figure 19 presents the influence of the VUV irradiation on the interfacial toughness acquired by bonding at 110 °C. To assess the interfacial toughness, the DCB test was employed with the symmetric DCB specimen geometry, where 1 mm thick COP plates were bonded. In this situation, Eq. (8) is simplified as Eq. (10) to compute G_c .

$$G_c = \frac{3\Delta^2 E h^3}{16a^4 C^4} \quad (10)$$

When a razor blade is inserted into the interface in the bonded laminates, the crack propagates ahead of the blade, and no significant crack propagation is observed after an hour. The initial G_c values are calculated based on the crack length thus obtained. The results indicate that the maximum G_c can be achieved with a 5-min VUV irradiation, and prolonged exposure does not result in further enhancement but rather

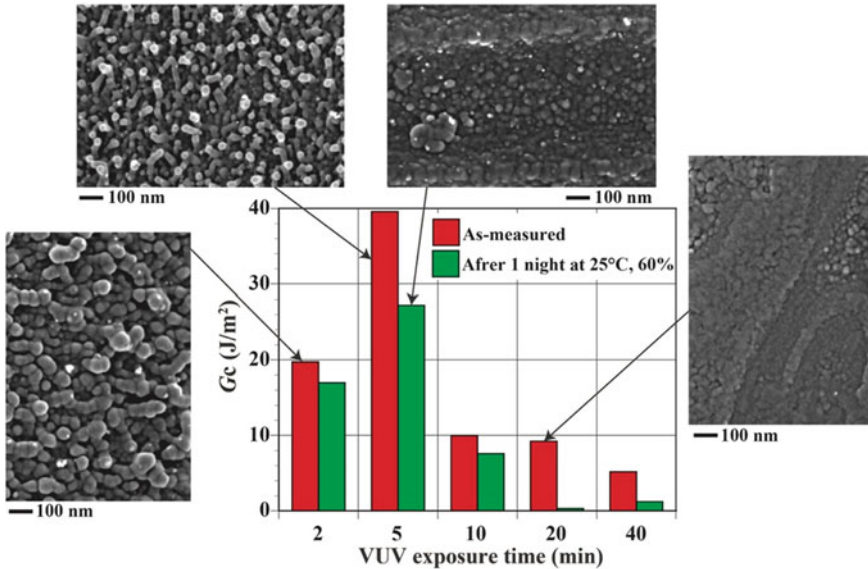


Fig. 19 Effect of VUV irradiation period and a high humidity environment on interfacial fracture toughness (G_c) of low-temperature bonding of COP. The average and standard deviations were calculated with at least ten data points for each laminate. SEM micrographs shown on upper side of the graph are fracture surfaces produced in the indicated conditions. Reprinted with permission from [48]. Copyright 2016, The Society of Polymer Science, Japan, All Rights Reserved

causes a decrease in G_c . To assess the effect of humidity on interfacial toughness, crack growth was measured after the specimens were left at 25 °C and 60%RH for 12 h. The G_c values decrease from their initial values for all VUV irradiation conditions in such a humid condition. The crack continues to propagate slowly as the specimen with the inserted razor blade was left under the humid condition, indicating that water vapor degraded the interfacial toughness. According to Sugimura and colleagues, the content of oxygen-containing functional groups on the COP surfaces increased with increasing VUV irradiation time of up to 40 min, and the water contact angle decreased [46]. These findings suggest that the optimal condition for bonding is not necessarily the same as that for the degree of surface activation.

In Fig. 19, SEM micrographs present the fracture surfaces of the DCB test specimens. The specimens VUV-irradiated for 2, 5, and 20 min, and the specimen exposed to the high humidity conditions after 5 min VUV-irradiation are shown. Before bonding, no surface features are observed on the surface of the VUV-irradiated specimens. The SEM micrographs indicate that many nano-fibrils are present on the fracture surfaces of the specimens irradiated for 2 and 5 min, which have relatively high G_c values. The results suggest that the surface-activated COPs exhibit similar surface features to those produced on the fracture surface of interfaces formed in melt conditions. The elongation, thickness, and density of the fibrils characterize their features. Conversely, the fracture surfaces of the specimens irradiated for 20 min, which have an extremely low G_c value, exhibit barely visible fibrils. Additionally, the fracture surface produced during exposure to high humidity conditions displays surface features significantly different from those produced in the as-irradiated specimen. Although surface features with similar length scales are produced, the height of the fibrils is relatively low.

The fact that the 2 and 5 min VUV-irradiated COPs produce the nano-fibrils on their fracture surfaces suggests that the interfaces failed via “chain pullout”. Since the bonding temperature (110 °C) is much lower than the T_g of COP (140 °C) and the bonding time is short (10 min), there is not enough mutual interdiffusion to form sufficient entanglement at the interface. It is presumed that hydrogen bonds at the interface between the oxygen-containing polar functional groups bridge the polymer chains across the interface. These polymer chains can reinforce the interface and be pulled out during the fracture.

Increased VUV irradiation results in more polar functional groups on the surface, which could produce more polymer chains across the interface. However, prolonged VUV irradiation also leads to polymer degradation beneath the activated surface, making fragments with lower molecular weight than the average molar weight between entanglement points. Despite an increase in the number of polymer chains across the interface, effective interfacial entanglement cannot be formed under such conditions, resulting in poor interfacial toughness. Exposure to high humidity allows water molecules to penetrate the interface and disrupt the hydrogen bonds formed at the interface, decreasing interfacial toughness.

Two analytical electron microscopy techniques were performed to inspect the interfaces of the COP bilayer specimens. Directly imaging the interfaces between identical polymers by conventional TEM is difficult since no contrast can be obtained

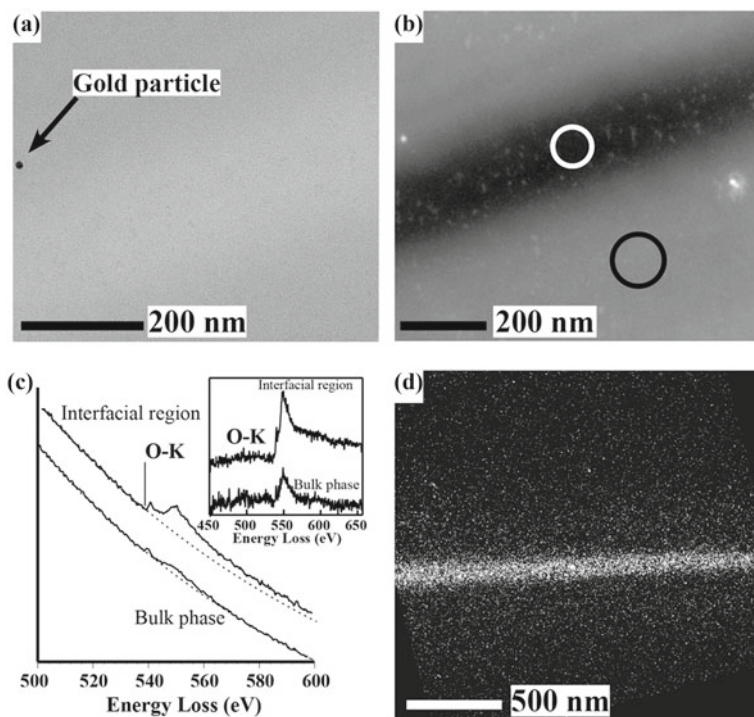


Fig. 20 EFTEM analysis of the interface between the 5 min VUV-irradiated COPs formed by the low-temperature bonding: **a** zero-loss image; **b** structure-sensitive image at 150 ± 5 eV energy loss; **c** O K-edges in EELS spectra acquired inside and outside the interfacial region shown in **b** with an inset of the background-subtracted O K-edges; **d** oxygen map created by three-window method. Reprinted with permission from [48]. Copyright 2016, The Society of Polymer Science, Japan, All Rights Reserved

between the COP plates. However, in our case, oxygen is introduced only in the region underneath the surface with a certain depth, allowing for the possibility of imaging the VUV-modified region by tracing the location of the oxygen element. In Fig. 20a and b, energy-filtered images by EFTEM of the specimen VUV-irradiated for 5 min are shown, one of which is a zero-loss image (ΔE is 0 ± 5) and another of which is a structure-sensitive image at 150 ± 5 eV. The interfacial region appears as a dark, approximately 200 nm thick layer in the energy-filtered image at 150 eV, while the zero-loss image does not clearly show the interfacial region. The EELS spectra acquired from the areas inside and outside the interfacial region are shown in Fig. 20b and c, respectively. The core-loss peaks of the O K-edges are shown in the inset of Fig. 20c, which are created by the subtraction of the BG component calculated by the power-law function shown as the dotted curves drawn along the as-measured spectra. The localization of oxygen in the interfacial region is due to the polar functional groups produced by the VUV irradiation. A small amount of oxygen is also detected over the entire area in the specimen, which may be derived

from the stabilizing agent contained in the gold colloid. An oxygen elemental map in Fig. 20d is calculated by the three-window method using three energy-loss images at 450 ± 5 , 500 ± 5 , and 550 ± 5 eV, which indicates the formation of a uniform interphase with a thickness of about 200 nm. This leads to an estimation of the depth of the surface activation of about 100 nm.

The interfacial region is also visualized using STEM-EDX, and the resulting images are presented in Fig. 21a and b as bright field (BF) and annular dark field (ADF) images, respectively. The BF and ADF images show the interfacial layer, which is similar to what was observed with EFTEM. The BF image can sufficiently identify the interfacial region, while the ADF image provides a much clearer contrast due to the difference in chemical composition between the interfacial region and the bulk part. The ADF image's contrast is related to the mass thickness and atomic numbers in the specimen. STEM allows the creation of an image by detecting signals at each probe position without an objective lens, resulting in a relatively minor effect of chromatic aberration on image quality. EDX microanalysis conducted on points within and outside the interfacial layer shows the presence of oxygen as shown in Fig. 21c, confirming the bright layer in the ADF image to be an oxygen-rich region. The ADF image of the sample prepared by VUV irradiation for 40 min is displayed in Fig. 21d, demonstrating that longer irradiation does not significantly increase the thickness of the activated layer. The VUV treatment remains confined to a depth of 100 nm below the surface, even with prolonged irradiation.

The proposed mechanism for the low-temperature bonding of VUV-irradiated COP is presented in Fig. 22. VUV irradiation generates polar functional groups such as $-\text{OH}$, CHO , COOH , etc., with a modification depth of about 100 nm, which is almost independent of the irradiation time. Shorter VUV irradiation times (less than 5 min) result in the formation of hydrogen bonds between functionalized polymer chains on both sides of the interface, reinforcing the interface and allowing energy dissipation during fracture via chain pullout of the coupled polymer chains. However, exposure to humidity can cause the hydrogen bonds to break, decreasing toughness. Longer VUV irradiation times generate more functional polar groups but can also cause polymer degradation, resulting in low molecular weight species. As a result, the polymer chains across the interface cannot achieve effective entanglements, leading to low interface toughness. The interfacial fracture toughness is greatly reduced by 10-min VUV irradiation, with the molecular weight decreasing below the critical value of the molecular weight between the entanglement points of COP.

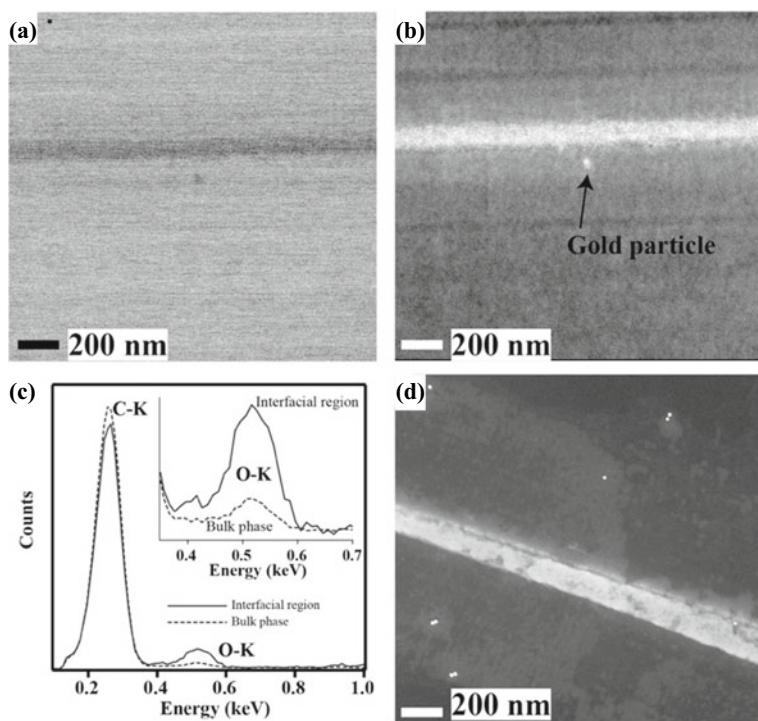


Fig. 21 STEM-EDX analysis of the interface between the COP laminate VUV-irradiated for 5 min: **a** STEM-BF image; **b** STEM-ADF image; **c** EDX spectra taken from the points inside (straight line) and outside (dotted line) the interfacial region; **d** STEM-ADF image showing the interfacial region between the COP plates surface-activated by 40 min VUV irradiation. Reprinted with permission from [48]. Copyright 2016, The Society of Polymer Science, Japan, All Rights Reserved

4 Adhesive Bonding by Surface and Interface Modifications of Polypropylene—Effect of Chemical Bonding and Mechanical Interlocking

Polypropylene (PP) is an important plastic material for the industry due to its high environmental durability, excellent heat resistance, and lightweight and inexpensive. The low surface energy of PP inhibits adhesion to most adhesive and coating formulations. The poor adhesion property of PP limits its use in various applications. Thus, different surface treatment techniques for adhesion improvement have been developed. However, the mechanisms of the surface pretreatment effect have yet to be fully understood. In this study, flame treatment and plasma treatment for the adhesion improvement of PP with an epoxy adhesive are evaluated and that mechanism is considered.

The interface between PP and adhesive involves multiscale structures with length scales ranging from Å to μm. The surface treatments of PP cause changes in the

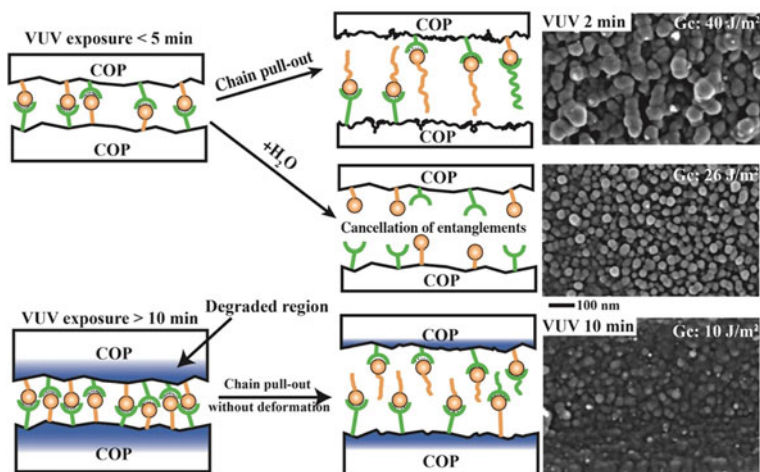


Fig. 22 Schematic illustrations describing the mechanism of low-temperature bonding of VUV-irradiated COP. Reprinted with permission from [48]. Copyright 2016, The Society of Polymer Science, Japan, All Rights Reserved

molecular structures and the crystallinity of the surface and create surface topography with the features of nanometer to micrometer scales. We are investigating such multi-scale interfacial structures formed between the adhesive and PP by electron microscopy [49, 50].

Commercial isotactic polypropylene (*i*PP) is press-molded at 200 °C into 3 mm thick plates between silicon wafers to obtain a flat surface to exclude the effect of initial surface roughness on adhesion behavior. The plasma treatment uses an atmospheric damage-free plasma source with N₂ gas, PF-DFMJ01, developed by Plasma Concept Tokyo Inc., Japan. The plasma source is scanned twice over the *i*PP plate with a 5 mm/s scanning speed and a 5 mm gap between the plasma source and the sample, as shown in Fig. 23a and the associated video. Flame treatment is employed by briefly exposing blue flame over the *i*PP surface by scanning the sample twice under the flame with 60 mm/s, as shown in Fig. 23b and the associated video. Those surface-treated and non-treated *i*PP plates are laminated with two-component epoxy adhesive, Denatite 2204 (Nagase ChemteX Corp.), and cured at 45 °C for 12 h.

Interfaces between *i*PP and the epoxy adhesive are investigated by STEM at an accelerating voltage of 200 kV. Thin cross sections of the interface are cut from the laminates by ultramicrotomy after staining with RuO₄. Surface morphologies before bonding are also investigated by the replica-STEM technique. As described in Sect. 2.3.3, a thin film of Pt with a thickness of 6.5 nm is deposited by sputtering at a low angle of 25°. To strengthen the Pt film, a carbon layer with a thickness of 25 nm is coated by sputtering at a high angle of 90°. The specimen is horizontally rotated during deposition to ensure that the deposit fills small spaces on the surfaces. After deposition, a 30 wt% aqueous gelatin solution is applied to the carbon surface and

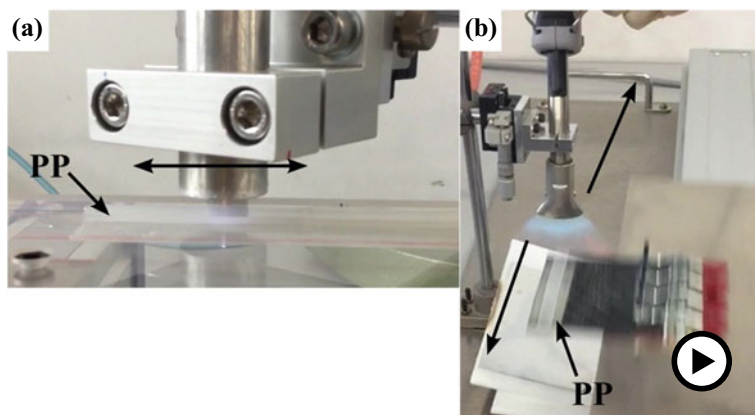


Fig. 23 Video showing atmospheric plasma (a) and flame (b) pretreatments of *i*PP surface employed for adhesion improvement (▶ <https://doi.org/10.1007/000-ayn>)

allowed to dry overnight under ambient conditions. The resulting solidified gelatin layer is removed along with the replica film from the substrate and immersed in an aqueous potassium thiocyanate (KSCN) solution to dissolve the gelatin layer. Following the complete dissolution of the gelatin layer, the Pt-carbon replica film is washed using dilute H_2SO_4 and water before being transferred onto copper grids coated with collodion. Finally, the replica film is observed by STEM.

Figure 24a–c shows STEM annular dark field (ADF) images of the replica films produced from the non-treated, flame, and plasma-treated *i*PP sheets, respectively. The replica from the non-treated sample (Fig. 24a) exhibits the lamellar feature of the *i*PP surface, indicating that the crystalline structures of the *i*PP surface are successfully transferred to the replica. The replica from the flame-treated sample (Fig. 24b), on the other hand, shows flat but no crystalline features, suggesting that an amorphous layer is formed after the flame treatment, and a replica of the plasma-treated sample (Fig. 24c) shows a very rough surface with pores of about 100 nm. Therefore, we can recognize that the two different surface treatments produce significantly different surface structures.

Figure 25 shows cross-sectional STEM-bright field (BF) micrographs of the interfacial regions between the adhesive and the surface-treated *i*PPs. As shown in Fig. 25a, the flame-treated *i*PP shows a relatively smooth interface where the strongly RuO_4 -stained layer with 50 nm thickness is formed. This result agrees well with the surface structure deduced by the replica experiment. The high-magnification view of Fig. 25a shows the lamellae of *i*PP in the bulk part underneath the interfacial amorphous layer. It can be interpreted that the rapid scanning of high-temperature flame over the *i*PP substrate melts the surface region of *i*PP and freeze the melted structure upon the rapid cooling from the melted state. The T_g of the amorphous part of *i*PP is lower than at room temperature; thus, this soft layer may form entanglements with the epoxy adhesive.

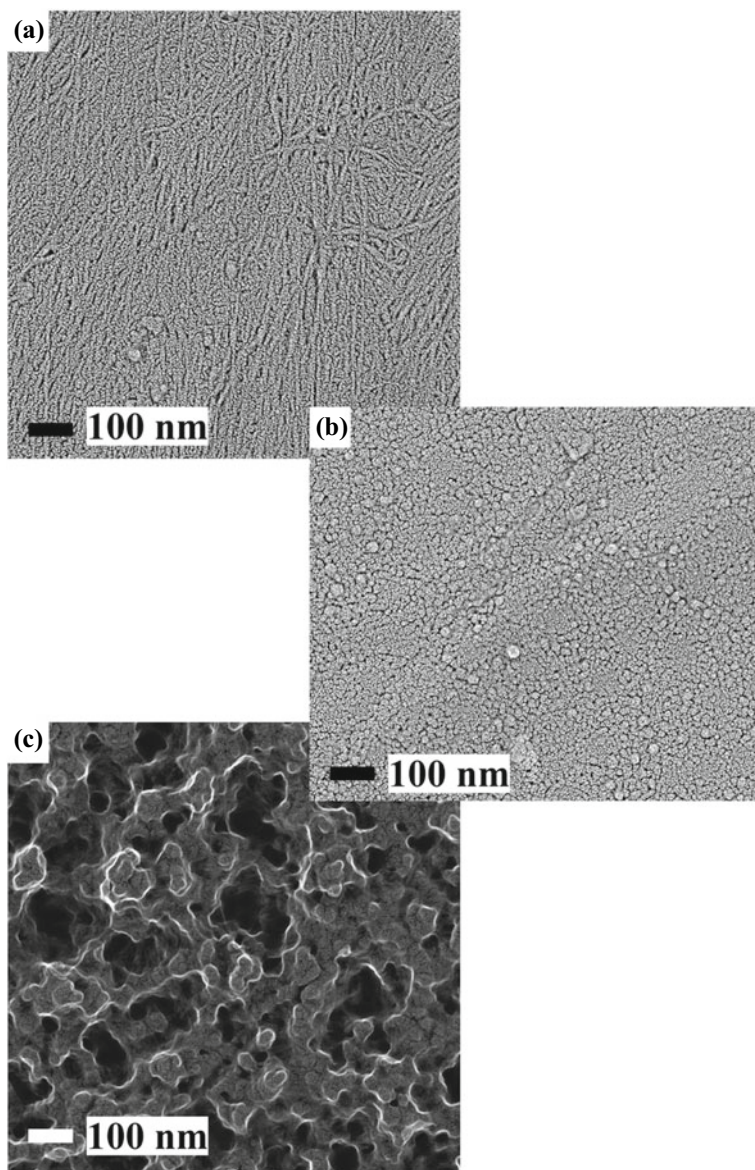
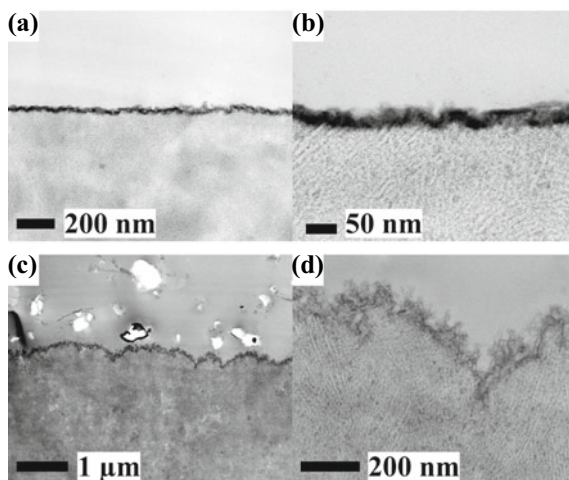


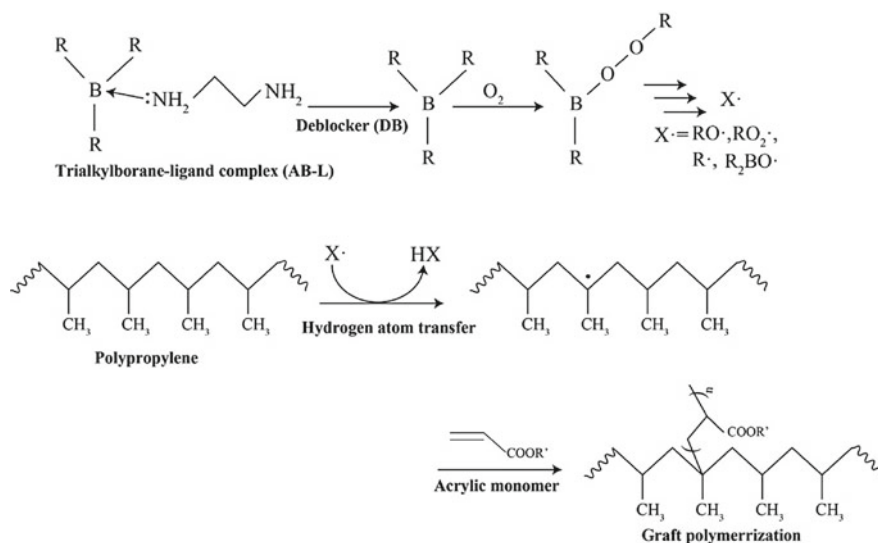
Fig. 24 STEM-ADF micrographs of replicas films showing the surface morphologies of *iPP*: **a** no treatment; **b** flame treatment; **c** plasma treatment

Fig. 25 STEM-BF micrographs showing the interfaces between *i*PP and adhesive: **a** flame treatment; **c** plasma treatment; **b**, **d** magnified images of **a** and **c**, respectively. The holes seen in the adhesive layer in **c** correspond to the traces of the inorganic fillers dropped off during the sectioning by ultramicrotomy



The plasma-treated *i*PP, on the other hand, exhibits an interface involving two different topological structures with different length scales, as shown in Fig. 25c and d. One is a rough feature having about 1 μm periodicity, while the other exhibits roughness with about 10 nm periodicity. The plasma treatment may etch the surface in two different processes simultaneously. The physical attack of plasma may create the micrometer scale etched surface. In contrast, the nanometer scale topological feature may be created chemically by the reactive species produced by the plasma. Figure 25d indicates that the roughness is almost equal to the lamellar thickness. It is therefore speculated that the amorphous part between the lamellae, called tie molecules, can be selectively etched chemically owing to the difference in the resistivity against the plasma between the amorphous and crystal parts. One can also recognize that the thin layer at the interface is relatively stained and more robust than the inside, suggesting that a thin layer with low crystallinity is formed at the surface. The crystalline structures of *i*PP are preserved under the modified skin layer. This means the plasma treatment can largely change the surface topographic features without losing the original polymer structures. And also, the adhesive can penetrate the complicated rough surface without voids.

We also evaluate the interfacial modification of *i*PP by an alkylborane-initiated acrylate-based adhesive. The chemical concept is shown in Scheme 1. In the first step, an alkylborane-ligand complex (AB-L) containing a monomer solution is mixed with another mixture of a deblocker (DB) and the monomer. Diisocyanate is used for the deblocker in this experiment. The complexed alkylboranes are deblocked in this process, generating uncomplexed trialkylborane, which is oxidized and produces several types of radicals. In the second step, the generated radicals initiate free-radical polymerization and graft polymerization from the *i*PP substrate. In the third step, an interfacial chemical reaction occurs between the adhesive and the substrate through hydrogen atom transfer, introducing radicals onto the *i*PP's backbone, where graft polymerization is initiated [51, 52].



Scheme 1 Reaction and adhesion process via complexed alkylborane

The adhesive mixture is placed between two *i*PP sheets at room temperature for 1 h, giving a strictly bonded plate. Figure 26 shows STEM-ADF images showing the interfacial region between *i*PP and the adhesive, where the bottom is the *i*PP substrate. The low magnification view (Fig. 26a) indicates that the adhesive creates a rough interface. The high magnification image (Fig. 26b) shows that the lamellae are partially cleaved from the substrate, producing disordered crystal structures. The stained region appears bright in the ADF images, corresponding to the amorphous part of *i*PP. Therefore, the highest magnification image (Fig. 26c) implies that the radical species produced by the oxidation of alkylborane attacks the amorphous phase between the lamellae and cleave the lamellae from the *i*PP substrate. In the next step, the acrylate monomers invade the amorphous part of *i*PP and initiate graft polymerization onto the lamellae. The STEM-ADF images present evidence of chemical interaction between the alkylborane (AB) initiated adhesive and *i*PP. Still, it is not a simple phenomenon, creating a heterogeneous thick interphase comprising the *i*PP lamellae, the amorphous *i*PP, and the grafted acrylate polymers.

The DCB test evaluates interfacial toughness. Untreated *i*PP does not bond at all and thus cannot be tested. Flame and plasma treatments, on the other hand, improve bond strength and allow testing, showing G_c values of 60 and 150 J/m², respectively. The AB-initiated adhesive offers excellent adhesion performance in the DCB test. The crack is not produced at the interface when the razor blade is inserted into the interface and the *i*PP plate fails.

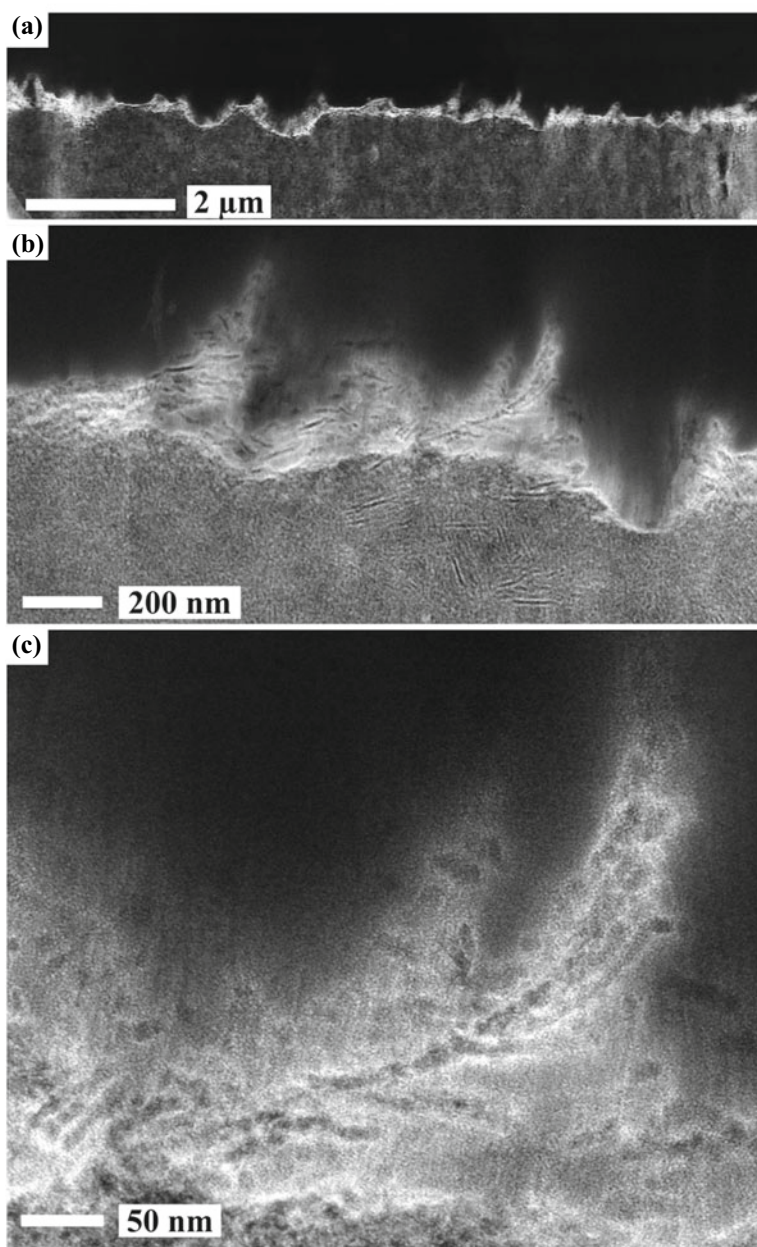


Fig. 26 STEM-ADF micrographs showing the interfacial region created by the alkylborane-initiated acrylate adhesive. The magnification increases in the order of **a**, **b**, and **c**

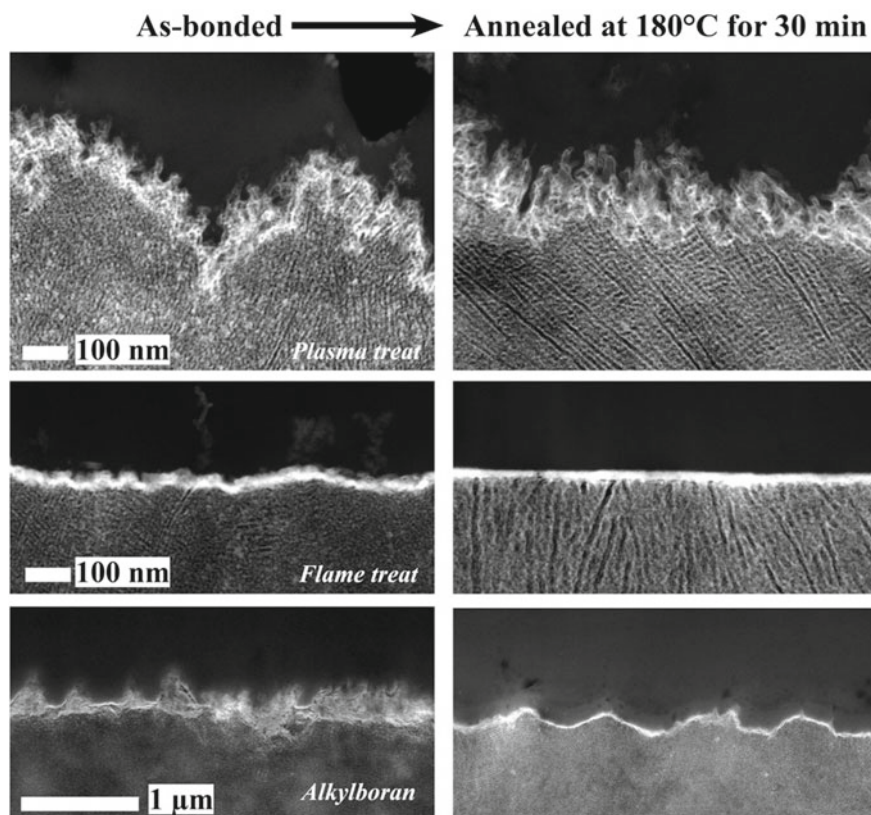


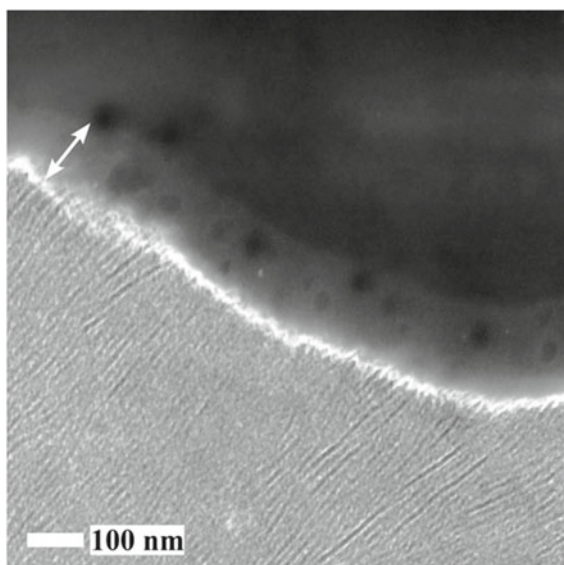
Fig. 27 STEM-ADF micrographs showing the changes of the interfacial region by thermal treatment at 180 °C for 30 min and subsequent cooling: plasma treatment (upper row); flame treatment (middle row); alkylborane-initiated adhesive (bottom row). The left column shows the interfaces of the as-bonded specimens, while the right column shows the interfaces after the thermal treatment at 180 °C for 30 min

We conduct further experiments to study the adhesion mechanism of the three surface and interface modification techniques. The bonded plates are annealed at 180 °C for 30 min and then cooled to room temperature. During this thermal treatment, the *i*PP melts and recrystallizes. The interfacial structures before and after the thermal treatment are inspected by STEM as shown in Fig. 27: The plasma-treated sample loses the micrometer level roughness features and flattened the interface with retaining nanometer-scale roughness after the thermal treatment (*upper row*). In the flame-treated sample, the thermal treatment makes the thin amorphous layer smooth (*middle row*). At the interface modified by the AB-initiated adhesive, the disordered lamellae produced by graft polymerization disappear while maintaining the micrometer-level roughness features (*bottom row*). The fact that the plasma-treated sample changes the morphology of the interface significantly suggests that the interface is loosely bonded. A similar trend is indicated in the flame-treated sample. Flame

treatment forms an amorphous layer and simultaneously causes chemical structure changes in *i*PP. The flat layer that forms after recrystallization comprises chemically modified compounds. The *i*PP that maintains the original structure included in the initial amorphous layer may be able to take part in recrystallization. Therefore, a thinner and flat interfacial layer is formed after the thermal treatment. In contrast to the plasma and flame pretreatments, the micrometer-scale roughness of the interface created by the AB-initiated adhesive remains the same even after the thermal treatment, indicating that the chemical bonding between *i*PP and the adhesive fixes the interface. The graft polymers developed onto the *i*PP main chains, produced by the AB-initiated adhesive, may disturb the recrystallization. Therefore, alternatively, a 100 nm thick layer is formed between the *i*PP crystalline phase and the adhesive, occluding domains of the adhesive composition as shown in Fig. 28, which is the high-magnification image of the bottom right image in Fig. 27. It should be mentioned that the lamellae can be seen clearly and tend to align perpendicular to the interface in all three samples after the thermal treatment. This means that the crystallization starts from the interface and grows inside.

The flame and atmospheric plasma treatments are effective for the adhesion of *i*PP, but the mechanism for those surface treatments differs. The flame treatment creates a thin amorphous layer on the surface which may promote the penetration of the epoxy adhesive and form molecular entanglement. This physical interaction is the main reason for the adhesion enhancement. The plasma treatment produces complicated surface roughness without the loss of the crystalline structure of *i*PP. This surface roughness mainly contributes to the adhesion increment to facilitate mechanical interlocking. Therefore, the chemical reactions between the adhesive and the substrate are not the first reason for the adhesion improvements. On the other

Fig. 28 STEM ADF micrograph showing the interfacial layer and the lamellar orientation formed after the thermal treatment in the interfacial region between the AB-initiated adhesive and *i*PP. The arrow indicated the amorphous layer formed by the graft polymer



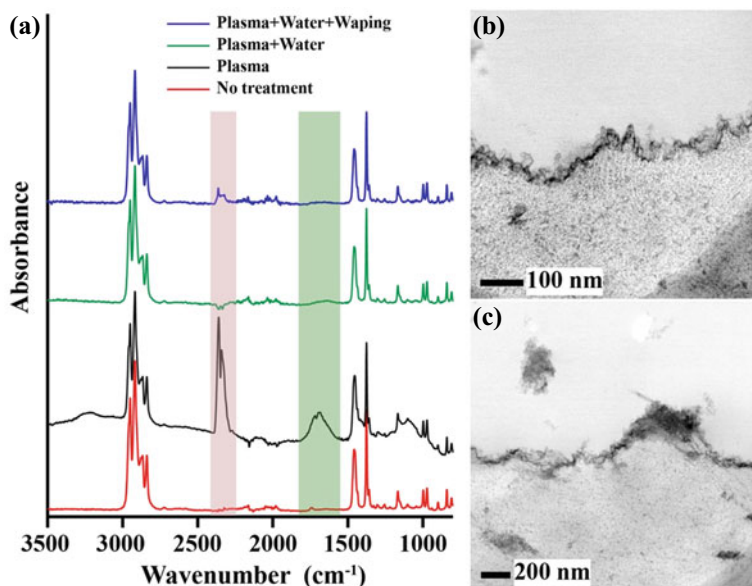


Fig. 29 ATR-IR spectra of as-prepared *iPP* (red), plasma-treated *iPP* (black), plasma-treated *iPP* washed with water (green), and plasma-treated *iPP* washed with water and rubbed subsequently with tissue paper (blue) (a). STEM-BF images of the interfaces between *iPP* and the adhesive: **b** after washing with water; **c** after rubbing with tissue paper

hand, the AB-initiated adhesive creates chemical bonds to *iPP*, which enhances the interfacial toughness remarkably.

Detailed surface chemical spectroscopy analyses are described in Chap. 5. Here, one typical result indicating the role of the chemical functional groups on adhesion is shown in Fig. 29a, which shows the ATR-IR spectra of non-treated (bottom) and plasma treated (second from the bottom). The ATR-IR spectra indicate carbonyl and hydroxyl functional group production after the plasma treatment. The third one from the bottom was obtained after washing the plasma-treated sample with water, showing the elimination of the peaks corresponding to the functional groups produced by the plasma treatment. This means that the plasma treatment causes the fragmentation of the polymers, which can be washed away from the substrate. The lap-shear bonding strength of the plasma-treated sample is 6.18 MPa, while it is 5.60 MPa after washing with water. Even with the elimination of the functional groups from the surface, the reduction of the bonding strength is limited. However, rubbing the surface with tissue paper after washing with water substantially reduced the bonding strength to be 3.13 MPa. Figure 29b and c are STEM-BF images of the interfacial region after washing with water and subsequent rubbing, respectively. No remarkable differences can be observed after washing with water in terms of the roughness of the interface, whereas, after rubbing, the roughness feature of the *iPP* surface is lost, and some fragments produced by the plasma treatment are detached from the *iPP* surface and

floated in the adhesive phase. This result strongly supports that chemical functional groups generated by plasma treatment have a limited role in adhesion enhancement.

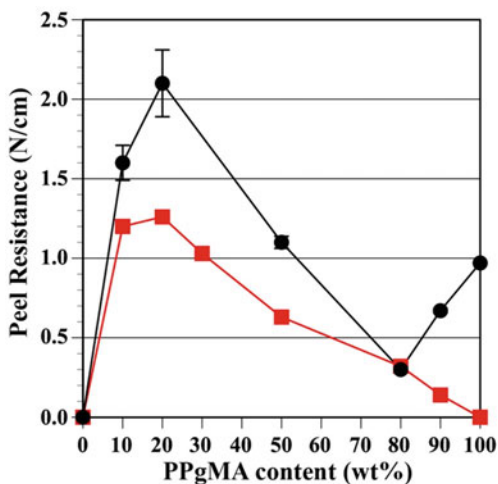
5 Formation of the Interphase Between Aluminum and Polypropylene—The Role of Reactive Functionality on Metal Bonding

The polymer–metal hybrid materials have been widely used in various industrial applications, leading to improved product design flexibility, product weight reduction, and protection of metallic surfaces in harsh environmental conditions. Polymers have been modified with chemically reactive groups to improve adhesion to the metallic adherend. It is generally believed that the formation of chemical bonds at the metal/polymer interface is the primary factor that enhances adhesion. Although detecting chemical bonding at adhesion interfaces is important in elucidating the bonding mechanism and assuring bonding reliability, obtaining direct evidence of covalent bonding is analytically challenging. In addition, adhesion performance is influenced not only by the two-dimensional metal/polymer interface but also by a three-dimensional (3D) “interphase” or “interfacial region” that possesses different properties and structural characteristics extending into the bulk materials [54, 55]. The thickness of this region remains unknown and has been the focus of extensive research. It is crucial to understand the bonding mechanism to identify the interfacial area and determine how it is created in the bonding process.

We conducted a simple adhesion experiment [53]. In this experiment, polymer films of the blends of *i*PP and PP grafted with maleic anhydride (PPgMA) are hot-pressed onto an Al sheet. The influence of the PPgMA content on adhesion is presented in Fig. 30: Pure *i*PP exhibit no adhesion to Al, but incorporating a small amount of PPgMA into *i*PP shows a remarkable increase in peeling resistance. Nevertheless, the bonding strength is reduced with a further increase in the fraction of PPgMA in the *i*PP/PPgMA blends. Based on the findings, adhesion enhancement may not be primarily attributed to interfacial chemical bonding between PPgMA and the Al surface.

The study uses *i*PP with an average molecular weight (M_n) of 67,000 and weight average molecular weight (M_w) of 250,000. PPgMA with different molecular weights are also used: One has an M_w of 9100 and a 3 wt.% MA content (*l*-PPgMA), while the other had an M_w of 153,000 and 3 wt.% MA content (*h*-PPgMA). The PPgMA was synthesized through free radical grafting of MA onto the PP backbone with peroxide during melt compounding. It is assumed that MA is mainly grafted onto the tertiary carbon of the PP backbone [56]. The *i*PP and PPgMA were melt-blended for 10 min at 300 rpm using an extruder. Subsequently, the resulting blend was molded into 300 μm thick films through hot-pressing between silicon wafers at 200 °C. The films were then hot-pressed between a 0.1 mm thick Al foil and a Si

Fig. 30 T-peel resistance to Al of the blend of *i*PP and PPgMA as a function of *i*PP/PPgMA ratio. Peeling resistance is plotted against the contents of *l*-PPgMA (red) and *h*-PPgMA (black) in the *i*PP/PPgMA blends. Reprinted with permission from [53]. Copyright 2021, American Chemical Society. All Rights Reserved



wafer. According to the DSC measurements, the *i*PP/PPgMA blends are miscible as a single peak corresponding to the melting temperature is observed [57].

The experiment involved heating the samples to 210 °C at a pressure of 10 MPa for 60 min, cooling them to 100 °C with the same pressure for 10 min, and finally cooling them to room temperature. The Si wafer was easily peeled off from the PP film after cooling. The T-peel resistance of adhesive bonds was measured according to the ISO11339:2010 [58] test method to measure the bonding strength. The relationship between the PPgMA content and peel resistance was similar for *h*-PPgMA and *l*-PPgMA, with *h*-PPgMA consistently exhibiting higher peel resistance. The maximum bonding strength is observed at 20 wt.% of PPgMA, and further increases lead to a steady decrease until the PPgMA content reached 80 wt.%. For *l*-PPgMA, the peel resistance decreases continuously with increasing content until it reaches zero with pure *l*-PPgMA. However, for *h*-PPgMA, a slight increase is exhibited in peel resistance when the content increased from 80 to 100 wt.%.

5.1 Bonding Mechanism Investigated by Replica-STEM Tomography

We thoroughly examine the fracture surfaces generated during the peeling test to investigate how adding reactive functional groups to *i*PP enhances its adhesion to Al. In Sect. 2, we utilized HR-SEM to find the nanoscale failure behavior of the fracture surfaces in the polymer interfaces. In this study, we perform the replica-STEM method to quantitatively evaluate the topographical surface features, allowing us to construct accurate 3D surface structures by STEM tomography using Pt/carbon replicas as described in Sect. 2.3.3.

To study the impact of PP_gMA on the adhesion between PP and Al, we initially examined the fracture surfaces' topological structures. Four fracture surfaces are produced, as illustrated in Fig. 31i when peeling the test specimens: an Al surface (FS-I); a PP surface separated from Al (FS-II); a PP surface detached from the silicon wafer (FS-III); a Si wafer surface (FS-IV). The replica-STEM technique accurately transfers the surface topological structures to the Pt-carbon thin replica films. The films are examined using STEM in the HAADF mode with an accelerating voltage of 200 kV. As the molecular weight does not impact the bonding properties, only *h*-PP_gMA-containing blend samples are investigated in the following. In the rest of this study, *h*-PP_gMA is referred to as PP_gMA.

Figure 31a–d depict STEM-HAADF micrographs of the replica films obtained from the four fracture surfaces between *i*PP and Al (*i*PP/Al). In Fig. 31b and c, surface lamellar morphologies with widths of approximately 10 nm can be observed on both sides of the *i*PP (FS-II and FS-III). The Al and Si wafer surfaces are presented

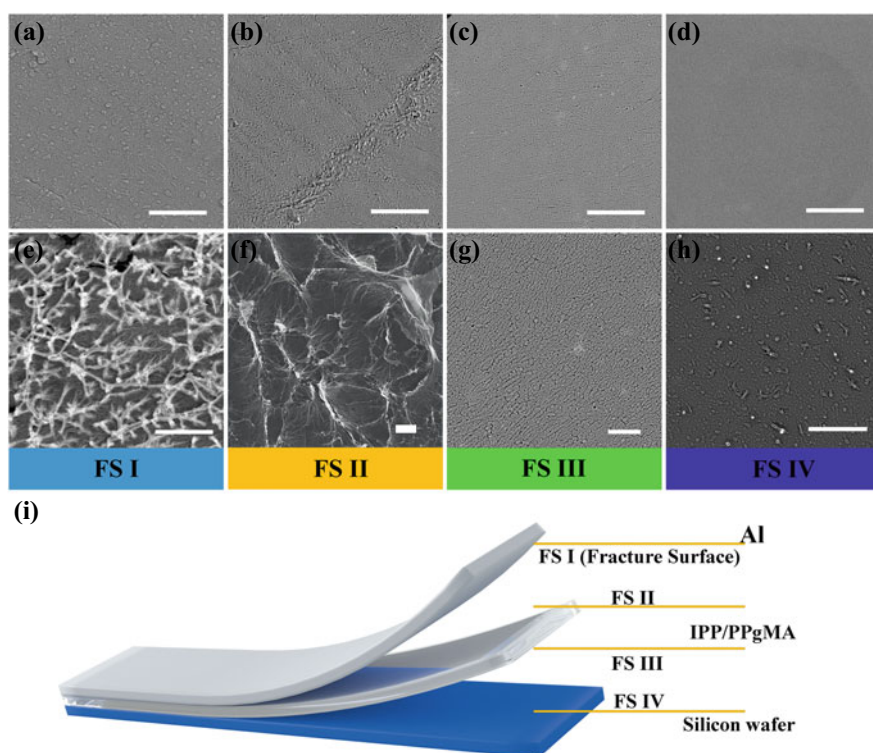


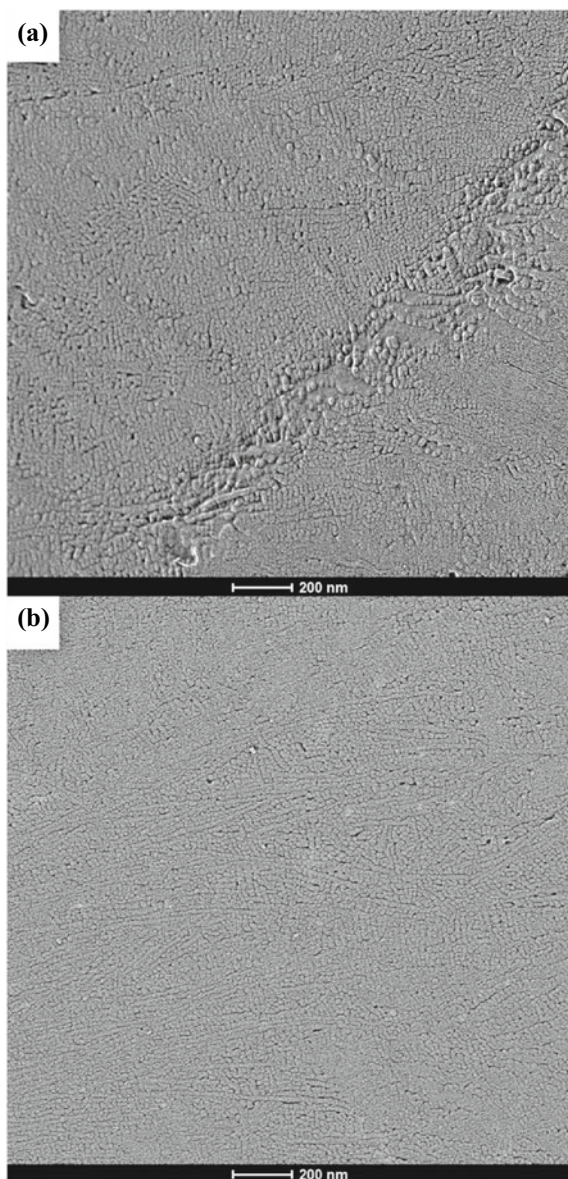
Fig. 31 STEM-HAADF images of the replica films taken from the fracture surfaces of the Al/ (*i*PP/PP_gMA)/Si wafer laminates as defined in (i): a–d fracture surfaces of an Al/*i*PP/Si wafer; e–h fracture surfaces of the lamination with the *i*PP/PP_gMA (80/20). Scale bars represent 500 nm. Reprinted with permission from [53]. Copyright 2021, American Chemical Society. All Rights Reserved

in Fig. 31a and d, respectively (FS-I and FS-IV), which appear smooth. Figure 32 provides enlarged images of Fig. 31b and c, demonstrating that the lamellar orientations on FS-II and FS-III exhibit distinct features. Specifically, the *i*PP failed from the Al foil consists of shorter lamellae, while that failed from the Si wafer contains longer lamellae. This discrepancy suggests that substrate surfaces can influence the crystallization of *i*PP despite the absence of adhesion. The lamellae on the surface attached to the Al foil grow from the Al surface, whereas those in contact with the Si wafer are randomly oriented. The Al surface significantly impacts the *i*PP crystallization more than the Si wafer. The replica images also highlight differences in the roughness of the *i*PP surface attached to the Al versus the Si wafer, reflecting the roughness of the Al foil and the Si wafer. The replica obtained from FS-I indicates the existence of small bumps less than 50 nm in diameter on the Al surface (Fig. 31a), while the FS-IV exhibits an entirely flat surface of the Si wafer (Fig. 31d). The results suggest that delicate surface structures of *i*PP can be successfully transferred to the replica, enabling observation of the crystallinity and topological features of the outermost surface of *i*PP. The Al/*i*PP interface is separated via interfacial failure, indicating no adhesion.

The incorporation of 10 wt.% of PPgMA leads to a significant improvement in the adhesion of PP to Al, as shown in Fig. 30. The fracture surfaces created by peeling the *i*PP/PPgMA (90/10) blend film from the Al substrate and from the Si wafer are shown in Fig. 31e-h. The addition of PPgMA causes substantial changes in the fracture surfaces, especially in FS-I and FS-II, where a large number of fibril-like fragments with widths of approximately 10 nm is generated on FS-I (Fig. 31e), and significant deformation of the *i*PP/PPgMA surface is observed on FS-II (Fig. 31f). In visual inspection, all samples' Al surfaces (FS-I) exhibit uniform metallic luster, implying interfacial failure. However, the STEM-replica technique indicates that a thin polymer layer with nanoscale fibril-like fragments is formed (Fig. 31e) in the failure process between the *i*PP/PPgMA blend film and the Al. Figure 33a, a zoomed-in image of Fig. 31e, shows that the entire Al surface (FS-I) is covered with *i*PP/PPgMA. Additionally, the Al/(*i*PP/PPgMA) interface exhibits asymmetric failure, as demonstrated in Fig. 31e and f. Figure 31b is a high-magnification image displaying the deformed *i*PP/PPgMA fibrils on FS-II, which are significantly larger than those observed on the Al surface FS-I. In contrast, the fracture surface of *i*PP/PPgMA separated from the Si wafer (FS-III) shows a lamellar morphology (Fig. 31g), and even with no adhesion, a small quantity of polymer adheres to the Si wafer FS-IV (Fig. 31h).

The results above suggest that the fine features on the fracture surfaces can be replicated onto thin film. While surface structures can be observed directly by SEM, of which resolution is limited due to specimen charging and damage caused by the electron beam. Conductive coatings can prevent charging but hinder the observation of fine structures, and convergent electron beams can penetrate below the surface, making it difficult to obtain true surface images [59]. In contrast, the replica-STEM technique overcomes these drawbacks and enables 3D visualization of surfaces through tomography. The video presented in Fig. 34 displays a sequence of STEM-HAADF tilt images that are obtained by incrementally tilting the sample from -60° to

Fig. 32 STEM-HAADF images of the replica films showing the surface lamellar morphologies of *i*PP: **a** *i*PP separated from the Al substrate; **b** *i*PP separated from the silicon wafer. Reprinted with permission from [53]. Copyright 2021, American Chemical Society. All Rights Reserved



+ 60° with a 2.5° interval. These images are used to reconstruct a 3D image through alignment and statistical analysis. In Fig. 35a–f, bird’s-eye and side views of the 3D reconstructed fracture surfaces of the Al sides after peeling off *i*PP/PPgMA blend films with various ratios are displayed. These images show the spatial distribution of the fibrils produced on the Al substrate. The 80/20 blend exhibits the highest density

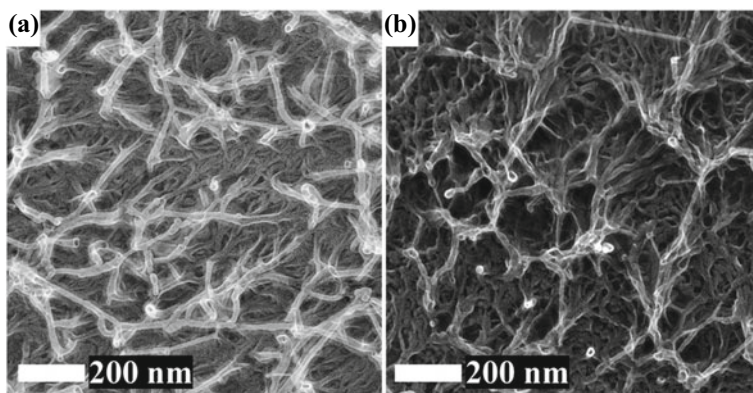


Fig. 33 Magnified STEM-HAADF images of the replicas shown in Fig. 31e and f: **a** the fracture surface of Al; **b** PP surface of *i*PP/PPgMA (90/10) blend. Reprinted with permission from [53]. Copyright 2021, American Chemical Society. All Rights Reserved

of fibrils, whereas the 100/0 blend shows no polymer fragments. The 3D visualizations also provide information on the fibrils' length, shapes, and branching, which are then transformed into thin filaments using skeletonization. Statistical analysis shows that the average thickness of the fibrils is 9.4 ± 5.1 nm.

The failure of the interfaces between the Al and *i*PP/PPgMA blend is asymmetric, as demonstrated by the highly elongated fibrils along the direction of the crack opening on the PP side of *i*PP/PPgMA 90/10, as shown in Fig. 37. The lamellar

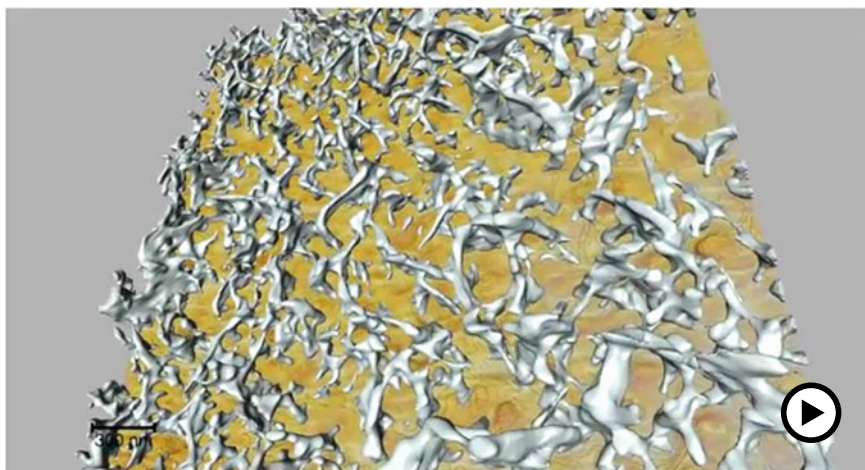


Fig. 34 A video showing a series of the STEM-HAADF tilt images acquired from -60° to $+60^\circ$ degrees with a 2.5° step, and the 3D image reconstructed after the alignment of the tilt images followed by quantitative and statistical analyses. Reprinted with permission from [53]. Copyright 2021, American Chemical Society. All Rights Reserved (► <https://doi.org/10.1007/000-ayk>)

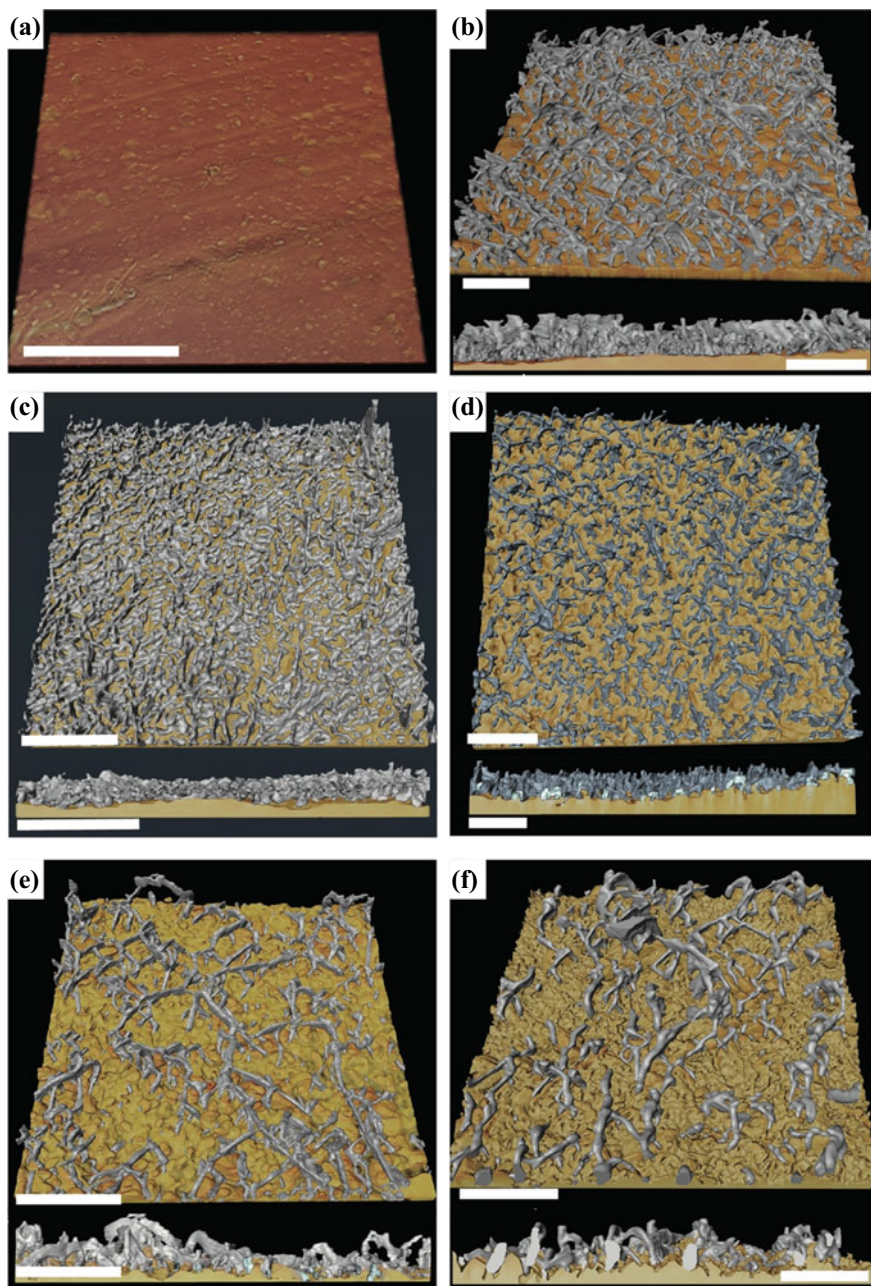
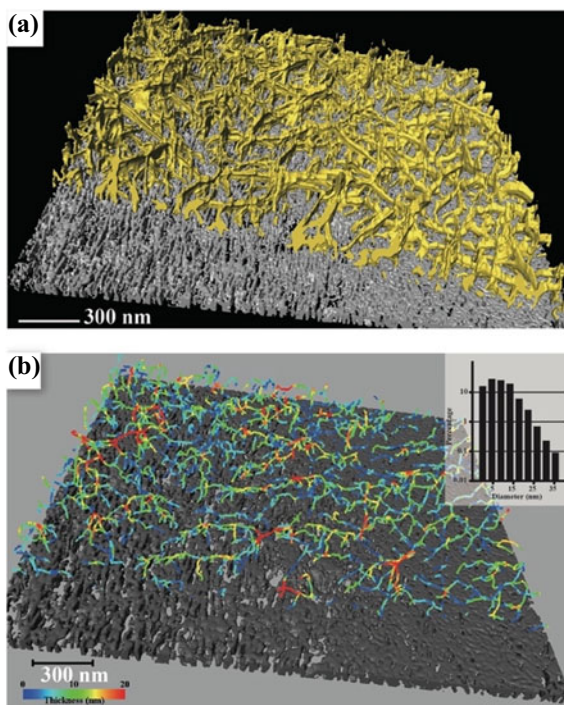


Fig. 35 Bird's-eye and side views of fracture surfaces of the Al substrate reconstructed by STEM-tomography of the replicas. Panels (a) through (f) correspond to *iPP/PPgMA* blend ratios of 100/0, 90/10, 80/20, 50/50, 10/90, and 0/100, respectively. Scale bars represent 500 nm. Reprinted with permission from [53]. Copyright 2021, American Chemical Society. All Rights Reserved

Fig. 36 3D re-constructed image of the replica representing the fracture surface of the Al surface bonded to the *i*PP/PPgMA (90/10) laminate (a) and the color map representing the fibril's thickness distribution (b). The Inset in (b) is a histogram showing the distribution of the thickness of the fibrils. Reprinted with permission from [53]. Copyright 2021, American Chemical Society. All Rights Reserved



structure with elongation along the crack opening direction is retained in the bottom part (gray), while the upper part (yellow) is largely elongated, making the crystalline structure unrecognizable. The STEM-replica technique can visualize this deep and complicated structure using rotary shadowing, which allows Pt-C deposition to reach into narrow spaces, as shown in the video (Fig. 38) [60].

Figure 39 illustrates the plot of bonding strength versus blend ratio, where the fracture surfaces of the Al side are displayed, and the corresponding images reveal the qualitative links between bonding strength and nanofibrillar formation. The 3D visualization presented in Fig. 35 enables an approximation of the volume fractions of the fibrils generated on the Al surfaces in the region predominantly occupied by the fibrils. The association between the volume fraction of the fibrils and peeling resistance is demonstrated in Fig. 40a, suggesting that the bonding strength rises as the volume fraction of fibrils increases.

Similar surface features have been observed in the failure of interfaces between glassy polymers, as discussed in Sect. 3 and reported in previous studies [17, 41, 44, 48]. In the welding of PS, for example, the thickness of the interface increases due to interdiffusion, and nano-fibrils are generated in the failure of the interfaces that form in the early stages of interdiffusion, where entanglements are insufficient to trigger crazing. The length and number of fibrils increase with increasing interfacial toughness before the failure mode transition, concluding that these nano-sized fibrils are associated with the failure of weak interfaces resulting from the interdiffusion of

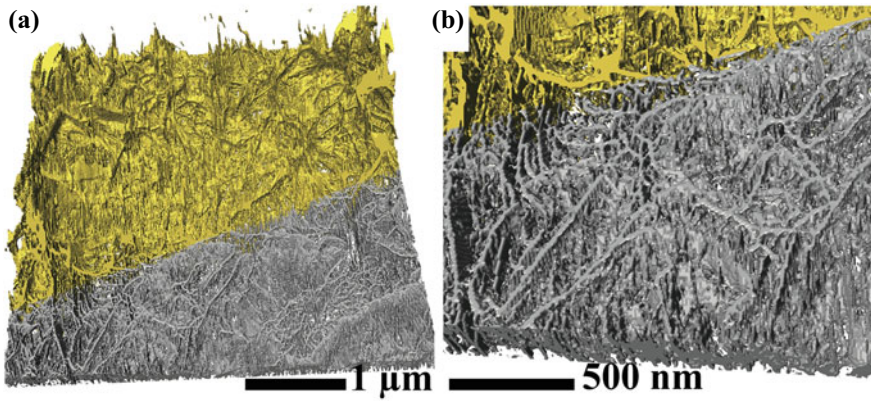


Fig. 37 The fracture surface of the PP in (*i*PP/PPgMA (90/10))/Al laminate. The yellow portion represents the outermost fractured surface, while the gray part indicates the inner parts with lamellar structures. A magnified view of (a) is shown in (b). Reprinted with permission from [53]. Copyright 2021, American Chemical Society. All Rights Reserved

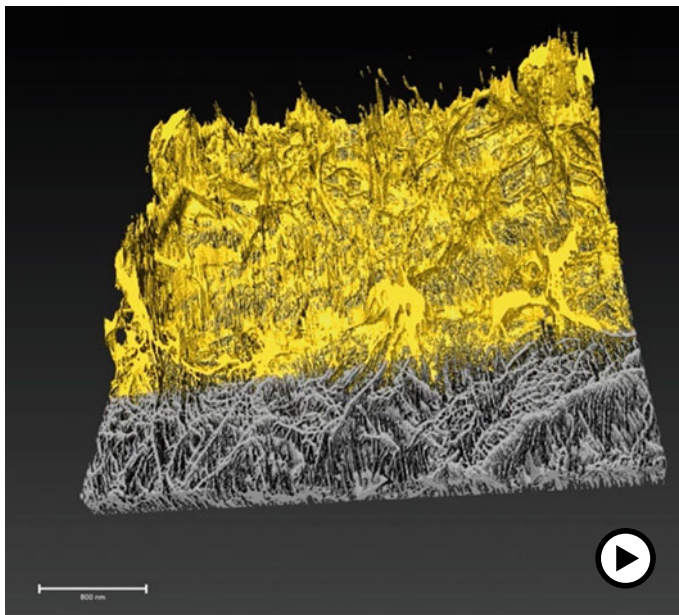


Fig. 38 A video showing the 3D structure of the fracture surface on the PP side of *i*PP/PPgMA 90/10 (▶ <https://doi.org/10.1007/000-aym>)

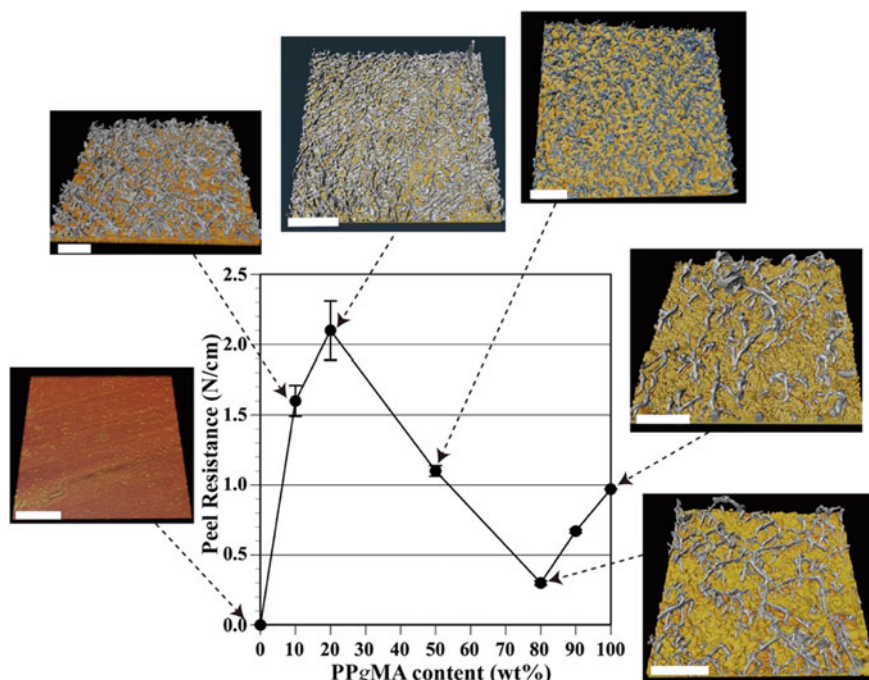


Fig. 39 Correlation between the 3D fracture surfaces constructed by replica-STEM tomography and the bonding strength between Al and *i*PP/PPgMA

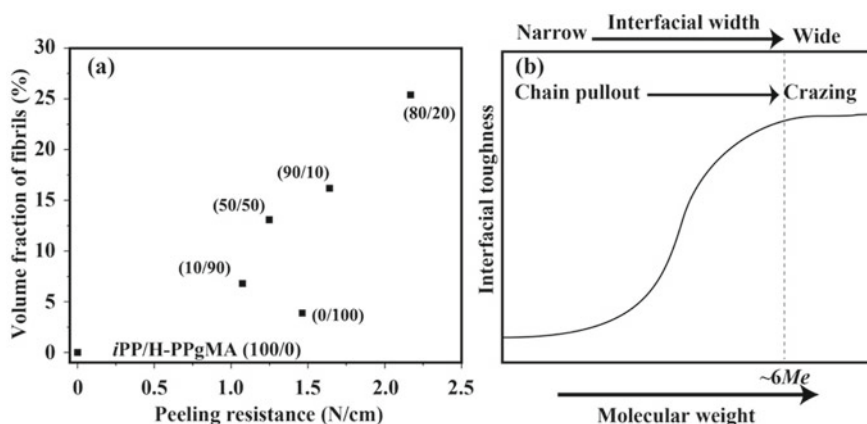


Fig. 40 Relationship between volume percentage of the fibrils produced on the Al fracture surfaces versus peeling resistance (a) and schematic representation of the dramatic increase in interfacial toughness resulting from a shift in failure mode (b). Reprinted with permission from [53]. Copyright 2021, American Chemical Society. All Rights Reserved

glassy polymers. In contrast, in the bonding of polymers to metals, interface diffusion is not possible.

Once again, we examine the bonding mechanism using the *S*-shaped curve as demonstrated in Fig. 17. For polymer–polymer adhesion, where entanglements play a crucial role, the interfacial toughness typically depends on the interfacial width. In contrast, the interfacial toughness is linked to the polymer’s molecular weight for polymer–metal adhesion, as indicated in Fig. 40b. According to the scaling analysis, failure mode transition occurs when the chain length exceeds the length associated with a molecular weight of $6Me$, where Me is the molecular weight between entanglement points. For instance, the Me of PS was reported to be 18,000, whereas that of *i*PP was 5,100–8,100. In this case, it is likely that a low-molecular-weight glassy or low-crystallinity layer formed in the region near the metal/polymer interfaces, leading to failure within that layer.

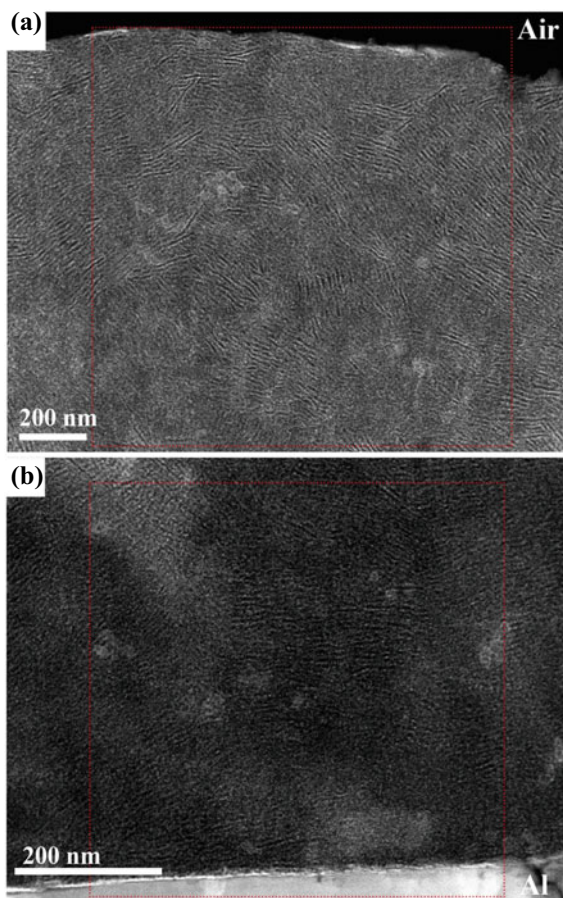
The replica-STEM technique enables us to find the generation of the nano-sized fibrils on the Al substrate when peeling off the lamination. This technique is especially effective in the point that the 3D visualization of the occurrence of the surface deformation on failure is visible. Additionally, it is interesting that the failure of polymer/metal-bonded interfaces produces surface features similar to entanglement-based polymer/polymer adhesion. We discover that a low-crystallinity and low-molecular-weight layer forms in the interfacial region, which is responsible for improving adhesion. We believe that this “soft layer” is produced due to the interfacial chemical reaction of PPgMA to the reactive moieties, such as -OH or adsorbed water on the Al surface. Furthermore, MA and Al surface’s interfacial chemical reaction leads to *i*PP with grafted carboxylic acid groups (-COOH), which may be excluded from the *i*PP crystal lamellae. The asymmetrical features of the Al and PP side’s fracture surfaces suggest gradient structures in the “soft layer” in terms of crystallinity and molecular weight. Structures with relatively low molecular weights and lower crystallinity are likely formed on the Al side, which segregates PPgMA when it is added as a minor component in the blend up to 20 wt%. The adhesion strength depends on the toughness of the “soft layer,” mainly determined by its molecular weight and crystallinity. Therefore, we conclude that chemical bonding does not achieve the enhancement of the metal/polymer adhesion. Still, chemical bonding is needed to induce the segregation of PPgMA from *i*PP, which causes the formation of the “soft layer”.

5.2 Mechanism of Interphase Formation

The replica-STEM fractography study indicated that forming a low-crystallinity and low-molecular-weight layer at the interfacial region is responsible for improving adhesion. This layer is likely produced via crystallization in the end of the hot-melt bonding process. It is likely accompanied by a change in the miscibility between *i*PP and PPgMA induced by the interfacial reaction between PPgMA and the Al surface.

The lamellae of the 80/20 wt/wt *i*PP/PPgMA blend at the interfacial region and at the free surface are inspected by STEM (Fig. 41). The lamellae of PP can be visualized by staining with RuO₄ because the amorphous region can be stained preferentially. The interlamellar amorphous region exists between the stacked lamellae in which the folded segments in a polymer chain are arranged parallel to the neighboring segments. These amorphous layers can be selectively stained, making the lamellae visible as the unstained region. Therefore, the lamellae are visible to be dark filaments between the bright amorphous layers in the HAADF mode in STEM. Notably, the visibility of lamellae in the region below the surface (Fig. 41a) is markedly clear compared to that in the interfacial region (Fig. 41b), implying that the interfacial region contains disordered lamellae. Additionally, the lamellae in the interfacial region prefer parallel orientation to the Al surface plane, while no particular lamellae orientation can be found in the region below the surface. Specifically, the “flat-on” lamellae are grown in the interfacial region, in which the chain axis is normal to the Al substrate.

Fig. 41 STEM-HAADF images showing the lamellae of *i*PP/PPgMA (80/20) blend: **a** surface side; **b** interfacial region. FFT calculations were performed for the red frames



Fast Fourier transformation (FFT) of an image allows the determination of its periodic components and their corresponding frequencies. Moreover, it identifies the preferred orientation direction of the structures within the image [61]. The FFT analyses of the lamellar structures were performed as shown in Fig. 42, which allows us to evaluate the orientation and thickness of the lamellae of PP. The FFT images were created from the area in the red flames shown in Fig. 41. The FFT image on the surface side is characterized by a broad pair of arcs (Fig. 42a), whereas that in the interfacial region is characterized by a pair of bright spots (Fig. 42b). The inverse Fourier transformations of the areas including the reflexes (peripheral arcs and spots) in the FFT images (as demonstrated in Fig. 42c and d) can produce clarified images representing the periodical structures, as depicted in Fig. 42c and d. The images also highlight the difference in lamellar orientation between the surface side and the interfacial region.

These findings suggest that the interaction between the Al surface and the *i*PP/PPgMA blend affects the growth of the lamellar during the crystallization from the isotropic melts. It has been known that lamellar crystallites exhibit preferential orientation in thin films because of their confinement and interactions with the

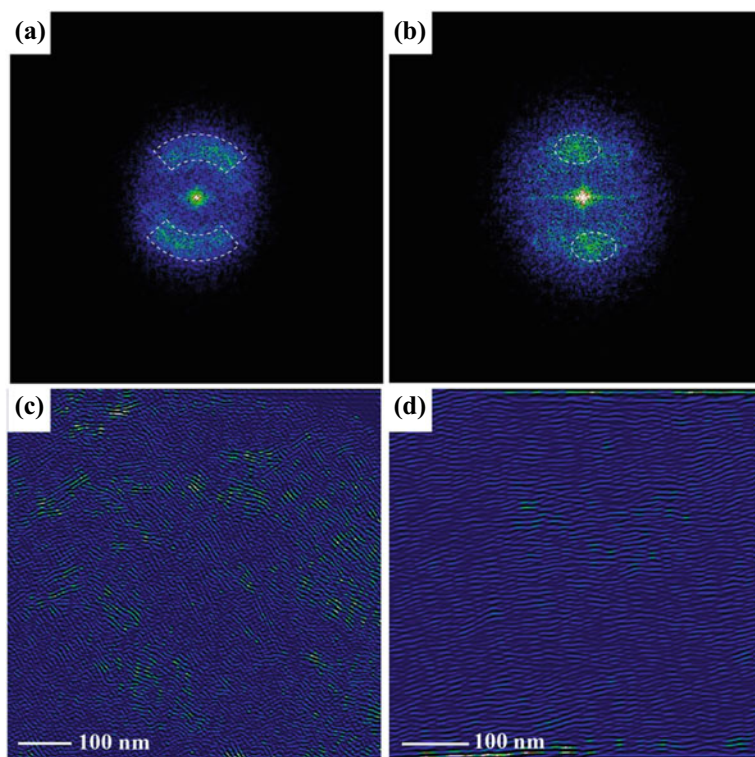


Fig. 42 FFT images (a, b) and inverse Fourier transformed images (c, d) for the regions marked by red flames in Fig. 41: a, c surface side; b, d interfacial region

substrate [62–64]. In a film with thicknesses of 100–1000 nm, they usually form “edge-on” lamellae, where the chain alignment can be parallel. They usually form flat-on lamellae in a much thinner film with thicknesses less than 100 nm. The film is much thicker than these critical thicknesses in the situation studied here. It is, therefore, presumed that the preferential “flat-on” lamellae in the interfacial region are produced by the chemical interaction between PPgMA and the Al surface.

Further details of the interphases were investigated by the localized thermomechanical responses of the cross sections of the *i*PP/PPgMA blend bonded to the Al [65]. The localized thermomechanical analysis was performed using an atomic force microscopy (AFM) instrument with a thermal probe tip to heat locally on PP, called NanoTA. NanoTA is a local analytical technique that combines the high-spatial-resolution imaging capabilities of AFM with the ability to obtain high-spatial-resolution information on the thermomechanical behavior of materials at specified positions [66, 67]. The local thermomechanical analysis by NanoTA could successfully identify the interphase between *i*PP/PPgMA blends and the Al substrate. The thermomechanical behavior near the Al/PP interface exhibited distinct differences compared to the bulk region or even the surface side of PP. The interphase extended approximately 10 μm away from the Al/PP interface towards the bulk region of PP, as described in [65].

Observations using STEM revealed that the interphase consisted of disordered “flat-on” lamellae when examining lamellar crystals. The wide interphase formation, triggered by a chemical reaction between PPgMA and the Al surface, occurs through phase separation of the blend. It’s important to note that the interfacial chemical reaction doesn’t directly enhance bonding strength but instead creates the interphase, which plays a critical role in improving bonding strength. The elucidated bonding mechanism highlights the need for careful control of cooling conditions in the bonding process to create an optimized interphase for desired bonding properties. Figure 43 illustrates the mechanism behind interphase formation during the bonding process.

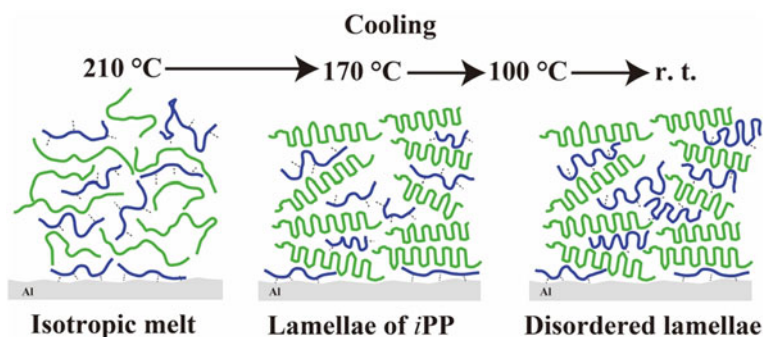


Fig. 43 Schematic illustration depicting the interphase formation during the *i*PP/PPgMA blend bonding to Al. The blue and red represent *i*PP and PPgMA chains, respectively

According to the proposed explanation, a chemical reaction takes place between PPgMA and the —OH functional groups on the Al oxide surface, as well as the adsorbed water molecules, converting MA to dicarboxylic acid. When the blend film is hot-pressed onto the Al foil at 210 °C, PPgMA selectively adheres and immobilizes on the Al surface due to the MA-Al oxide surface reaction. This preferential adsorption serves as nucleation sites for *i*PP crystallization, leading to the growth of “flat-on” lamellae in the interfacial region. As the sample cools, *i*PP initiates crystallization, forming ordered lamellae, while the converted PPgMA is expelled from the *i*PP lamellae and becomes encapsulated by them. During subsequent cooling stages, PPgMA gradually crystallizes until the sample reaches room temperature. However, the presence of surrounding ordered *i*PP lamellae may disrupt the chain folding of dicarboxylic acid-grafted PP, resulting in the production of disordered lamellae. This situation occurs when PPgMA is a minor component in the blend, typically with a composition of less than 20 wt% to achieve enhanced bonding strength.

6 Mechanism of Adhesive Bonding of Aluminum Alloys Studied by STEM-EELS/ELNES

Due to the excellent combination of mean density, high strength, and good corrosion resistance, aluminum alloys will be crucial for constructing lightweight car bodies. To understand the bonding mechanism of aluminum, the heterogeneous structures in the aluminum surface layer and its molecular-level chemistry in the bonding process must be well understood. The natural aluminum surface possesses thin oxide and/or hydroxide compounds with porous structures, of which the thickness is less than 10 nm [68]. In this work, we study chemistry at the interfaces in the adhesive bonding process of aluminum alloy with an epoxy adhesive by STEM-EELS and study the bonding mechanism [69].

6.1 Mechanism of Steam Treatment in Improving Adhesion Bonding of Aluminum

To achieve robust adhesion with durability in adhesive bonding, it is essential to identify practical, cost-effective, safe, and environmentally friendly surface treatment methods. Pretreating Al surfaces by immersing them in boiling water has been known as a suitable technique [70, 71]. We found that the bond strength of Al alloys and epoxy adhesives can be improved by a straightforward steam treatment approach, in which the Al surface is exposed to hot steam created by a commercial steam cleaner for 5 min. The effectiveness of the steam treatment on Al–Al adhesive bonding is evaluated using technical grade sheets of Al6061 alloy with a thickness of 2 mm, and lap shear strength tests are conducted using epoxy adhesives. The epoxy adhesive

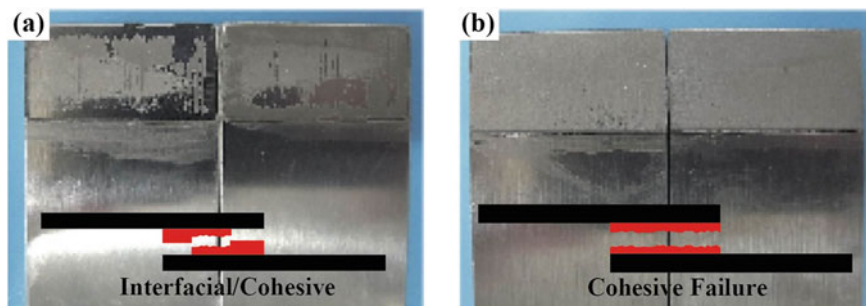


Fig. 44 Photographs of fracture surfaces showing interfacial failure with the degreased aluminum (a) and cohesive failure with the steam-treated aluminum (b). Reprinted with permission from [69]. Copyright 2022, Elsevier. All Rights Reserved

used in this study is a simple mixture of bisphenol A diglycidyl ether (DGEBA) and diphenyl diamino sulfone (DDS). When aluminum is sonicated with chloroform for degreasing, the lap shear strength is 10.8 ± 3.2 MPa. In contrast, steam-treated Al yielded 19.9 ± 1.1 and 22.8 ± 1.2 MPa. Subsequent macroscopic observation of the fracture surface revealed that the improved bond strength resulted from a change in failure mode, as shown in Fig. 44. The degreased aluminum showed a mixed “interfacial” and “cohesive” failure (Fig. 44a), while the steamed aluminum showed complete cohesive failure (Fig. 44b).

The aluminum/adhesive interfaces were inspected by STEM to investigate the mechanism of adhesive strength improvement by steam treatment. When the specimen was cut perpendicular to the interface, the projected two-dimensional (2D) image overlapped the three-dimensional (3D) structure within the interface region, so that interface details could not be observed (Fig. 45a). To address this issue, samples were prepared by cutting at an angle to the interface. The detailed procedure is depicted in Fig. 9 in Chap. 2. This gave an oblique projection showing very thin aluminum oxide regions (Fig. 45b). The interfacial structural details could be seen, revealing the roughness and porosity of the thin layer on the aluminum surface. STEM-tomography reconstruction using tilted series images of obliquely sectioned samples reveals the porous features of the aluminum oxide surface in 3D, showing that the aluminum surface exhibits a complex structure with densely packed pores of size 10–20 nm (Fig. 45c). The natural aluminum surface of industrial aluminum plates is coated with a porous 10 nm layer of oxides and/or hydroxides [69], so the surface is not atomically flat. When the surface of the used aluminum plate was observed by SEM, no significant difference was observed before and after the steam treatment.

The STEM-EDX elemental maps of C, O, and Al of the adhesive interfaces formed with either steam-treated or degreased Al are shown in Fig. 45d and e, respectively. The STEM-HAADF images on the left in each series show the surface roughness of the aluminum that the oblique sectioning can see. The Al and O elemental maps allow for identifying the oxygen-containing Al parts on the surface, and the C elemental

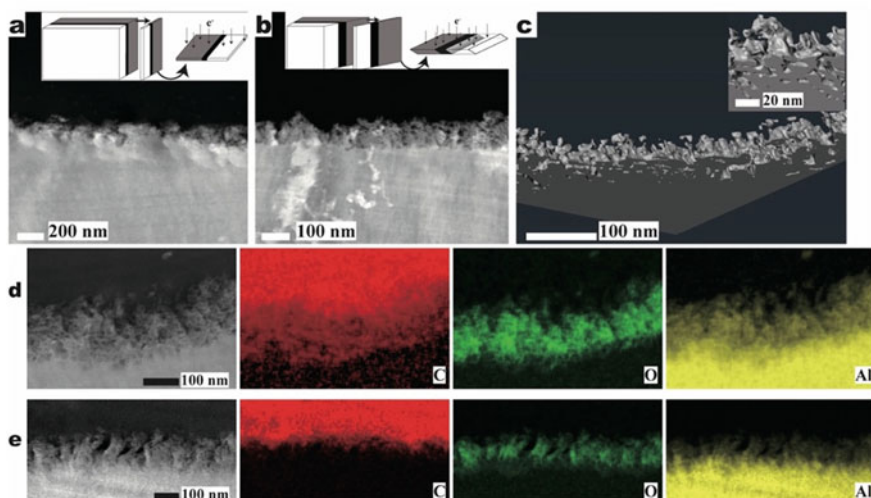


Fig. 45 Cross-sectional images of adhesive interfaces: **a, b** STEM-HAADF images of the adhesive interfaces of the steam-treated Al with a cross section (**a**) and an oblique section (**b**) at 30° to the interfacial plane as depicted in the insets in **a** and **b**; **c** 3D Al surface image re-constructed by STEM-tomography; **d, e** STEM-HAADF image and EDX elemental maps of carbon, oxygen, and aluminum of adhesive interfaces of steam-treated (**d**) and degreased aluminum (**e**). Reprinted with permission from [69]. Copyright 2022, Elsevier. All Rights Reserved

maps represent the location of the adhesive. In steam-treated aluminum, the adhesive diffuses and infiltrates the micropores of the oxide layer. In contrast, in the degreased aluminum, the adhesive only makes contact with the Al surface and does not penetrate the pores.

To examine the chemical composition of the Al plate's surface layer before bonding, thin cross sections were made from the Al plate before and after steam treatment using ultramicrotomy. These cross sections were analyzed by STEM-EELS in SI mode [72–75]. Two EELS spectra are acquired nearly simultaneously in dual EELS mode, one for the low-loss region and another for the high-loss region, including the O K-edge. The core-loss spectra's accurate energy-loss positions are obtained by drift correction of the zero-loss peak. To remove the plural scattering effects in the core-loss region using the shapes of the low-loss spectra, Fourier logarithmic deconvolution is applied to the obtained spectra. The chemical structures of the Al surface layer produced due to steam treatment are investigated using O K-edge ELNES and are shown in Fig. 46. Before steam treatment, a STEM image in HAADF mode was taken, and spectral data were obtained from the ROI shown in Fig. 46a. The maps representing the intensities in the narrow energy window of 530–535 eV are created (Fig. 46b, e and h), corresponding to the small peak in the energy loss region shown as green-shaded boxes in Fig. 46c, f, and i before the edge of the main peak. The results demonstrate that the Al surface layer underwent chemical changes due to steam treatment, as evidenced by the increased population and intensity of the small

peak in the 530–535 eV energy loss region. The results after steam treatment for 1 and 3 min are presented in Fig. 46d through 46i.

EELS spectra of various oxygen-containing Al compounds were obtained to investigate the ELNES characteristics of the O K-edge in the Al surface layer.

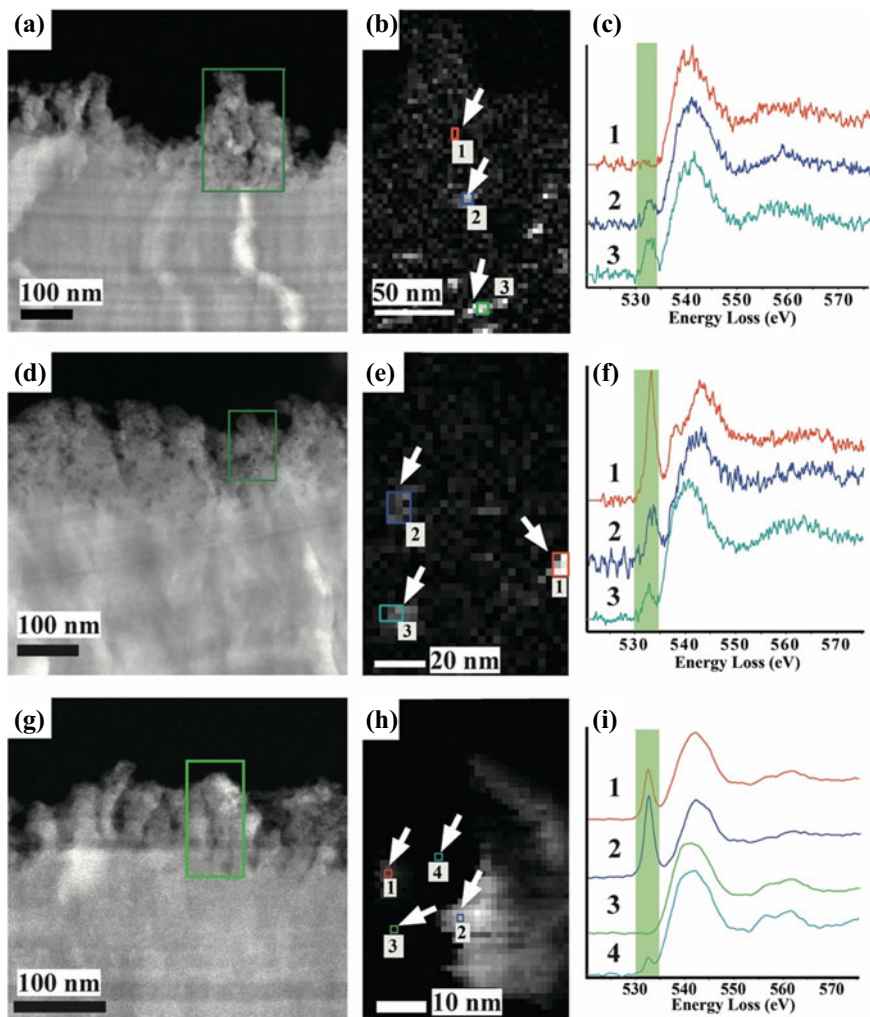


Fig. 46 STEM-EELS analysis of Al surface: **a–c** before steam treatment; **d–f** steam treatment for 1 min; **g–h** steam treatment for 3 min. The left column shows the STEM-HAADF images of the oblique sections of the surface layers. The middle column shows the chemical maps showing the distribution of $\text{Al}(\text{OH})_3$ created with the 530–535 eV energy window. The right column shows the O K-edges extracted from the ROIs indicated in the corresponding chemical maps. The green-shaded boxes indicate the 530–535 eV energy window used for the mapping. Reprinted with permission from [69]. Copyright 2022, Elsevier. All Rights Reserved

Figure 47 illustrates the O K-edges of γ -alumina (Al_2O_3), boehmite ($\text{AlO}(\text{OH})$), and aluminum hydroxide ($\text{Al}(\text{OH})_3$) powders under various irradiation conditions. The spectra were collected in the SI mode, with an interval of 10 nm and from 10×10 points, and then summed into a single spectrum. The ELNES characteristics of the O K-edges varied significantly among the three oxygen-containing compounds. γ -alumina exhibits two peaks at 550 and 563 eV energy losses, followed by the primary peak at 542 eV (Fig. 47a). Boehmite displays a broadened first peak, followed by only one peak at an energy loss of 560 eV (Fig. 47b). $\text{Al}(\text{OH})_3$ shows an intense characteristic peak at 532.6 eV, followed by two peaks at 540 and 560 eV energy losses (Fig. 47c). Despite significantly higher irradiation doses than the sample acquisition condition (a probe current of 160 pA for 500 ms), no significant changes in the ELNES features are observed. Thus, the O K-edge ELNES can be utilized to identify the chemical compositions produced in the Al surface layers, as these characteristic features are often utilized as fingerprints for chemical characterization by EELS and ELNES. They can assist in identifying those compounds in the thin, heterogeneous surface layer of technical Al substrates [76]. The emergence of peaks in the 530–535 eV energy loss region in Fig. 46 suggests $\text{Al}(\text{OH})_3$ in the ROIs indicates that the steam treatment produces -OH functional groups in the Al surface. Hydroxylation of aluminum surfaces has increased their wettability and chemical reactivity [70, 71, 77, 78]. Therefore, introducing hydroxyl functional groups through the steam treatment is responsible for improving adhesion strength.

It is challenging to differentiate between $\text{Al}(\text{OH})_3$ and $\text{AlO}(\text{OH})$ in XPS spectra because their spectroscopic information is usually similar. However, in EELS, the chemical states of aluminum in metallic, oxide, and hydroxide Al compounds are

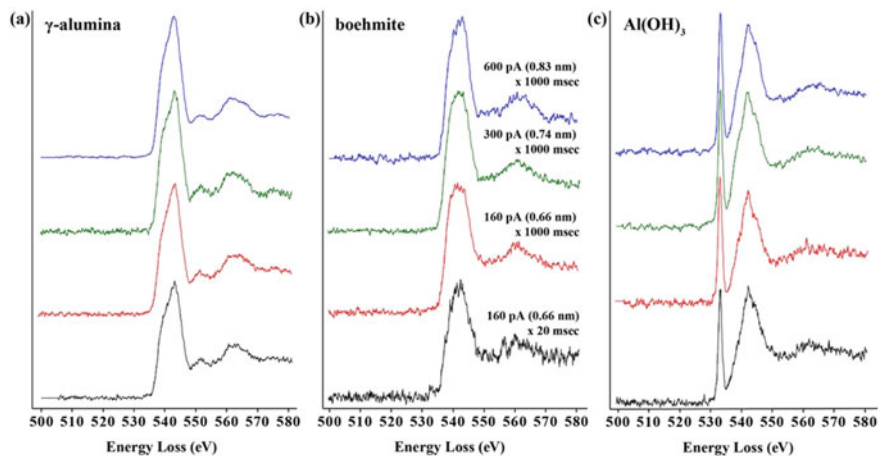


Fig. 47 O K-edge ELNES obtained from the powder samples: **a** γ -alumina; **b** $\text{AlO}(\text{OH})$ (boehmite); **c** $\text{Al}(\text{OH})_3$. Irradiation dose increases from lower to upper. All the spectra are presented after the background subtraction by fitting the pre-edge regions with a power law function. Reprinted with permission from [69]. Copyright 2022, Elsevier. All Rights Reserved

reflected in the plasmons-loss and core-loss regions of Al L_{23} - and O K-ionizations as shown in Fig. 2.5 in Sect. 2. The Al L_{23} -edges clearly show that the ionization edge of metallic aluminum appears at a lower energy (72 eV) than aluminum compounds. The three aluminum compounds exhibit ionization edges between 75 and 76 eV and two major peaks near the edges at about 80 eV and 84 eV. The peak at the onset of the edge consists of the shoulder on the lower energy side. Introducing a hydroxyl group into γ -alumina causes the peak at 79.5 eV to shift towards higher energies, resulting in another peak at 77.5 eV in $\text{Al}(\text{OH})_3$. The fine structures in the Al L_{23} -edges of the three Al compounds represent the difference in Al atomic coordination. A first-principles calculation of γ -alumina revealed that the two peaks near the edge at 77.5 and 79.5 eV originate from tetrahedrally and octahedrally coordinated Al, respectively [79].

STEM-EELS/EDX simultaneous analysis was employed with a point-to-point distance of 3 nm and an acquisition time of 0.5 s to examine the interface after bonding. Figure 48 presents the EDX elemental maps and O K-edges obtained from different regions at varying distances from the interface. The STEM-EDX elemental maps of C, O, and Al (middle panel) demonstrate that the adhesive molecules fill the nanopores in the Al surface layer. The O K-edge acquired from the ROI in close proximity to the interface (upper spectrum) shows ionization edge at 530 eV before the edge at 535 eV, which originates from the oxygen in the epoxy. The characteristic sharp peak at 532.6 eV vanished entirely when compared with the EELS spectra collected from the sample before bonding as shown in Fig. 46. The hydroxyl functional group in $\text{Al}(\text{OH})_3$ is removed after bonding, indicating that the Al surface is dehydrated. As a result, a chemical interaction between the hydroxylated aluminum surface and the epoxy adhesive arises after bonding.

To explore the interfacial interaction, the ELNES of Al L_{23} -edges in the adhesive bonding of the steam-treated and the degreased aluminum are examined carefully, as shown in Fig. 49. These were obtained by recording EELS and EDX spectra simultaneously in dual EELS- and SI-mode, with a point-to-point distance of 1 nm

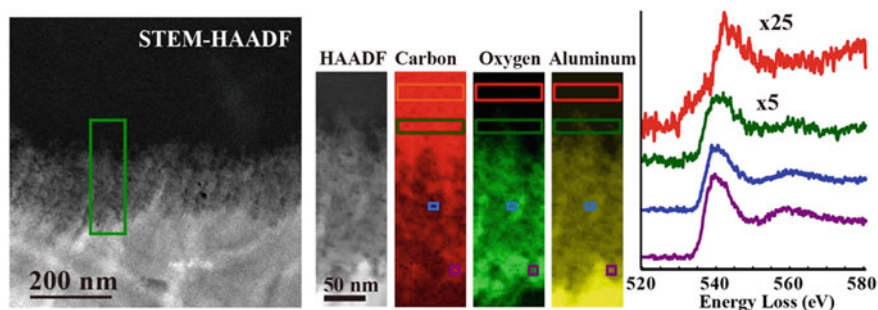


Fig. 48 A global STEM-HAADF image, STEM-EDX elemental maps for the ROI marked in the global STEM-HAADF image, and EELS O K-edges extracted from the ROIs indicated in the EDX elemental maps of the interfacial region between the adhesive and steam-treated A. Reprinted with permission from [69]. Copyright 2022, Elsevier. All Rights Reserved

and an acquisition time of 0.1 s. In the steam-treated sample (Fig. 49a), most of the spectra except for the lowest one display a characteristic ELNES consisting of two distinct peaks at 85 and 88 eV in the energy range of 85–90 eV indicated as the green-shaded boxes. Conversely, the degreased sample has no apparent characteristic ELNES (Fig. 49b). This ELNES pattern is likely the outcome of the interaction between the hydroxy groups on the Al surface and the adhesive, which differs from the ELNES acquired in the reference aluminum compounds presented in Fig. 2.5.

To gain a deeper understanding of the ELNES observed in the Al L_{23} -edge spectra, STEM analyses were performed for the single component of the epoxy (DGEBA) and the amine (DDS). The Al plates were coated with liquid DGEBA, 10 wt% DDS acetone solutions, or an organophosphate (HDPA), followed by annealing at 100 °C for 1 h. HDPA has been known to be effective in promoting the adhesion of epoxy adhesives to Al [80]. After rinsing the surfaces by ultrasonication with toluene, acetone, and ethanol, thin cross sections containing the aluminum surface were examined using STEM-EELS/EDX in SI mode. Figure 50a shows the surface region of steam-treated Al before bonding, where the metallic and oxide parts are differentiated. Despite vigorous rinsing, small amounts of each coated material are found on the Al surface (Fig. 50b–d), as evidenced by EDX elemental mapping, where

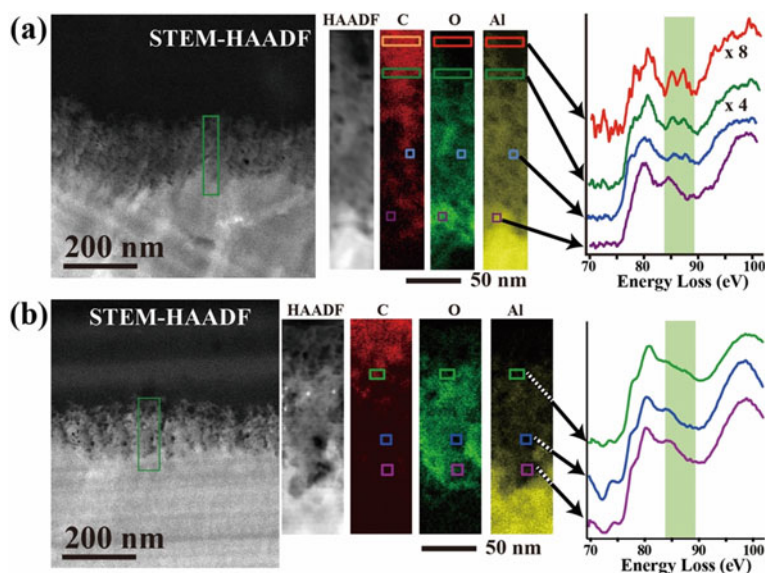


Fig. 49 The EELS spectra of Al L_{23} -edges obtained from the interfacial area: **a** interface between steam-treated Al and the adhesive; **b** interface between degreased Al and the adhesive. Each panel displays a global STEM-HAADF image (*left*), a STEM-HAADF image, and STEM-EDX elemental maps for the ROI specified in the global STEM-HAADF image (*middle*), and the Al L_{23} -edges extracted from the ROIs indicated in the EDX elemental maps (*right*). The ELNES feature indicating the interfacial chemical interaction is shown in green-shaded boxes. Reprinted with permission from [69]. Copyright 2022, Elsevier. All Rights Reserved

red pixels indicate metallic aluminum, green indicates oxygen, and blue indicates carbon. Figure 50b and c show the location of DGEBA and DDS, respectively. In Fig. 50d, it can be observed that HDPA adsorbs onto the oxygen-rich aluminum layer, depicted as a phosphor (P) elemental distribution. The ELNES characteristics of Al L_{23} -edges from these samples are compared to those of the Al/(DGEBA/DDS) interface in Fig. 50e. No distinct features are detected in the 85–90 eV energy loss region from the surface region of the Al (top spectrum) before bonding. However, two 86 and 88 eV peaks are observed in that same region after bonding (second top spectrum). While the ELNES feature in the 85–90 eV energy loss region is visible in the spectra for DDS alone, it is absent in the spectra for DGEBA alone. This suggests that the interaction between the amine and hydroxy groups present on the aluminum surface primarily drives the chemical interaction.

The O K-edge ELNES results of the aluminum surface treated with steam indicate the absence of surface hydroxy groups after bonding. The Al L_{23} -edge ELNES studies suggest that the bonding between the epoxy/amine adhesive and the aluminum occurs primarily due to the hydroxy groups on the aluminum surface and the amine component in the adhesive. Considering the surface-activation scheme of HDPA as

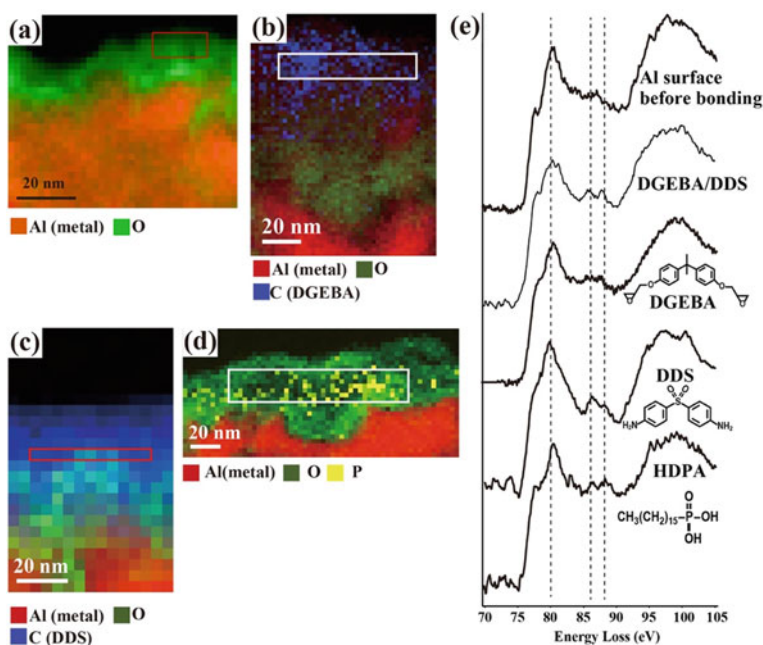


Fig. 50 Compositional maps of cross sections of aluminum surfaces: **a** before bonding; **b, c, d** after the adsorption of DGEBA, DDS, and HDPA, respectively. Red pixels represent the metallic Al distributions by EELS, and the green, blue, and yellow pixels represent O, C, and P elemental distributions by STEM-EDX; **e** ELNES of Al L_{23} -edges extracted from the ROIs indicated in the corresponding images. Reprinted with permission from [69]. Copyright 2022, Elsevier. All Rights Reserved

proposed in Fig. 51a [80], and based on the ELNES analysis and the previous SKP [70] and SFG studies [81], it can be inferred that chemical bonding at the adhesive interface occurs via acid–base interaction between the hydroxyl group on the aluminum surface and the secondary or tertiary amine in the adhesive molecules as shown in Fig. 51b. However, such bonding might not be sufficient to enhance adhesion strength, as the interaction energy of the bond is much lower than that of covalent bonds. In reality, the improvement in adhesion strength is achieved by the diffusion of adhesive molecules into the nanopores of the Al surface layer rich in hydroxy groups, which increases mechanical resistivity against applied shear stress, resulting in cohesive failure. Although acid–base interaction plays a crucial role in facilitating the diffusion of adhesive molecules into the Al porous surface layer, it does not directly enhance adhesion strength. The enthalpy-driven diffusion of adhesive molecules into the micropores of the Al surface layer results in the spontaneous diffusion of the adhesive molecules due to the acid–base interaction. Regarding polymer–polymer diffusion at the interface, dissimilar miscible polymer pairs demonstrate fast interdiffusion due to thermodynamic acceleration as stated in Sect. 2. In such cases, the positive enthalpy gained by mixing leads to more rapid diffusion compared to entropy-based interdiffusion between identical polymer pairs.

According to our findings, surface hydroxylation by steam treatment is a straightforward approach to improving the bonding strength of technical aluminum alloy substrates. Our analysis of the O K-edges using ELNES reveals the heterogeneous chemical nature of the oxide/hydroxide layer on the aluminum surface, which displays intricate nanoporous structures with a spatial resolution of less than 5 nm. The observed increase in adhesion strength is due to the penetration of adhesive molecules into the nanopores on the aluminum surface, leading to a shift from interfacial failure to cohesive failure. ELNES analysis of the Al L₂₃-edges allowed us to identify the chemical bonds created through acid–base interactions between the

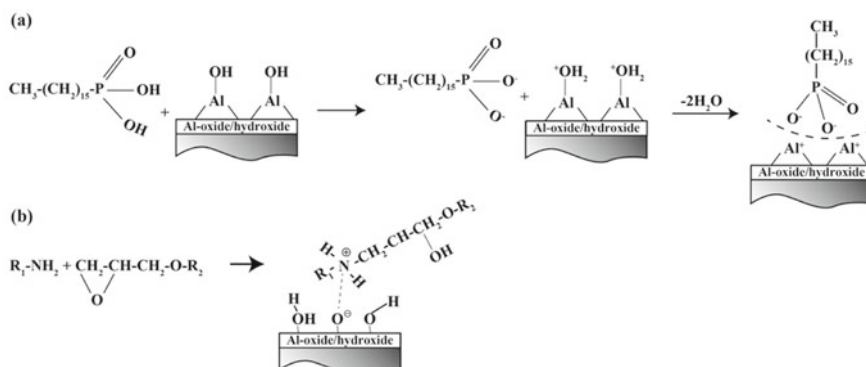


Fig. 51 Schematic representation of the acid–base interactions between adsorbed molecules and a hydroxylated aluminum surface: **a** Al surface adsorbs HDPA; **b** hydroxyl groups on the aluminum surface interact with the secondary amine in an epoxy adhesive. Reprinted with permission from [69]. Copyright 2022, Elsevier. All Rights Reserved

amino group of the adhesive and the hydroxyl groups on the aluminum surface. Although this weak bonding may not directly contribute to the improved adhesion strength, it facilitates the spontaneous penetration of adhesive molecules into the pores by means of thermodynamically favored acid–base interfacial interactions [18, 30, 82, 83].

6.2 Role of the Chemical Bonding on Interfacial Toughness Between Aluminum and Epoxy Adhesive

The extent to which chemical bonding and mechanical interlocking contribute to the bonding strength attained has yet to be completely comprehended. To address this concern, more comprehensive EELS/ELNES research was employed with an atomically flat aluminum oxide substrate, with a discussion on the impact of surface roughness and chemical bonding on adhesive bonding [84]. DGEBA, triethylenetetramine (TETA), and 2,4,6-tris(dimethylaminomethyl)phenol (TDAMP) were mixed stoichiometry at the molar ratio of 3/1 (5.7/0.72 wt/wt) and with 3 wt% of TDAMP. The curing condition of the adhesive was at 100 °C for 30 min. 50–100 nm thick oxidized Al thin film sputtered on a CaF₂ plate was used for a naturally oxidized Al model surface. The CaF₂ substrate with coated oxidized Al was ultrasonicated in ethanol for 10 min, followed by UV/ozone treatment for at least 20 min to serve a hydrocarbon-contamination-free surface before the coating of the adhesive.

Figure 52a shows a STEM image of a cross section of the specimen in STEM-HAADF mode, where the cured adhesive is coated on the AlO_x thin film sputtered on the CaF₂ substrate. Observing the cross section confirms that the uniform sputtered Al film is formed on the CaF₂ substrate without noticeable defects. A ROI indicated as a green box in Fig. 52a was inspected by STEM-EDX/EELS simultaneous analysis with a point-to-point distance of 2 nm and the acquisition time of 0.1 s, providing 86 × 25 EDX and EELS spectra. Figure 52b is an EDX elemental map of the ROI showing the carbon (red) and aluminum (blue) elemental distributions. Al L₂₃-edges were extracted from the regions with 2 nm width parallel to the interface as indicated in Fig. 52b. Figure 52c shows the background-subtracted Al L₂₃-edges extracted from the three regions, where the regions and the corresponding spectra are shown with the same colors. Those spectra show intensity fluctuations in the energy loss region beyond the ionization edge at 75 eV, especially in the energy loss range from 85 to 90 eV. As found in the technical Al alloy plate, the spectra extracted from the interface (orange) exhibit a characteristic ELNES in the energy range of 85–90 eV, where two distinct peaks at 85 and 88 eV are presented. The second layer (green) from the interface exhibits the same feature, but the intensities of those peaks become lower, while in the bulk part (blue), those peaks disappear, and a broad peak appeared instead. It is also noticed that the maximum peak at 79.5 eV in the spectra extracted from the interfacial region is shifted toward higher energy. The Al L₂₃-edge ELNES,

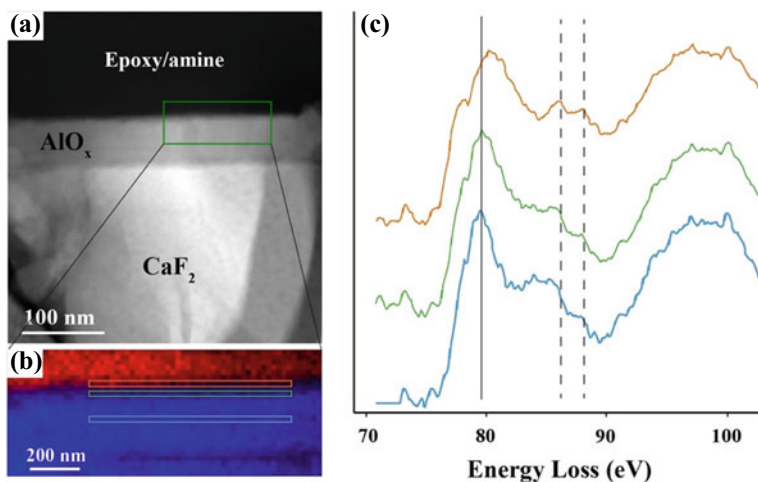


Fig. 52 STEM-EELS/ELNES analysis of the interface between the cured adhesive and the oxidized Al thin film: **a** STEM-HAADF image of a cross section of Al-sputtered film on CaF_2 covered with adhesive; **b** STEM-EDX elemental map representing carbon (red) and aluminum (blue) distributions in the ROI indicated in **a**; **c** Al L_{23} -edge EELS spectra extracted from the regions indicated in **b**. The spectra and the regions are shown as the same color

therefore, indicates that the chemical interaction between the sputtered AlO_x film and the adhesive influences the Al atomic coordination.

Figure 53 shows the O K-edge ELNES analysis of a cross section including the adhesive layer, sputtered Al thin film, and CaF_2 plate. An ROI indicated in the STEM-HAADF image (Fig. 53a) was inspected with a point-to-point distance of 5 nm and an acquisition time of 0.5 s, which provided 20×7 EDX and EELS spectra. Figure 53b shows the EDX elemental maps showing the oxygen, aluminum, carbon, and calcium distributions, and O K-edge EELS spectra extracted from the 5 nm thick layers as indicated in the EDX oxygen map (left panel in Fig. 53b) are presented in Fig. 53c. The extracted four spectra exhibit different ELNES features. The sharp peak at 532.6 eV is shown with different intensities, and the following broad peak in the 535–545 eV energy loss range exhibits different shapes. The upper layer contact with the adhesive (layer 1) does not have the sharp peak at 532.6 eV, while the second and the third layer (layers 2 and 3, respectively) shows the peak with the highest intensity of the third layer. Considering the ELNES features of O K-edges of the three reference samples, we can identify that the extracted EELS spectra 1 is similar to the boehmite spectra, and spectra 3 is identical to the $\text{Al}(\text{OH})_3$ spectra. The fact that only the interfacial layer contact with the adhesive gives the boehmite-like ELNES feature indicates that the hydroxy groups on the Al-sputtered thin film surface are consumed due to the chemical reaction with the adhesive.

STEM-EELS/ELNES analysis of the flat interface formed between the model Al oxide sputtered film and the epoxy/amine curing mixture can more clearly reproduce the results obtained with the technical Al plate as stated in Sect. 6.1. The sample used

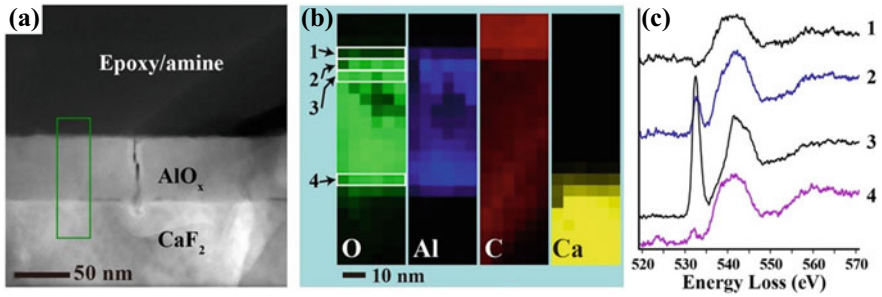


Fig. 53 O K-edge STEM-EELS/ELNES analysis of the interface between the cured epoxy/amine and AlO_x : **a** STEM-HAADF image of a cross section of AlO_x sputtered film on CaF_2 covered with epoxy/amine-cured adhesive; **b** STEM-EDX elemental maps representing oxygen (green), aluminum (blue), carbon (red) and calcium (yellow) distributions in the ROI indicated in; **c** O K-edge EELS spectra extracted from the regions shown in (b)

in this experiment can be used for other instrumental measurements, such as XPS, SFG, and Kelvin probe measurements, which support the results obtained in this study. The details will be reported elsewhere.

To evaluate the contribution of the chemical bonding, the interfacial fracture toughness between the AlO_x sputtered film and the epoxy was measured using the specimen geometry depicted in Fig. 54a, and the ADCB test was carried out. The Al thin film was sputtered on a polycarbonate (PC) plate, and the adhesive was molded onto the PC plate using a silicone rubber mold. The test was performed by the procedure stated in Sect. 3. The G_C values of the adhesive joint of technical Al plate (Al1000) were also measured by the wedge-test [85] using the symmetrical DCB specimens as shown in Fig. 54b, where the thickness, width, and length of the specimen are 3, 25, and 150 mm, respectively. The plates were preliminarily treated with sodium hydroxide aqueous solution (ph12) at 60 °C for 10 s and then with nitric acid for 10 s to remove the natural oxide layer, followed by UV/ozone treatment before bonding. After bonding, an Al wedge having 25 mm width, 30 mm length, and 1 mm thick is driven into pre-crack 30 mm from the edge to create an interfacial crack. After the initial crack made by the insertion of the wedge is stabilized, G_C is calculated.

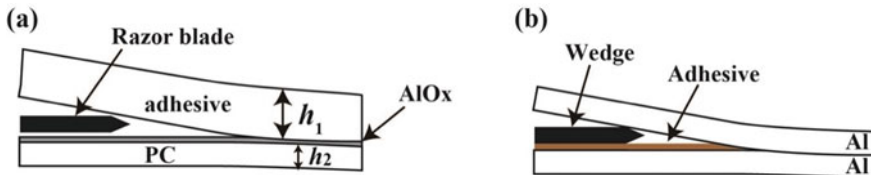


Fig. 54 Schematic illustrations of the specimens for the interfacial critical energy release rate measurements, G_C , for adhesive/sputtered Al thin film interface (a) and technical Al plate/adhesive interface (b)

The test was performed with five specimens and obtained G_c values of $3.8 \pm 1.5 \text{ J/m}^2$. After the tests, the fracture surfaces were inspected by SEM, and no topographic surface features were found on both surface. This suggests that the failure occurs at the adhesive/ AlO_x interface without noticeable deformation of the adhesive. The interfacial toughness between the technical Al plates, on the other hand, is calculated to be $129.2 \pm 17.9 \text{ J/m}^2$.

Work of adhesion (W_{adh}) can be estimated by measuring contact angles using three probe liquids. Surface energies of the sputtered Al substrates (γ_{Al}) and the cured adhesive (γ_{ad}) are determined from contact angles of water, diiodooctane, and ethylene glycol in the framework of acid–base theory [86] In this theory, total surface energy (γ^{total}) is given by

$$\gamma^{\text{total}} = \gamma^{\text{LW}} + 2\sqrt{\gamma^+ \gamma^-} \quad (11)$$

where γ^{LW} , γ^+ , and γ^- denote Lifshitz–van der Waals, Lewis acid, and Lewis base components, respectively. Using the Young–Dupré Eq. (12), respective components of the surface energies of a substrate ($\gamma_{\text{S}}^{\text{LW}}$, γ_{S}^+ , γ_{S}^-) were calculated from the parameters of the three probe liquids ($\gamma_{\text{L}}^{\text{LW}}$, γ_{L}^+ , γ_{L}^-) and experimental contact angles (θ) of respective liquids.

$$\frac{\gamma_{\text{L}}^{\text{total}}(1 + \cos \theta)}{2} = \sqrt{\gamma_{\text{S}}^{\text{LW}} \gamma_{\text{L}}^{\text{LW}}} + \sqrt{\gamma_{\text{S}}^+ \gamma_{\text{L}}^-} + \sqrt{\gamma_{\text{S}}^- \gamma_{\text{L}}^+}. \quad (12)$$

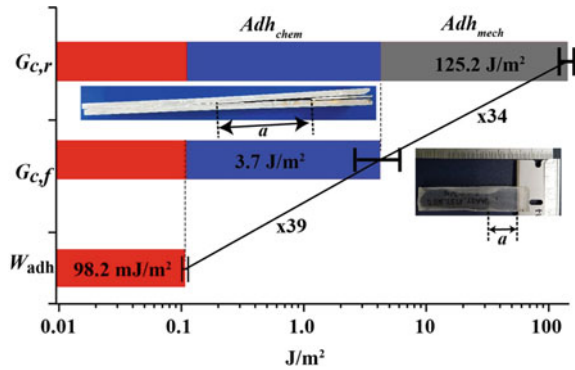
The values are used to calculate W_{adh} using the following Eq. (13):

$$W_{\text{adh}} = 2\sqrt{\gamma_{\text{Al}}^{\text{LW}} \gamma_{\text{ad}}^{\text{LW}}} + 2\sqrt{\gamma_{\text{Al}}^+ \gamma_{\text{ad}}^-} + 2\sqrt{\gamma_{\text{Al}}^- \gamma_{\text{ad}}^+}. \quad (13)$$

Figure 55 compares three adhesion energies obtained throughout the experiments. The interfacial fracture energy between the flat AlO_x substrate and the adhesive ($G_{c,f}$) is 39 times larger than the W_{adh} represented by Lifshitz–van der Waals and Lewis acid/base interactions. The contribution of chemical bonding may achieve this enhancement. The interfacial fracture energy between the technical Al plates and the epoxy adhesive ($G_{c,r}$), on the other hand, is 34 times larger than $G_{c,f}$. Therefore, the contribution of the mechanical bonding owing to the surface roughness of the Al plate is significantly more significant than that of the chemical bonding.

The toughness of interfaces between dissimilar polymers has been well investigated by the reinforcement of block copolymers (BC), of which components are identical to the polymers to be bonded. The interface between polymer A and polymer B reinforced with an A–B diblock polymer can be considered a model of the interface strengthened by chemical bonding, and the relationship between the areal density of BC at the interface and the interfacial toughness has been extensively discussed [87, 88]. In the polymer/polymer adhesion reinforced by BC, the interfacial toughness can be enhanced to more than 100 J/m^2 due to the energy dissipation through the deformation of the polymers at the crack tip via crazing if the BC chains are well

Fig. 55 Roles of the chemical and the mechanical bonding on the adhesion of Al and an epoxy adhesive. The work of adhesion (W_{adh}), the interfacial fracture energies between the flat oxide Al substrate and the epoxy adhesive ($G_{c,f}$), and between the Al technical plate and the epoxy adhesive ($G_{c,r}$) are compared. The corresponding test specimens are shown therein



entangled at the interface between the polymers. In contrast to the polymer/polymer adhesion, the interfacial toughness between the AlO_x and the adhesive was not sufficiently enhanced by the chemical bonding. This suggests that sufficient deformation of the metal/polymer interface is not expected by chemical bonding. Our result indicates that the effect of the chemical bonding is limited for the adhesion of Al, and the mechanical bonding achieved by the surface roughness is more effective.

7 Metal–plastic Direct Bonding by Injection Nano-Molding—Interfacial Structures and Testing Joint Performance

A novel technique for joining metal and plastic without adhesive has been developed, utilizing a surface treatment process that creates small pores on the metal surface. Known as Nano-Molding Technology (NMT), this is a method of directly molding plastic by inserting surface-modified metal into a mold [89–91]. Metal–plastic hybrids can be created using various combinations of metals such as Al, Cu, Ti, Mg, and plastics such as polyphenylene sulfide (PPS), polyamide (PA), and PP. The polymer chains infiltrate the nano-sized pores on the metal, yielding strong joint strength. This technique allows for fast assembly of metal and plastic with high design flexibility, but the size of the products is mainly limited by mold size. Another attractive feature of this joining technique is that cost reduction can be achieved in the case of many products being repeatedly manufactured. The new joint technology requires a thorough understanding of the joint mechanism and proper evaluation methodology to ensure safety and reliability. In this study, the joint process of PPS and Al5052 is investigated by STEM and XPS, and new test methods to evaluate the joint performance and assess environmental durability are developed.

The test specimens for the evaluation were prepared by insert-injection molding of PPS onto a surface-modified Al5052 plate at the process temperatures of 290–330 °C and the mold temperature of 120 °C. Two types of surface structures of Al5052 were

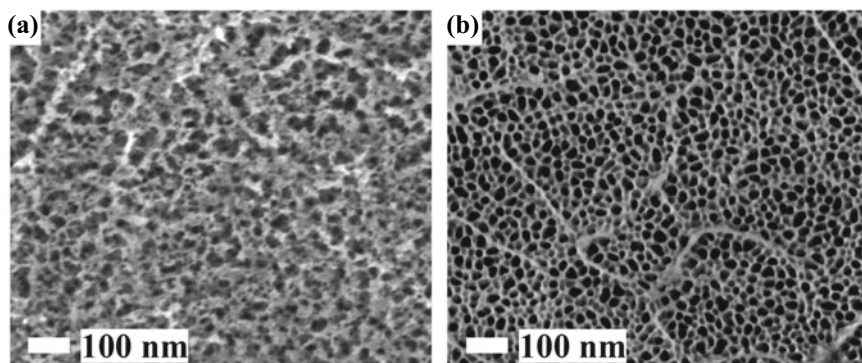


Fig. 56 SEM micrographs showing the aluminum surface porous features: **a** NMT1; **b** NMT2. Reprinted with permission from [78]. Copyright 2020, EDP Sciences. All Rights Reserved

prepared by the chemical treatment developed by Taisei Plas Co., Ltd. [89]. Those two are different in terms of the pore size, the depth of the treated layer, and the 3D interconnected structures inside the layers. The PPS/Al5052 joint performances were evaluated by ISO19095 [92].

To investigate the bonding mechanism, two distinct Al5052 surface structures named NMT-1 and NMT-2, which have different pore sizes and shapes, thicknesses of modified layers, and internal pore connectivity, were employed [78]. SEM micrographs of the Al5052 surfaces of NMT-1 and NMT-2 are presented in Fig. 56a and b, respectively. The Al surface in both treatments is characterized by tiny pores approximately 20 nm in diameter. The pores of NMT-1 are relatively smaller than those of NMT-2, and the pores of NMT-1 are irregularly shaped, while those of NMT-2 are uniformly distributed.

In Fig. 57, the PPS/Al5052 joint interface of NMT-1 is depicted through both a STEM-HAADF image (Fig. 57a) and STEM-EDX elemental maps of Al, sulfur (S), and oxygen (O) (Fig. 57b, c, and d, respectively). The surface-modified layer's depth, around 100 nm, is visible in the HAADF image. The elemental maps indicate that the surface-modified layer comprises aluminum and oxygen and that the S map (Fig. 57c) signifies the penetration of PPS into the Al surface pores. In contrast, Fig. 58 shows that NMT-2 has a roughly 500 nm thick interfacial layer. The STEM bright field (BF) image shows that PPS has only penetrated the upper part of the layer, with a depth of around 100 nm, and the majority of the layer is comprised of empty holes.

By using STEM tomography, we can better understand the porous structures formed on the surface of Al. The 3D reconstructed images of NMT1 and NMT2 are displayed in a video in Fig. 59. These images reveal that the pores on NMT1 are interconnected and create 3D continuous hollows with a space of 10–20 nm (Fig. 59a). In contrast, NMT-2 exhibits isolated pores growing perpendicular to the substrate (Fig. 59b). In NMT-1, the complex narrow and deep hollows allow polymer chains to enter during the injection molding process within minutes. The continuous

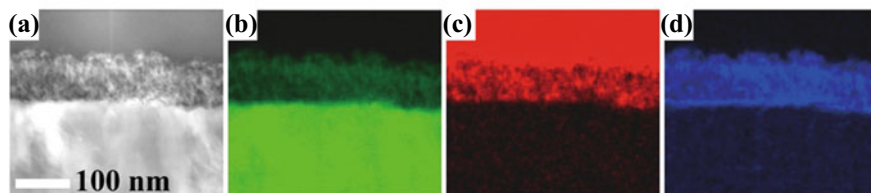


Fig. 57 Cross-sectional views of a PPS/Al5052 joint interfacial region with NMT-1 surface treatment: **a** STEM-HAADF image; **b, c, d** EDX elemental maps of Al, S, and O, respectively. Reprinted with permission from [78]. Copyright 2020, EDP Sciences. All Rights Reserved

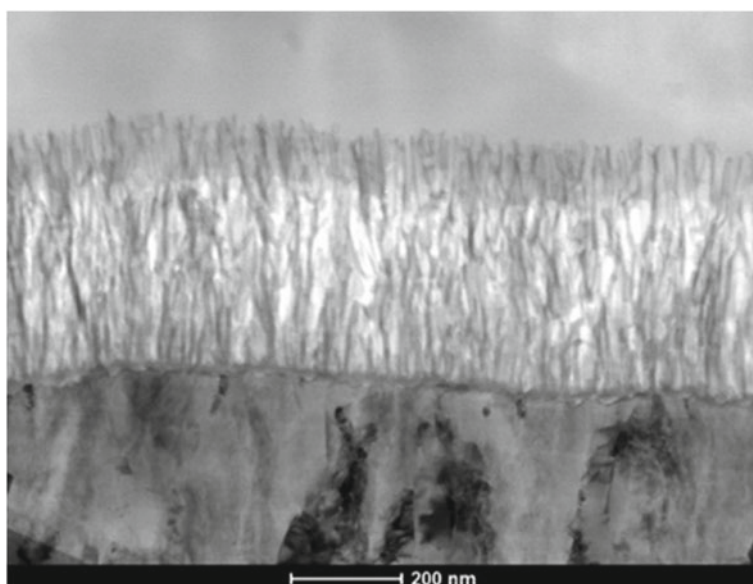


Fig. 58 STEM-BF micrograph showing PPS/Al5052 joint interface with NMT-2 surface treatment

porous structure enables air to escape from the pores, facilitating the replacement of the air with polymer chains. Conversely, NMT-2 has a narrow one-way space, and PPS polymer chains cannot displace the air from the pores. As a result, the penetration of polymer chains is limited to the upper portion of the layer.

XPS depth profiles are measured to examine the chemical interactions between metal and polymer. Figure 60a displays the XPS depth profiles, including the Al 2p peaks acquired from the NMT-1 surface before bonding. Within the first minute, the peak shifted towards higher binding energy, and another peak emerged. Ultimately, after 11 min of sputtering, only the single peak assigned to metallic Al (73 eV) remained. The depth profiles mean that the chemical state of the oxygen-containing modified layer varies from the outermost surface to the interior of the Al plate, suggesting that the surface layer possesses a chemical gradient structure and a porous

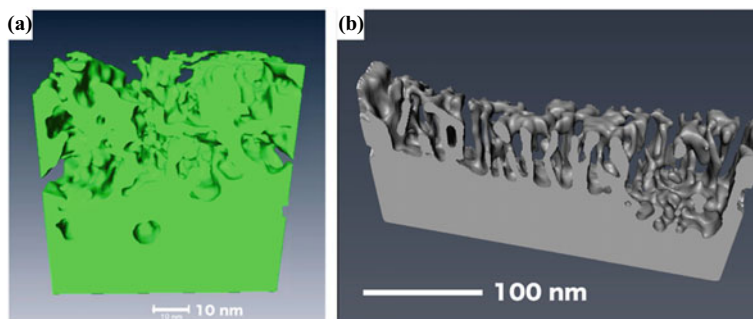


Fig. 59 A video presenting the 3D reconstructed views of NMT-1 (a) and NMT-2 (b) showing the internal porous structures created on the Al surface. Reprinted with permission from [78]. Copyright 2020, EDP Sciences. All Rights Reserved

structure. Figure 60b shows the XPS depth profiles of the PPS/Al5052 joint interface after rinsing the Al part by HCl etching. Despite the etching, a trace of Al persists on the PPS, and the Al 2p peaks are detectable during the sputtering. The binding energies at which the Al 2p peaks appear are relatively constant, independent of the sputtering time, which differs from the profiles acquired before bonding. These observations suggest that bonding PPS to Al induces changes in the chemical state of the oxygen-containing Al surface layer.

Figure 61 is the plots of the O/Al atomic ratios as a function of sputtering time, calculated by integrating Al 2p and O 1s peaks from depth profiles. The results indicate that the oxygen content is higher in the entire depth of the modified layer before bonding. In particular, the outermost surface of the modified Al before bonding has the highest O/Al ratio, which is almost equivalent to the atomic ratio of $\text{Al}(\text{OH})_3$, and gradually decreases to approximately 2.0. Therefore, the chemical shift of the Al 2p peaks observed before bonding (Fig. 60a) is caused by gradual changes in the chemical structure from the surface to the inner part.

It was known that the dehydration reactions of $\text{Al}(\text{OH})_3$ to $\text{AlO}(\text{OH})$ and $\text{AlO}(\text{OH})$ to Al_2O_3 occur when exposed to high temperatures above 253 °C and 500 °C, respectively. These endothermic reactions have 15.70 and 0.20 kJ/mole activation energies, respectively. Upon contact with the hot molten polymer, these dehydration reactions occur and absorb heat from the polymer. This heat transfer can promote the spontaneous penetration of polymer chains into the pores. Since the space provided by the pores is only slightly larger than the size of a polymer molecule, it may be challenging for highly viscous polymer melt to penetrate these tiny pores, even with high pressure applied during injection molding. The 3D continuous hollow structure likely plays a critical role in forming the metal/polymer hybrid interface, allowing the metal pores to be filled with polymer. At the same time, the air escapes from the pores during the penetration of polymer chains.

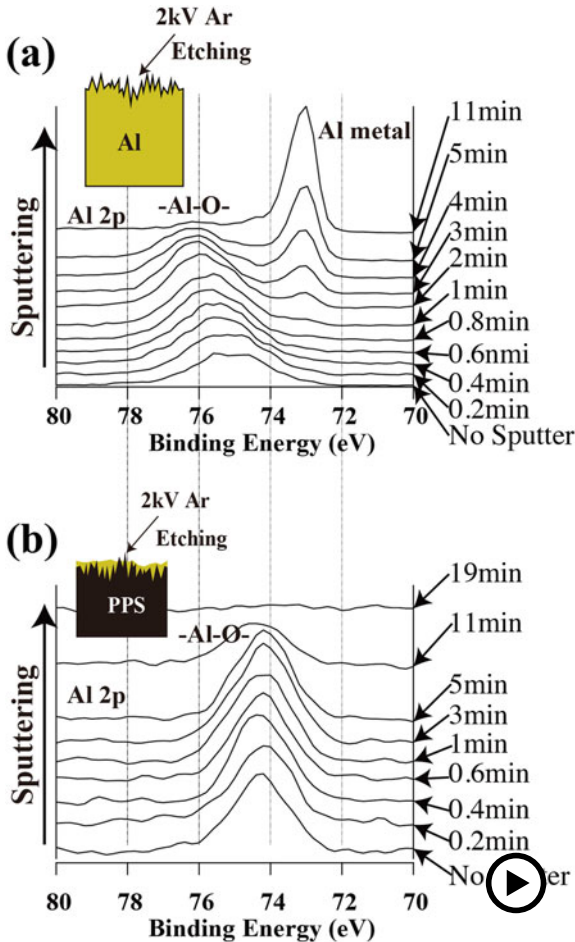
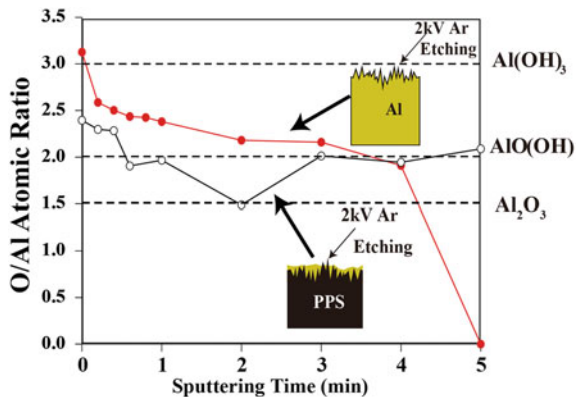


Fig. 60 XPS depth profiles of Al 2p signals of the Al surface before the bonding (a) and the Al/PPS interface after removing Al by HCl etching (b). Reprinted with permission from [78]. Copyright 2020, EDP Sciences. All Rights Reserved (▶ <https://doi.org/10.1007/000-ayj>)

Figure 62 depicts the durability of the PPS/Al5052 joint with the NMT-1 under a high humidity condition (85 °C 85%RH) and after repeated temperature cycles of a rapid-rate change. The butt-joint specimens before and after the measurement of the joint strength are also presented in Fig. 62a. The specimens are fractured near the metal/plastic joint interface, and the initial tensile strength of about 45 MPa is maintained for 3000 h. The measured strengths represent the interfacial region’s strengths because the value is significantly lower than the tensile strength of the PPS (about 120 MPa). Figure 62b presents the thermal shock resistance under two conditions. The joint strengths are maintained even after 1500 cycles of the rapid-rate temperature changes between -40 and 85 °C. It decreases to about 25 MPa with

Fig. 61 Sputtering time dependence of the atomic ratios of O/Al determined by the ratios of the integral peak intensities of Al 2p and O 1 s before bonding (Al surface) and after bonding (PPS/Al5052 interface). Reprinted with permission from [78]. Copyright 2020, EDP Sciences. All Rights Reserved



significant large scatterings of the results between 500 and 1000 cycles in the more significant temperature gap from -40 to 120 °C. The peel resistance measurement gives a typical force-distance curve, as shown in Fig. 63a, demonstrating steady peeling keeping the force of about 180 N/25 mm. The geometry of the lap joint specimen and the specimen before and after the measurement are shown in Fig. 63b, which is measured to be 44.2 ± 1.2 MPa. The failure occurred near the interface, where a small amount of PPS is partly fixed on the Al plate. In all the measurements, a small amount of PPS remains on the fracture surface of Al, implying that PPS forms a weak boundary layer near the interface during the joint process. The difference in the cooling rate of PPS in the interfacial region close to the metal and in the bulk part causes the joint strength reduction. The PPS undergoes rapid cooling when injected on the Al plate at 120 °C after melting at 290 – 330 °C in the injection molding machine. This results in different crystallization behavior near the interface than the bulk part. It can be inferred that the crystallinity of PPS near the interface is lower than that of the bulk part due to this rapid cooling. The excellent joint performance of the PPS/Al5052 joint is demonstrated under various test conditions, except for the thermal shock with a significant temperature gap, which can be attributed to the large difference in the thermal expansion coefficient between the metal and plastic.

To comprehend the failure mechanism of the joint, in situ STEM is performed to observe the failure behavior directly [93]. As discussed in Chap. 2, this technique involves subjecting thin sections that include the joint interfaces to tensile load using a specially designed specimen holder for the in situ tensile experiments under STEM. Figure 64 is a video demonstrating the failure behavior of the PPS/Al direct joint in STEM bright-field (BF) mode, while Fig. 65 presents selected images captured from the movie. In Fig. 65a and d, dark strands appear due to wrinkles produced during specimen preparation by ultramicrotomy. Rubber domains dispersed in the PPS matrix to improve injection moldability and impact strength of molded articles can also be observed. Upon applying a tensile load to pull the specimen perpendicular to the interface, the PPS part stretched and the wrinkles disappeared. Microcavities were observed to form preferentially inside the rubber domains (Fig. 65b and e), and

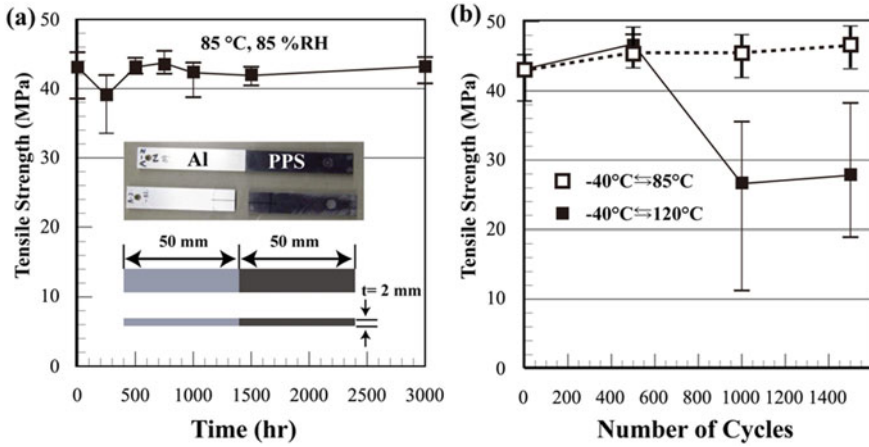


Fig. 62 The PPS/Al5052 tensile joint strength as a function of residence time under accelerated environmental conditions: **a** durability at 85 °C and 85%RH and the butt-joint test specimen before and after the test; **b** thermal shock resistivity under the temperature jumps from -40 to 85 °C and from -40 to 120 °C as a function of the cycles. Reprinted with permission from [78]. Copyright 2020, EDP Sciences. All Rights Reserved

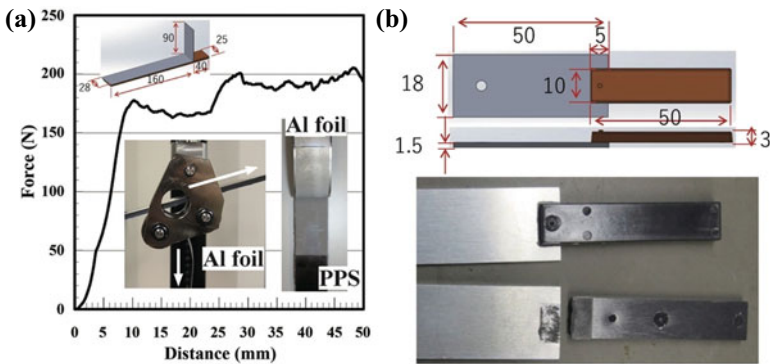


Fig. 63 Force vs. distance curve obtained in the peeling resistivity test of Al/PPS laminate with NMT1 surface treatment, the specimen geometry, a floating roller jig, and the specimen after the test (a). The specimen geometry of the PPS/Al5052 lap joint and the test specimens before and after the test (b). Reprinted with permission from [78]. Copyright 2020, EDP Sciences. All Rights Reserved

microcracks in the PPS matrix connecting neighboring domains were produced. The failure’s final stage before the specimen’s complete fracture is shown in Fig. 65c and f, revealing that the elastomer domains near the interface underwent significant deformation and then ruptured. Finally, the PPS part is separated from the Al part.

The interpretation of failure behavior observed by the in situ TEM tensile experiment is described as shown in Fig. 66. When tensile stress is applied to the joint

Fig. 64 Video showing the failure behavior of the PPS/Al direct joint in STEM bright-field (BF) mode



specimen, the plastic part preferentially elongates along the tensile direction, and microcavities are generated inside the rubber domains (Fig. 66a). As a result, the plastic deformation of the PPS matrix around the rubber domains is promoted, and crazes are generated between the rubber domains (Fig. 66b). At the same time, the plastic experiences a compressive stress perpendicular to the tensile direction. In the region close to the interface, the deformation of the plastic part is constrained by the strong bonding with Al (Fig. 66c). Therefore, the stress concentrates in the interfacial area in the plastic, causing the specimen to rupture (Fig. 66d).

The interfacial fracture energies of PPS/Al5052 joints can be characterized using a test specimen designed based on the compact tensile (CT) test specimen geometry described in ISO 13586 [94] for measuring the fracture toughness of bulk plastics. The joint laminate is produced by bonding metal and plastic plates, each with a thickness of 2 ± 0.1 mm, together, leaving a non-bonded region on one side to serve as a pre-crack as shown in Fig. 67a. To apply stress to the pre-crack tip, the laminate is sandwiched between two aluminum blocks using an epoxy adhesive, as shown in Fig. 67b. The surface of the metal substrate was masked to reduce the bond area of the laminate by 50%, ensuring that failure initiates from the pre-crack rather than the interface between the load block and the metal/plastic laminate. The pins inserted into the two holes of the load blocks were used to apply a crack opening stress to the specimen at a testing speed of 10 mm/min.

A force–displacement curve for a PPS/Al5052 laminate treated with the NMT1 is shown in Fig. 68. This curve displays an abrupt linear increase in force with a drop at the moment of crack initiation. The energy required to fracture the specimen is

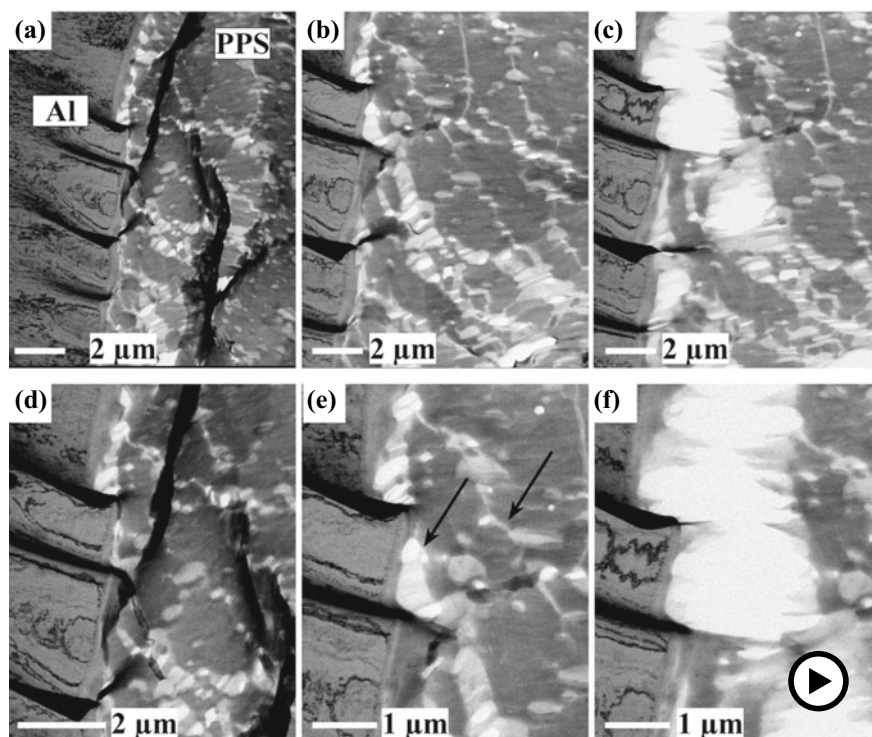


Fig. 65 In situ STEM-BF images of the PPS/Al direct joint interface under tensile load showing the failure of the interface: **a** initial state before applying the tensile load; **b** evolution of cavity and craze before the failure; **c** crack generated in the interfacial region. **(d)**, **(e)**, and **(f)** are the high-magnification images of **(a)**, **(b)**, and **(c)**, respectively. The arrows indicate the microcavity in the elastomer domains and the crazes between neighboring domains. Reprinted with permission from [93] (► <https://doi.org/10.1007/000-ayp>). Copyright 2021, Elsevier. All Rights Reserved

determined by calculating the area under the linear portion of the force–displacement curve.

The findings of this study are summarized in Table 1. The data demonstrate that the NMT-1 surface treatment yields slightly higher values than the NMT-2 under all test conditions. Although the penetration of PPS into the surface pores in NMT-2 is incomplete, it shows high joint strength. Additionally, it shows that direct Al/PPS bonding produces significantly higher joint strength than adhesive bonding.

The failure mechanism of the joints is investigated with the cross section of the fracture surfaces. Figure 69a shows a largely deformed PPS attached to the Al surface with the NMT-2 surface treatment in the upper part of the image. A mixed elemental map of S, O, and Al shown in Fig. 69b reveals that PPS is not pulled off from the Al surface pores. In Fig. 70a and b, STEM-HAADF and EDX mixed elemental maps of the fracture surface near the crack tip of the Al with the NMT-1 treatment are displayed, respectively. These images indicate the largely deformed PPS

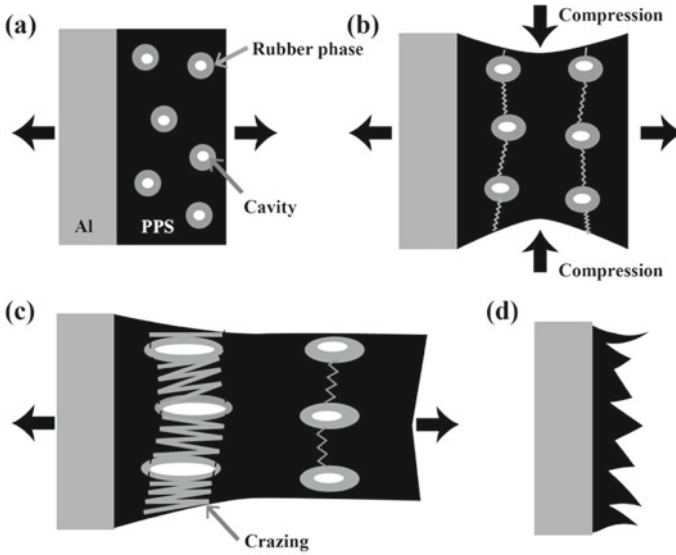


Fig. 66 Schematic illustration presenting the failure behavior of the PPS/Al direct joint interface

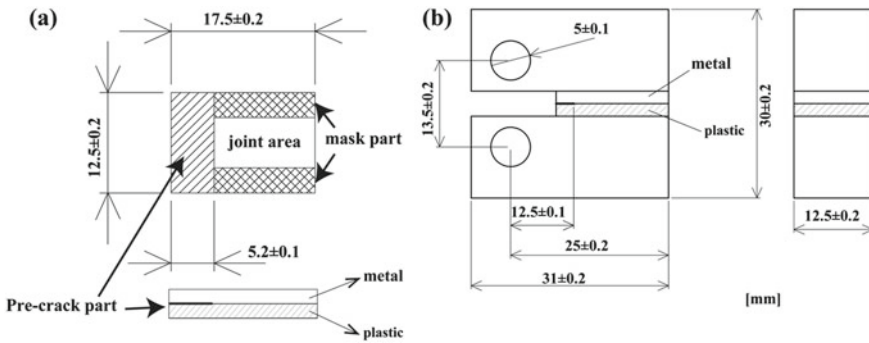


Fig. 67 Test specimen geometry and size for measuring interfacial fracture energy: **a** metal/plastic laminate; **b** the test specimen for the fracture test. Reprinted with permission from [78]. Copyright 2020, EDP Sciences. All Rights Reserved

attaches to the Al surface. Figure 70c is a magnified view of the interfacial region of Fig. 70a, which reveals that the surface-modified layer is partially damaged with voids produced inside the surface layer. The S elemental map (Fig. 70d) indicates that PPS remains inside the pores even though the layer is damaged. Based on these findings, it is concluded that once PPS diffuses into the pores, it cannot be pulled off from the pores in the surface layer, and instead, the interfacial layer is damaged to create voids. This failure behavior explains why the joint strength of NMT-1 is higher than that of NMT-2.

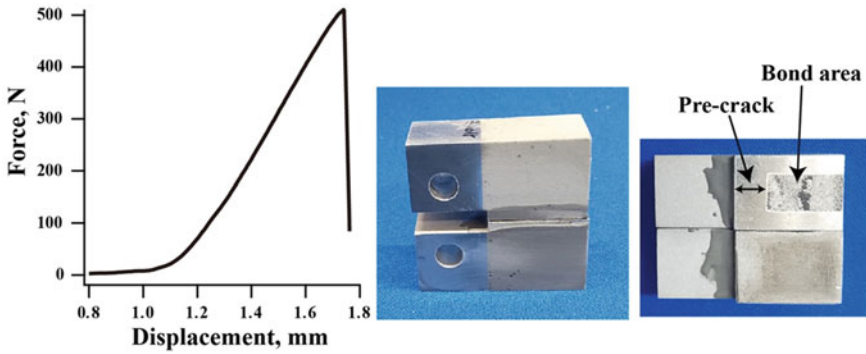


Fig. 68 The typical force–displacement curve obtained with a PPS/Al5052 laminate with NMT1 surface treatment and fracture surfaces of the test specimen

Table 1 Summary of the joint properties of the PPS/Al5052 joints with the NMT-1 and NMT-2 surface treatment

Surface treatment	NMT1 (Direct bonding)	NMT2 (Direct bonding)	NMT1 (Adhesive bonding)
Fracture energy (J/m)	12.3 ± 1.0	11.6 ± 1.1	3.20 ± 0.08
Lap shear strength (MPa)	44.2 ± 1.2	42.3 ± 0.52	10.8 ± 0.22
Tensile strength	43.0 ± 2.5	41.2 ± 2.2	18.5 ± 1.2

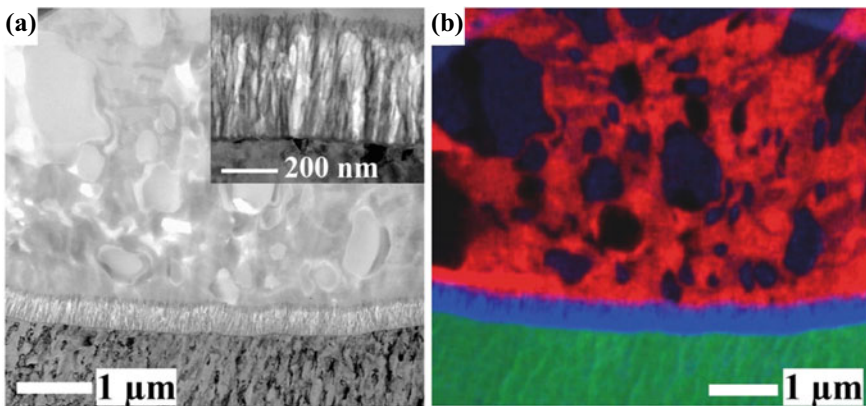


Fig. 69 STEM-HAADF and STEM-EDX elemental maps of the cross sections of the fracture surface of the Al with NMT-2 treatment after the fracture energy measurement: **a** STEM-BF cross-sectional image; **b** STEM-EDX mixed map of S (red), O (blue), and Al (green). Inset in **(a)** is a magnified image of the interfacial region. Reprinted with permission from [78]. Copyright 2020, EDP Sciences. All Rights Reserved

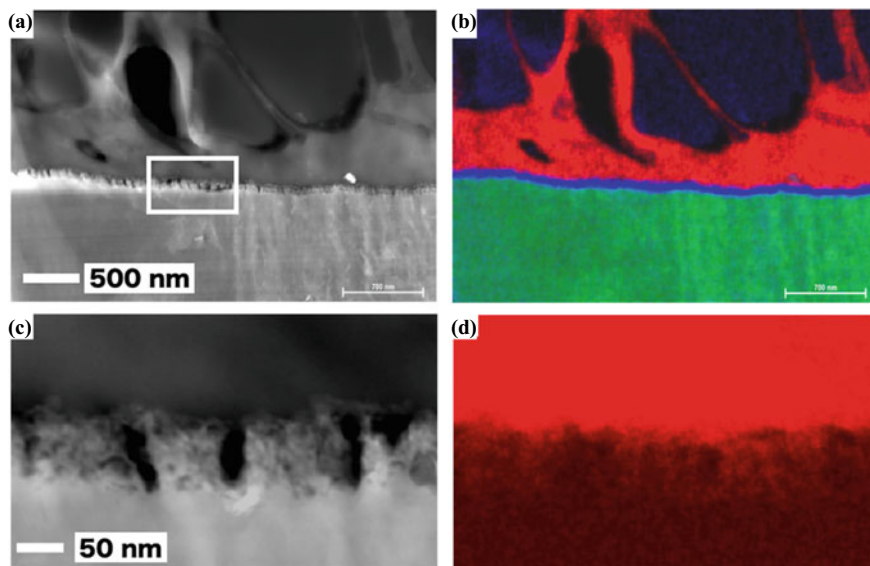


Fig. 70 STEM-HAADF and STEM-EDX elemental maps of the cross sections of the fracture surface of the Al with NMT-1 treatment after the fracture energy measurement: **a** STEM-HAADF image; **b** STEM-EDX mixed map of S (red), O (blue), and Al (green); **c** magnified image of **a**; **d** magnified image of the STEM-EDX S map representing the PPS distribution. Reprinted with permission from [78]. Copyright 2020, EDP Sciences. All Rights Reserved

Direct bonding of plastic and Al via insert injection molding provides high joint strength. This high joint performance can be achieved by the surface pretreatment of Al substrate, creating porous surface structures of 30–50 nm. The small pores are filled with molten polymers in the injection molding process in a short time. This study investigates the bonding mechanism between Al and PPS with two different surface treatments with different 3D connectivity in the modified surface layer. STEM tomography allows us to observe the interconnectivity of the pores at the joint interfaces. NMT-1 has three-dimensionally co-connected pores, while NMT-2 has isolated two-dimensional pores perpendicular to the metal substrate. It was found that the 3D-connected porous structure in NMT-1 facilitates polymer chain penetration. Due to dehydration, we observed a chemical reaction during the bonding process that converts meta-stable aluminum hydroxide into more stable alumina. The 3D porous structure and dehydration process are essential in creating a polymer/metal strong joint. Although incomplete penetration of PPS into the pores, sufficient joint strength can be achieved. These findings suggest that the nano-sized porous metal structures yield robust adhesion of polymer chains with metal.

8 Toughness and Durability of Interfaces in Dissimilar Adhesive Joints of Aluminum and Carbon-Fiber Reinforced Thermoplastics

Thermosetting polymers like epoxy and polyester resins have been widely studied as matrices for carbon fiber-reinforced plastics (CFRP) [95, 96]. However, these composites are not recyclable due to the characteristics of thermosetting polymers. In contrast, thermoplastic polymers have gained significant attention as a matrix because of no heat curing process needed, less hazardous chemical compositions, better recyclability, and mass production capabilities. By combining thermoplastic polymers with unidirectional and discontinuous carbon fibers, composite materials can be produced. Carbon fiber-reinforced thermoplastic polymers (CFRTP) offer a weight reduction of approximately 50% compared to steel and 20% to aluminum [97, 98].

CFRTPs have been identified as a promising composite for various industrial applications, including in the automotive, renewable energy, and aerospace industries. Their exceptional properties, such as high strength-to-weight ratio, wear resistance, and stiffness, give them an edge over traditional materials like metals. CFRTPs are better suited for mass production in the automotive industry. They can be easily manufactured using conventional molding methods like injection, rotational, extrusion, vacuum, and compression molding. Unlike traditional CFRP, the molding process for CFRTP is shorter, requiring only a few simple steps. Moreover, the shape of CFRTP can be altered after molding, enabling recycling through reuse, reforming, or other means, thereby improving production efficiency.

As a result, the demand for reliable techniques for joining metals and CFRTP is increasing. Adhesive bonding is a preferred option due to its lower weight, cost-effectiveness [99, 100], ability to prevent electrolytic corrosion [101, 102], and uniform stress distribution over the entire bonding area, as opposed to mechanical joining techniques such as welding, riveting, and bolt fastening. However, great concerns arise regarding the durability and mechanical resistance of adhesive bonding under severe service conditions, as adhesives are believed to be weak against heat than mechanical joining. Therefore, establishing a methodology to ensure the reliability of adhesive bonding is crucial.

A thorough evaluation of adhesive interfaces is required to guarantee the safety of adhesive bonding. The dissimilar adhesive joints of metal and CFRTP involve two interfaces, one between the adhesive and CFRTP, and the other between the adhesive and metal [103, 104]. The failure of joints can occur at any of the interfaces, within the adhesive layer, or a combination of all three. Accurately characterizing the interfacial region in adhesive joints is essential for appropriate system design by selecting surface pretreatments for adherents and adhesives.

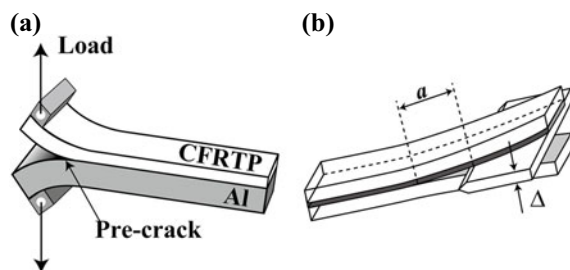
Accurate interfacial characteristics cannot be extracted from the measured data by traditional engineering tests such as lap shear and peel adhesion tests because these tests are sensitive to inelastic deformations in adherend and adhesive away from the interface. The double cantilever beam (DCB) geometry is suitable for estimating

the fracture resistance of adhesive interfaces subjected to tensile opening force as the crack grows along the interface [105, 106]. This study aims to investigate the fracture toughness and durability of different adhesive interfaces in joints of Al and CFRTP with a polyamide-6 (PA6) matrix under high humidity and temperature conditions, using an optimized DCB specimen geometry, as shown in Fig. 71 [85]. By continuously pulling the specimen apart at a constant velocity (Fig. 71a) or displacement by inserting a wedge (Fig. 71b), the locus of failure is inspected, and the bonding mechanism of surface pre-treatments of CFRTP is discussed.

The TEPEX® product, manufactured by LANXESS, is a CFRTP consisting of plain woven carbon fiber continuous fabric impregnated with PA6 with a bending modulus of 50 GPa. NMT-1 was used to prepare surface-treated aluminum alloy (Al5052) plates with a bending modulus of 65 GPa, and their surface properties are described in Sect. 7. Three types of commercial paste adhesives (epoxy, acrylic, and urethane) were used to join the CFRTP and Al. The two-component epoxy adhesive (Denatite 2204, Nagase ChemteX Corp.) was cured at 25 °C for 1.5 h and 100 °C for 1 h. The second-generation acrylic (SGA) adhesive (HARDLOC C-335–20, Denka corp.) was cured at room temperature for 1 h and then at 80 °C for 1 h. The two-component urethane adhesive was cured at 25 °C for 1.5 h and 80 °C for 1 h.

Two methods are used to pretreat the CFRTP surface: acetic acid treatment, where the substrate is rubbed with cotton containing acetic acid, and flame treatment, which is detailed in Sect. 4. To control the thickness of the adhesive layer, 200 μm diameter glass spheres are added after coating the adhesive onto both adherents. Before lamination, an 80 μm thick PTFE film is placed on one end of the substrate, which creates a 50 mm long non-bonded area. This area is used as a pre-crack for the initiation of the crack in the DCB test. After curing, rectangular coupons with a length of 250 mm and a width of 25 mm are cut out from the bonded laminates. These specimens include a non-bonded part at one end.

Fig. 71 Schematic illustrations of the specimens for ADCB test (a) and wedge test (b). Reprinted with permission from [85]. Copyright 2020 American Chemical Society, All Rights Reserved



8.1 Evaluation of Interfacial Fracture Toughness by ADCB Test

To assess the toughness of dissimilar joint interfaces, a universal testing machine is utilized to apply a tensile opening load to a pre-crack of the specimen, as shown in Fig. 71a. An asymmetric double cantilever beam (ADCB) test [107] is employed using specimens of 10 mm thick Al and 4 mm thick CFRTP beams to obtain reliable interfacial toughness values. The modulus mismatch of the dissimilar joint makes it necessary to achieve the reliability of the results. When using a conventional DCB specimen with beams of equal thickness for dissimilar joints, the crack could escape from the interface and calculated fracture energy is overestimated. Therefore, the appropriate Al/CFRTP thickness combination have to find by testing specimens with different thickness ratios, as presented in Fig. 72. In the DCB test with the same Al/CFRTP thicknesses beams, the crack propagation accompanies significant plastic deformation of the Al beam, which makes it difficult to interpret the calculated data. Increasing the Al/CFRTP thickness ratio decreases the plastic deformation of the Al beam, and a ratio of 5/2 mm shows negligible plastic deformation, enabling the test to be performed within the elastic deformation of both beams. The thermal expansion coefficient mismatch between Al and CFRTP is another concern that causes specimen warping. When cooled from a cure temperature to room temperature, residual thermal stress in the specimen impacts the calculation of fracture energies. The specimens with 10 mm thick Al and 4 mm thick CFRTP make specimen warping negligible.

One-component epoxy (Scotch-Weld, EW-2040, 3 M, USA) is used to adhesively bond the load blocks to one end of the specimens following ISO 25217 [108], and they are set to the testing instrument via loading blocks. All tests are performed at room temperature with a constant crosshead speed of 1 mm/min. The mechanoluminescence (ML) technique is introduced to monitor the crack's progress during the ADCB test [109], which detail is described in Chap. 4. The force measured by a universal testing machine and the crack length measured by the assistance of ML are plotted against the crack opening displacement (COD), measured by the displacement of the crosshead. The interfacial fracture toughness is calculated by using a method described later.

Detecting the crack tip accurately is essential to obtain precise fracture toughness values by the ADCB test. The conventional method to detect the crack tip is to apply white paint to the side of the specimen, as described in ISO 25217. However, the crack tip may not always be detectable. In contrast, the ML technique effectively identifies the crack tip precisely. The ML particles act as a sensitive mechanical sensor that emitted bright light under mechanical stimuli, revealing the specimen's dynamical strain/stress distribution as demonstrated in Fig. 73a. The ML-assisted DCB test allows us to observe the crack frontline within the adhesive layer from outside the adherend.

Figure 73b–d display the load and crack length versus COD for the non-treated, acetic acid-treated, and flame-treated specimens. The tensile load initially increases linearly but deviates from this slope before reaching the maximum load point. The



Fig. 72 Al/CFRTP thickness ratio dependence on the plastic deformation of the Al beams after the DCB test of the Al/CFRTP adhesive joints. The total thickness is fixed at 7 mm and the thickness ratio is varied. Reprinted with permission from [85]. Copyright 2020, American Chemical Society. All Rights Reserved

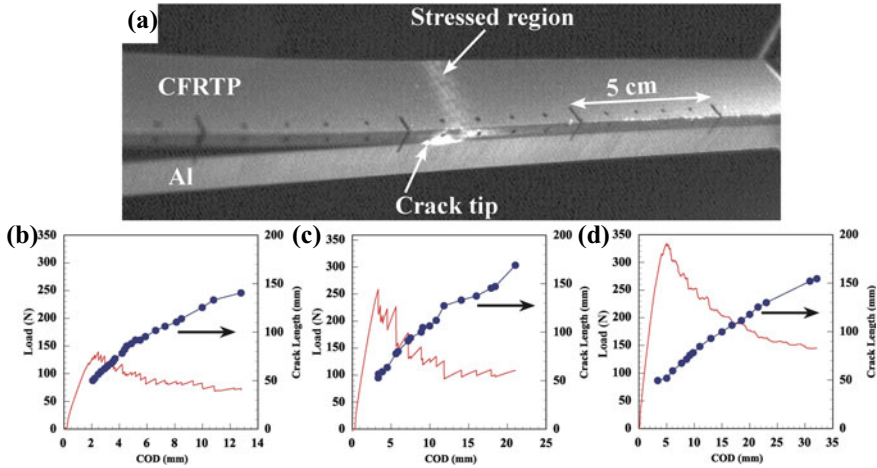


Fig. 73 ML emission seen in a test specimen for the ADCB test of the dissimilar adhesive joints of CFRTP and Al (a). The load and crack length versus COD plots obtained for the non-treated (b), acetic acid-treated (c), and flame-treated (d) specimens through the ADCB test. Reprinted with permission from [85]. Copyright 2020, American Chemical Society. All Rights Reserved

crack begins shortly before the maximum load is reached and continues to grow with a gradual decrease in load in all tests [110]. After passing the maximum load point, the load-COD curves for the non-treated (Fig. 73b) and acetic acid-treated (Fig. 73c) specimens exhibit similar features, showing gradual decay with small random fluctuations as the crack propagated. In contrast, the load for the flame-treated specimen (Fig. 73d) shows a smooth decay during crack propagation. Figure 74 is a video demonstrating that the cracks in the non-treated and acetic acid-treated specimens progress unstably with repeated “initiation and arrest”. In contrast, the flame-treated specimen exhibits continuous and steady crack growth. Furthermore, it can be found that the crack propagation rate is the fastest for the non-treated specimen, slower for the acetic acid-treated specimen, and slowest for the flame-treated specimen. These results indicate that both fracture toughness and fracture behavior are affected by the surface treatment of the CFRTP.

The modified beam theory is used to estimate the interfacial fracture energies of the ADCB specimens. To introduce an equivalent stiffness (EI_{eq}), the cubic root of compliance, C , as defined by Eq. (14) is plotted against the crack length, a , as shown in Fig. 75. All points on the graph are on the linear slopes produced by least squares fitting. The negative X-intercept of the linear fits provided Δ values, while the linear fit slope represented the specimen’s stiffness, defined as $(1/EI_{eq})^{1/3}$. The interfacial fracture energy, G , can be calculated using Eq. (15), with B representing the specimen width and Δ serving as the calibration parameter.

$$C = \frac{\delta}{P} \tag{14}$$

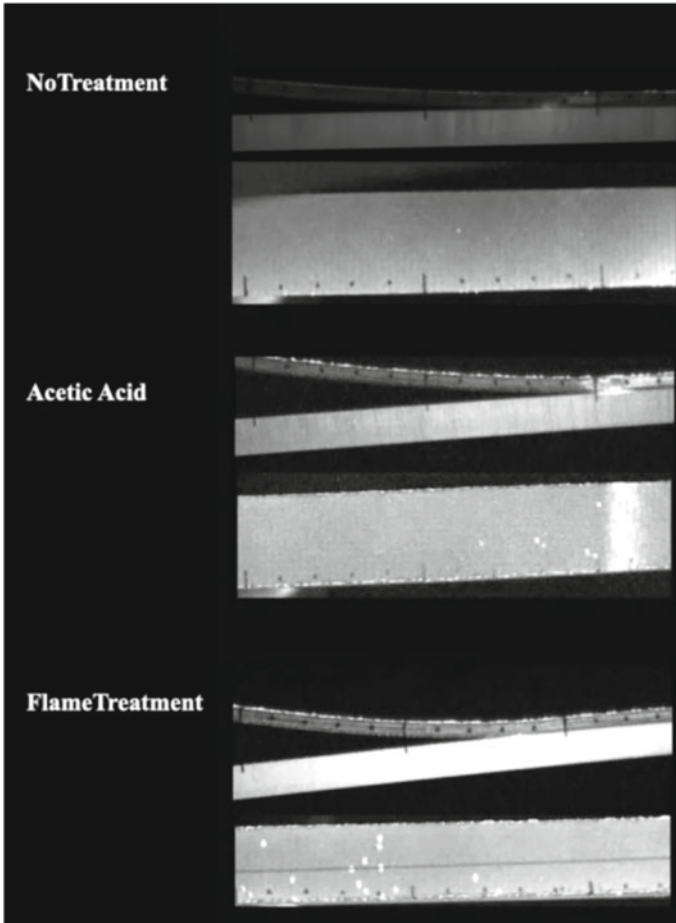
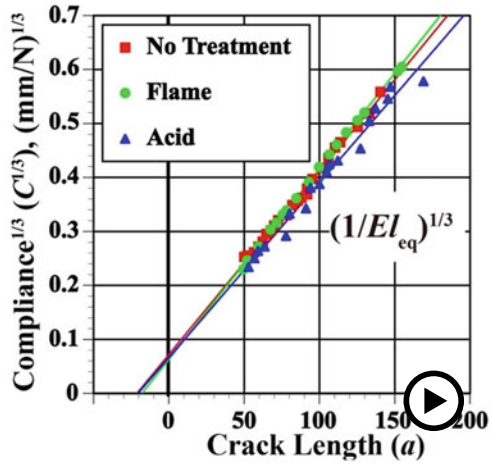


Fig. 74 A video showing the cracks progressed in ADCB tests of the non-treated, the acetic acid-treated and the flame-treated specimens. Reprinted with permission from [85]. Copyright 2020, American Chemical Society. All Rights Reserved

$$G = \frac{3P^2(a + \Delta)^2}{2B(EI)_{eq}} \quad (15)$$

The toughness of the Al/CFRTP dissimilar joint interfaces is evaluated by plotting G values against the crack length in the crack growth resistance curves (R-curve), as shown in Fig. 76. The influence of the surface pretreatments on the interface toughness is found to be adhesive-dependent. The interfacial fracture toughness of the epoxy adhesive joint is significantly enhanced by flame treatment. In contrast, the acetic acid treatment improved the joint toughness to some extent but showed

Fig. 75 Plots of $C^{1/3}$ versus crack length, a , for determining the equivalent stiffness, EI_{eq} , and the calibration parameter, Δ . Reprinted with permission from [85]. Copyright 2020, American Chemical Society. All Rights Reserved
 (▶ <https://doi.org/10.1007/000-ayq>)



fluctuations in the values during crack propagation. The lowest G values in the R-curves of the flame-treated and non-treated specimens are attributed to the energy required for crack initiation. The slight increase in G values with increasing crack length suggests the growth of a plastic zone around the crack tip, which makes the interfaces more ductile. Surface treatments are necessary for bonding with the SGA, and the acid treatment is the most effective, followed by the flame treatment. On the other hand, high bonding performance is observed for the urethane adhesive joint, regardless of surface treatment.

To investigate the mechanism of the surface pretreatments for CFRP, the interfaces between pristine PA6 and the epoxy adhesive were investigated. As stated in Sect. 4, the flame treatment produces a 10 nm thick amorphous layer on the PA6 surface. The absorption band at 1710 cm^{-1} observed in FT-IR spectra of acetic acid-treated PA6 is attributed to the $\text{C}=\text{O}$ stretch of acetic acid [111], indicating

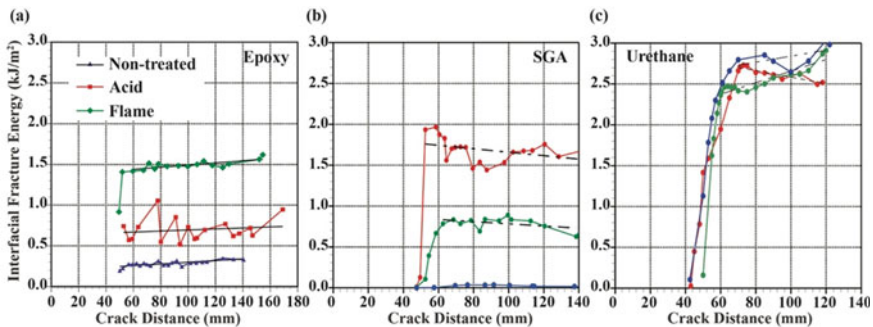


Fig. 76 Crack growth resistance curves of no treated (blue), acetic acid treated (red), and flame treated (green) specimens: **a** epoxy adhesive; **b** SGA; **c** urethane adhesive. Reprinted with permission from [85]. Copyright 2020, American Chemical Society. All Rights Reserved

the absorption of acetic acid into PA6 [112]. STEM-EDX results demonstrated that acetic acid treatment suppresses the segregation of silica, which is contained in the epoxy adhesive, on the interface, thereby promoting contact between the adhesive and PA6 and enhancing adhesion. The authors suggest that the acetic acid treatment may improve the affinity of PA6 to the epoxy adhesive, as evidenced by contact angle measurements that showed enhanced wettability of the PA6 surface. The flame treatment did not produce specific functional groups on PA6; the amorphous layer may improve surface mobility at the curing temperature, allowing for diffusion of the liquid state adhesive into the PA6 layer and entanglement with PA6. Although the mechanism for SGA and urethane adhesives is unknown, the authors recommend using the ADCB test with appropriate beam thickness combinations to quantitatively evaluate the effects of adhesive and surface treatment on dissimilar adhesive joints.

8.2 Evaluation of Durability of Adhesive Interfaces Under High Humidity Environment by Wedge Test

In the wedge test, the interface is cleaved by pulling apart the edge of the specimen at a constant displacement, as illustrated in Fig. 71b. It is a simple test that requires no specialized equipment, making it suitable for use in different environmental conditions where a testing machine is difficult to be used. After the wedge is inserted into the interface, a crack is initiated and stabilized. If the environmental conditions change, the crack may expand afterward, which allows for assessing interface durability under specified environmental conditions. An equation that is discussed in Sect. 3 can be used to relate the fracture energy directly to the crack length.

Figure 77a displays a side view of an Al/CFRTP wedge test specimen, where Al and non-treated CFRTP are bonded with the epoxy adhesive. When the Al wedge is inserted into the pre-crack, the crack is extended and then terminated within a 12-h. The specimen is subjected to a high temperature and high humidity environment of 85 °C and 85%RH. Water penetrates the interfaces when the adhesive layer is exposed to these conditions under the stress applied by the wedge. Water invades the adhesive layer at the crack tip, resulting in further crack extension along the interface. As illustrated in Fig. 77b, this significantly decreases interfacial fracture toughness within the first few hours. The decrease in interfacial toughness is primarily attributed to the high humidity, which appeared independent of the surface pretreatment condition. Subsequent exposure to these conditions resulted in a gradual decline in toughness values, G_{wet} . A test is also conducted under dry conditions at 85 °C, which indicates that heat damage to the interfacial region is negligible and the decrease in interfacial toughness is primarily caused by high humidity.

Figure 77c through 77e depict the visual examination of fracture surfaces following the wedge tests of non-treated, acetic acid-treated, and flame-treated specimens. The non-treated specimen (Fig. 77c) exhibits an apparent fracture between the adhesive and the CFRTP interface. In the acetic acid-treated specimen (Fig. 77d),

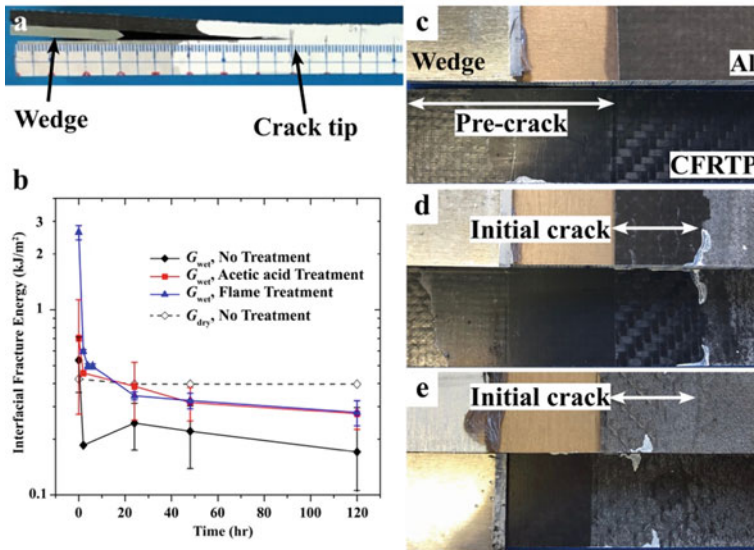


Fig. 77 Wedge-test of Al/CFRTP adhesive joints with the epoxy adhesive: **a** side view of the specimen after the wedge insertion; **b** semi-log plot of interfacial fracture energy under wet, G_{wet} , and dry, G_{dry} , conditions as a function of residence time in high humidity condition at 85 °C and 85% RH; **c** fracture surfaces of the non-treated specimen; **d** acetic acid-treated specimen; **e** flame-treated specimen. Reprinted with permission from [85]. Copyright 2020, American Chemical Society. All Rights Reserved

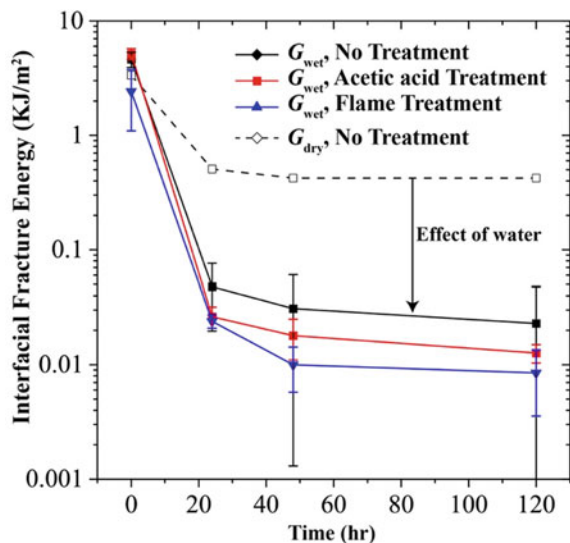
the locus of failure shifts from the interfacial to the cohesive at the period when the crack extension starts in the high humidity environment, indicating successful toughening of the CFRTP/adhesive interface and preventing water invasion into the interface. In contrast, water is absorbed into the epoxy adhesive, not into the interface, causing degradation of the adhesive and significantly reducing the interfacial toughness. Therefore, the interfacial fracture toughness of the acetic-acid-treated and flame-treated specimens under wet conditions, G_{wet} , are nearly identical, while the non-treated specimen exhibited much lower values. The flame-treated specimen did not fail at the CFRTP/adhesive interface (Fig. 77e), indicating the critical role of physical bonding created via entanglements in interface toughness.

The adhesive joints with the urethane adhesive are also evaluated under the same condition. The urethane adhesive exhibits the initial high bonding performance regardless of the CFRTP surface pretreatment, as shown in Fig. 76c. However, the crack extends along the interface once the specimen is brought into the high-humidity environment. This means the urethane adhesive is much weaker than the epoxy under high humidity conditions, although the initial adhesion strength is remarkably high. According to Fig. 78, the initial interfacial toughness values are higher than the epoxy adhesive, but the interfacial fracture toughness decreased significantly within the first 24 h. The interfacial toughness was also measured in a dry condition at 85 °C. Although it reduces, the reduction is not as significant as in the wet condition

and differed from the behavior of the epoxy adhesive. This difference highlights the impact of water on the interfacial toughness with the urethane adhesive. The results indicate that the urethane adhesive exhibits weaker performance in wet conditions when compared to the epoxy adhesive. Furthermore, the surface treatments exhibit negative effect on the durability. Unlike the epoxy adhesive, the surface pretreatments of CFRTP shows no chance to improve the durability under the high-humidity condition for the urethane adhesive.

To gain further insight, a detailed investigation was conducted using STEM with thin cross sections of the fracture surfaces of the Al sides. Figure 79a, b, and c exhibit STEM-HAADF images of the non-treated, acetic-acid-treated, and flame-treated specimens, respectively. Significant changes are observed in the Al surface structures of the non-treated specimens (Fig. 79a) and the acetic acid-treated (Fig. 79b). In contrast, the original porous structure on the Al plate is preserved in the flame-treated specimen (Fig. 79c). In the non-treated specimen, the Al surface oxide layer is highly elongated along the crack opening direction, with a 300–400 nm length, confirmed in the corresponding EDX elemental maps (Fig. 79d). The acetic acid-treated surface appears to have been significantly damaged, with voids generated within the layer, which seems to be partially separated from the Al metal part (Fig. 79e). The wedge test conducted under high humidity conditions reveals that water preferred to invade the Al/adhesive interfaces in the non-treated and acetic acid-treated specimens, resulting in the growth of thick oxide layers. Although the urethane adhesive used in the study exhibited high initial adhesive strength and did not require surface treatment, its strength considerably decreased when exposed to high humidity. Previous experiments have shown that isocyanate can chemically bond with glycidyl groups on solid substrates [113], implying the possibility of chemical bonding between isocyanate

Fig. 78 The semi-log plot of interfacial fracture energy of the urethane adhesive under wet, G_{wet} , and dry, G_{dry} , conditions as a function of residence time in the high humidity condition at 85 °C and 85 RH%. Reprinted with permission from [85]. Copyright 2020, American Chemical Society. All Rights Reserved



and PA6. However, the harmful effects of flame treatment on the urethane adhesive remain unclear and require further investigation.

Two different test methods were employed to assess the toughness and durability of dissimilar adhesive joints between CFRTP and Al alloy under high humidity conditions. The first is the ADCB test, in which the specimens are pulled apart continuously at a constant velocity, while the second is the wedge test, in which they are pulled apart at a constant displacement. The ML-assisting ADCB test allows for accurate detection of the crack tip and visualization of micro-deformations around it, revealing plastic deformation and failure inside the CFRTP. Combining ADCB and wedge tests provides insight into the effects of surface pretreatments and adhesive types on adhesive interface characteristics. Various failure modes are observed, as summarized in Table 2. Notably, using epoxy adhesive with acetic acid treatment results in a switch

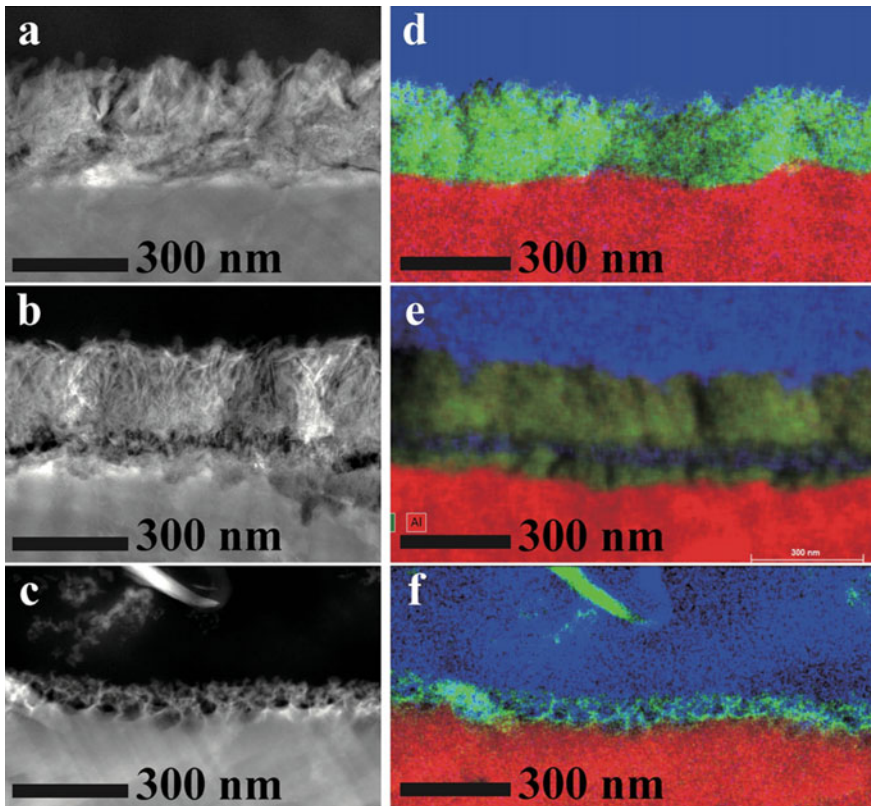






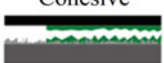







Fig. 79 STEM-HAADF (a–c) images and STEM-EDX elemental maps (d–f) of the cross sections of the Al fracture surfaces: a, d non-treated; b, e acetic acid treated; c, f flame treated specimens. Blue, green, and red represent carbon, oxygen, and aluminum distributions in the STEM-EDX maps. Reprinted with permission from [85]. Copyright 2020, American Chemical Society. All Rights Reserved

Table 2 Loci of failure in the test conditions employed in this study and schematic illustrations representing the failure mode. Reprinted with permission from [85]. Copyright 2020, American Chemical Society. All Rights Reserved

Adhesive	Surface Treatment on CFRTP	Locus of Failure	
		DCB	Wedge
Epoxy	No	Interfacial (CFRTP/Adhesive) 	Interfacial (CFRTP/Adhesive) 
	Acetic acid	Interfacial (CFRTP/Adhesive) 	Cohesive 
	Flame	Cohesive 	Cohesive 
Urethane	No	Cohesive 	Interfacial (Adhesive/Al) 
	Acetic acid	Cohesive 	Interfacial (Adhesive/Al) 
	Flame	Cohesive 	Interfacial (CFRTP/Adhesive) 

from “interfacial” to “cohesive” failure when the environment changes from atmospheric to high humidity. Under high humidity conditions, failure of the urethane adhesive occurs at the Al/adhesive interface with significant deformation of the Al surface layer. This study aims to establish a correlation between interfacial structure and mechanical joint properties, regardless of joint design or size. The results do not represent adhesive-type properties and require further data collection. The durability of adhesive joints under high humidity conditions remains a challenge, and future efforts will focus on developing appropriate surface treatments and highly durable adhesives.

8.3 Stress-Induced Corrosion at Adhesive Interfaces

As shown in Fig. 79, the cross-sectional STEM observations of aluminum fracture surfaces indicate the formation of a novel structure within the thick oxide layer, suggesting that the Al/adhesive interfaces are severely attacked by moisture. The wedge test was employed with an Al/Al similar adhesive joint with an epoxy adhesive

to find the chemical phenomena at the Al adhesive interface. The wedge inserted into the pre-crack produced a crack along the interface, as shown in Fig. 80a. The two Al plates were separated after the test for 24 h and both sides showed the fracture surfaces as shown in Fig. 80b. It shows that the adhesive remains on one side of the Al plates, indicating failure along the interface. The initial crack, propagated after the insertion of the wedge, and the crack progressed under the high humidity condition are clearly distinguished on the fracture surface as shown in the upper plate of Fig. 80b. The surface created by the initial crack is glossy, while the surface produced after the crack propagation under a humid environment appears white and cloudy.

The three ROIs on the fracture surfaces were selected, as shown in Fig. 80b. Figure 80c shows the STEM-HAADF image, STEM-ELNES phase map, and STEM-EDX elemental map of the cross section of ROI-I, which was produced under the high-humidity condition. An oxide layer of 500 nm or more thickness is formed on the fracture surface. As mentioned in Sect. 6, the ELNES phase mapping allows us to distinguish aluminum oxide compounds by the ELNES of O K-edges in EELS. All the spectra included in the ROI are fitted with the O K-edges of $\text{Al}(\text{OH})_3$ and $\text{AlO}(\text{OH})$ as standard spectra. The distribution of the two compounds is obtained as a phase map according to the ratio of those compounds obtained by fitting. The obtained ELNES phase map (middle panel of Fig. 80c) shows that the oxide layer comprises two parts: the bottom part is $\text{Al}(\text{OH})_3$ -rich and the upper part is boehmite-rich. The STEM-EDX elemental map (right panel of Fig. 80c) indicates that the chlorine element is in the bottom part of the oxide layer.

The cross section of ROI-II, which is below the initial crack, shows different features compared to ROI-I. Even though ROI-II was exposed to the high-humidity environment, the oxide layer is not as thick as produced in ROI-I, which is close to the crack tip. And also, the two-layer structure with $\text{Al}(\text{OH})_3$ and boehmite as found in ROI-I was not formed and $\text{Al}(\text{OH})_3$ was produced less than the ROI-I. Chlorine element was also detected in this region but was not concentrated as much as ROI-I. ROI-III is the opposite part of ROI-I, where the adhesive layer is attached to the surface and no thick oxide layer is produced, as shown in Fig. 80e.

In the wedge test, water invaded mainly into the Al/epoxy interface at the crack tip and an extremely thick oxide layer was produced in 24 h. The STEM-ELNES mapping revealed that a two-component layer structure with $\text{Al}(\text{OH})_3$ and boehmite was formed with Cl-rich bottom $\text{Al}(\text{OH})_3$ part. It is indicated that corrosion is likely to occur at the highly stressed crack tip. The Al oxide layer can prevent corrosion, but bending stress applied to the oxide layer may destroy the oxide layer, and the metal part below is oxidized. We will investigate the detailed mechanism of this stress-induced corrosion.

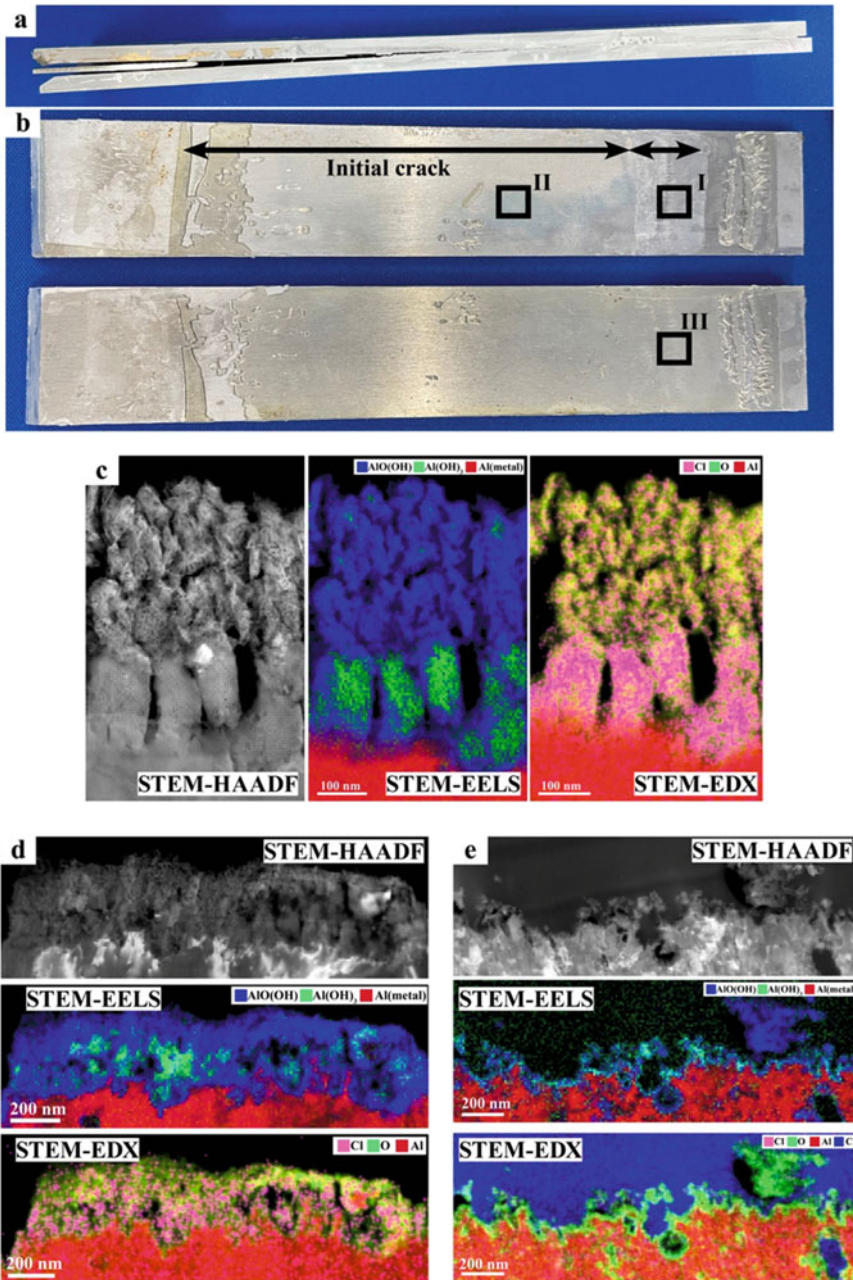


Fig. 80 Side view (a) and fracture surfaces (b) of the wedge-test specimen of the adhesive joint of Al exposed to 85 °C, 85%RH condition for 24 h. c, d, and e are cross-sectional images of the ROIs I, II, and III, respectively, marked in b. Each panel shows STEM-HAADF, STEM-ELNES phase map, and STEM-EDX elemental map

9 Concluding Remark

Polymer–polymer dissimilar interfaces formed via interdiffusion can be visualized and characterized by the elemental mapping and Image EELS techniques of EFTEM. The concentration profiles can estimate the interfacial thickness across the interfaces with a spatial resolution of 10 nm. The enthalpy-driven thermodynamic acceleration causes ultrafast interdiffusion in miscible polymer pairs. On the other hand, the interfacial diffusion between identical polymers is extremely slow because the diffusion between identical polymers is caused only by the contribution of combinatorial entropy change, which is relatively tiny for high molecular weight polymers.

The observation of the fracture surfaces by HR-SEM revealed that the failure of interfaces between polymers creates about 10 nm thick fibrils when they failed in the earlier diffusion stage. The nanofibrillar structure is formed when a thin interface is separated with the disentanglement of polymer chains before the initiation of crazing. This nanofibrillar surface feature is a signature of the failure of thin interfaces via “chain-pullout” and represents the entanglement structure at the interface. A similar nanofibrillar pattern on fracture surfaces is also found in the failure of the interfaces between metal and polymer. This indicates that an interfacial layer is formed with the low-molecular-weight polymer, and the entanglement structure within this layer determines the bonding strength. It was found that the interfacial toughness is determined by entanglement rather than thickness from the relationship between interfacial toughness and interface thickness.

Using STEM-EELS/ELNES, we clarified the chemical reaction at the Al adhesive interface with a resolution of 5 nm. We found that the main reason for the strong bonding is the diffusion of the adhesive molecules into tiny pores spaced about 10 nm on the aluminum oxide surface. This shows a similarity to polymer–polymer entanglement at the interface. The acid–base interaction between the amino moiety of the epoxy/amine adhesive and the hydroxyl unit on the Al oxide surface is the origin of the chemical bonding between Al and epoxy adhesive. This bond itself is weak and makes a small contribution to the increase in adhesive strength, but the enthalpic drive of acid–base interfacial interactions may cause spontaneous diffusion of adhesion molecules into the pores.

Acknowledgements SH thanks Mr. Hideki Hakukawa, Ms. Yuri Shigemto, Dr. Takeshi Hanada, Dr. Kazunori Kawasaki, Dr. Yida Liu, Dr. Lingyun Lyu (AIST), Prof. Yongjin Li (Hangzhou Normal University), and Prof. Yonggui Liao (Huazhong University of Science and Technology) for their contributions to the works. Part of this work was commissioned by JST-Mirai Program Grant Number JPMJMI18A2, Japan (Sects. 5, 6, and 7) and by the New Energy and Industrial Technology Development Organization (NEDO) Grant Number JPNP14014, Japan (Sect 8).

References

1. S.F. Edwards, Proc. Phys. Soc. **92**, 9–16 (1967)

2. P.G. de Gennes, *J. Chem. Phys.* **55**, 572–579 (1971)
3. F. Brochard, J. Jouffroy, P. Levinson, *Macromolecules* **16**, 1638–1641 (1983)
4. S. Horiuchi, Y. Ishii, *Polymer J.* **32**, 339–347 (2000)
5. T. Hayakawa, S. Horiuchi, *Angew. Chem. Int. Ed.* **42**, 2285–2289 (2003)
6. S. Horiuchi, T. Hanada, K. Yase, T. Ougizawa, *Macromolecules* **32**, 1312–1314 (1999)
7. S. Horiuchi, T. Hamanaka, T. Aoki, T. Miyakawa, T. Narita, H. Wakabayashi, *J. Electron Microsc.* **52**, 255–266 (2003)
8. L. Reimer, *Energy-Filtering Transmission Electron Microscopy*, 1st edn., ed. by L. Reimer (Springer, Berlin, 1995) pp. 347–400
9. N. Higashida, J. Kressler, S. Yukioka, T. Inoue, *Macromolecules* **25**, 5259–5262 (1992)
10. M.E. Fowler, J.W. Barlow, D.R. Paul, *Polymer* **28**, 1177–1184 (1987)
11. M. Suess, J. Kressler, H.W. Kammer, *Polymer* **28**, 957–960 (1987)
12. L. Reimer, *Energy-Filtering Transmission Electron Microscopy*, 1st edn., ed. by L. Reimer (Springer, Berlin, 1995) pp. 383–388
13. K.H. Körtje, *Scanning Microsc.* **8**, 22 (1994)
14. P.J. Thomas, P.A. Midgley, *Ultramicroscopy* **88**, 179–186 (2001)
15. S. Horiuchi, T. Fujita, T. Hayakawa, Y. Nakao, *Langmuir* **19**, 2963–2973 (2003)
16. S. Horiuchi, D. Yin, T. Ougizawa, *Macromol. Chem. Phys.* **206**, 725–731 (2005)
17. S. Horiuchi, D.H. Yin, Y.G. Liao, T. Ougizawa, *Macromol. Rapid Commun.* **28**, 915–921 (2007)
18. Y. Liao, A. Nakagawa, S. Horiuchi, T. Ougizawa, *Macromolecules* **40**, 7966–7972 (2007)
19. J. Kressler, N. Higashida, T. Inoue, W. Heckmann, F. Seitz, *Macromolecules* **26**, 2090–2094 (1993)
20. J. Klein, *Science* **250**, 640–646 (1990)
21. M.A. Parker, D. Vesely, *J. Polym. Sci. Polym. Phys.* **24**, 1869–1878 (1986)
22. H.C. Lin, I.F. Tsai, A.C.-M. Yang, M.S. Hsu, Y.C. Ling, *Macromolecules* **36**, 2464–2474 (2003)
23. P.E. Rouse, *J. Chem. Phys.* **21**, 1272–1280 (1953)
24. H. Qiu, M. Bousmina, *Macromolecules* **33**, 6588–6594 (2000)
25. E. Kim, E.J. Kramer, W.C. Wu, P.D. Garrett, *Polymer* **35**, 5706–5715 (1994)
26. S. Yukioka, K. Nagato, T. Inoue, *Polymer* **33**, 1171–1176 (1992)
27. S. Yukioka, T. Inoue, *Polym. Comm.* **32**, 17–19 (1991)
28. R. Schnell, M. Stamm, C. Creton, *Macromolecules* **32**, 3420–3425 (1999)
29. R. Schnell, M. Stamm, C. Creton, *Macromolecules* **31**, 2284–2292 (1998)
30. S. Wu, H.-K. Chung, *J. Polym. Sci. Polym. Phys.* **24**, 148–169 (1986)
31. L. Silvestri, H.R. Brown, S. Carrà, S. Carrà, *J. Chem. Phys.* **119**, 8140–8149 (2003)
32. P.J. Cole, R.F. Cook, C.W. Macosko, *Macromolecules* **36**, 2808–2815 (2003)
33. H.R. Brown, *J. Adhes.* **82**, 1013–1032 (2006)
34. J. Zhang, P.J. Cole, U. Nagpal, C.W. Macosko, *J. Adhes.* **82**, 887–902 (2006)
35. W.S. Gutowski, *J. Adhes.* **79**, 445–482 (2003)
36. S. Wu, *Polymer Interface and Adhesion* (Marcel Dekker: New York, 1982) p. 111
37. C. Creton, E.J. Kramer, C.Y. Hui, H.R. Brown, *Macromolecules* **25**, 3075–3088 (1992)
38. V. Janarthanan, R.S. Stein, P.D. Garret, *Macromolecules* **27**, 4855–4858 (1994)
39. A. Tanaka, *J. Electron Microsc.* **43**, 177–182 (1994)
40. D. Hull, *Fractography: Observing, Measuring and Interpreting Fracture Structure Topography* (Cambridge University Press, Cambridge, 1999) pp. 139–142
41. S. Horiuchi, A. Nakagawa, Y. Liao, T. Ougizawa, *Macromolecules* **41**, 8063–8071 (2008)
42. M. Stamm, S. Hüttenbach, G. Reiter, T. Spronger, *Europhys. Lett.* **14**, 451–456 (1991)
43. Z. Xu, N. Hadjichristidis, L.J. Fetters, J.W. Mays, *Adv. Polym. Sci.* **120**, 1–50 (1995)
44. S. Horiuchi, *Kobunshi Ronbunshu* **69**, 326–333 (2012)
45. M. Yamazaki, *J. Mol. Catal. A: Chem.* **213**, 81–87 (2004)
46. Y.J. Kim, Y. Taniguchi, K. Murase, Y. Taguchi, H. Sugimura, *App. Surface Sci.* **255**, 3648–3654 (2009)

47. Y. Taguchi, Y.J. Kim, M. Hagioi, Y. Taniguchi, H. Sugimura, *Hyoumen Gijutsu* **65**, 234–239 (2014)
48. S. Horiuchi, H. Hakukawa, Y. Jong Kim, H. Nagata, H. Sugimura, *Polym. J.* **48**, 473–479 (2016).
49. T. Sato, H. Akiyama, S. Horiuchi, T. Miyamae, *Surf. Sci.* **677**, 93–98 (2018)
50. T. Sato, S. Ise, S. Horiuchi, H. Akiyama, T. Miyamae, *Int. J. Adhe. Adhes.* **93**, 102322–102322 (2019)
51. M.F. Sonnenschein, S.P. Webb, P.E. Kastl, D.J. Arriola, B.L. Wendt, D.R. Harrington, *Macromolecules* **37**, 7974–7978 (2004)
52. O.R. Wilson, D.J. Borrelli, A.J.W. Magenau, *ACS Omega* **7**, 28636–28645 (2022)
53. Y. Liu, Y. Shigemoto, T. Hanada, T. Miyamae, K. Kawasaki, S. Horiuchi, *A.C.S. Appl. Mater. Interfaces* **13**, 11497–11506 (2021)
54. H. Leidheiser, P.D. Deck, *Science* **241**, 1176–1181 (1988)
55. J. Cognard, *Inter. J. Adhe. Adhes.* **11**, 114–116 (1991)
56. B.A. Calderón, J. Soule, M.J. Sobkowicz, *J. Appl. Polym. Sci.* **136**, 47553 (2019)
57. Z. Qiu, T. Ikehara, T. Nishi, *Polymer* **44**, 2799–2806 (2003)
58. International Standardization Organization. *ISO11339: 2010: Adhesives-T-peel test for flexible-to-flexible bonded assemblies* (2010)
59. R.F. Egerton, P. Li, M. Malac, *Micron* **35**, 399–409 (2004)
60. N.J. Severs, *Nat. Protoc.* **2**, 547–576 (2007)
61. G.H. Michler, *Electron Microscopy of Polymers* (Springer, Berlin, 2008), pp.165–171
62. Y. Chen, T. Gan, C. Ma, L. Wang, G., *J. Phys. Chem. B*, **120**, 4715–4722 (2016)
63. Q. Liu, X. Sun, H. Li, S. Yan, *Polymer* **54**, 4404–4421 (2013)
64. K. Uchida, K. Mita, Y. Higaki, K. Kojio, A. Takahara, *Polymer J.* **51**, 183–188 (2019)
65. S. Horiuchi, Y. Liu, Y. Shigemoto, T. Hanada, *Mater. Today Commun.* **36**, 106637 (2023)
66. W.P. King, T.W. Kenny, K.E. Goodson, G. Cross, M. Despont, U. Dürig, H. Rothuizen, G.K. Binnig, *P. Vettiger, Appl. Phys. Lett.* **78**, 1300–1302 (2001)
67. F. Tang, P. Bao, A. Roy, Y. Wang, Z. Su, *Polymer* **142**, 155–163 (2018)
68. J. Zähr, S. Oswald, M. Türpe, H.J. Ullrich, U. Füssel, *Vacuum* **86**, 1216–1219 (2012)
69. S. Horiuchi, Y. Liu, T. Hanada, H. Akiyama, *Appl. Surf. Sci.* **599**, 153964 (2022)
70. A. Strålin, T. Hjertberg, *Appl. Surf. Sci.* **74**, 263–275 (1994)
71. A.N. Rider, *J. Adh. Sci. Tech.* **15**, 395–422 (2001)
72. R. Leapman, *EELS Quantitative Analysis*, C.C. Ahn, ed., *Transmission Electron Energy Loss Spectrometry in Materials Science and the EELS ATLAS*, Wiley-VCH (Weinheim, Germany, 2004) pp. 49–96
73. R. Arenal, F. de la Peña, O. Stéphan, M. Walls, M. Tencé, A. Louseau, C. Colliex, *Ultramicroscopy* **109**, 32–38 (2008)
74. J. Scott, P.J. Thomas, M. MacKenzie, S. McFadzean, J. Wilbrink, A.J. Craven, W.A.P. Nicholson, *Ultramicroscopy* **108**, 1586–1594 (2008)
75. J. Bobynko, I. Maclaren, A.J. Craven, *Ultramicroscopy* **149**, 9–20 (2015)
76. R. Brydson, H. Sauer, W. Engel, In *Transmission Electron Energy Loss Spectrometry in Materials Science and the EELS ATLAS*, C.C. Ahn, ed., (Wiley-VCH, Weinheim, Germany, 2004) pp 223–270
77. R.U. Din, K. Piotrowska, V.C. Gudla, M.S. Jellesen, R. Ambat, *Appl. Surf. Sci.* **355**, 820–831 (2015)
78. S. Horiuchi, N. Terasaki, M. Itabashi, *Manuf., Rev.* **7**, 11 (2020)
79. K. Kimoto, K. Ishizuka, T. Mizoguchi, I. Tanaka, Y. Matsui, *J. Electron Microsc.* **52**, 299–303 (2003)
80. K. Wapner, M. Stratmann, G. Grundmeier, *Inter. J. Adhe. Adhes.* **28**, 59–70 (2007)
81. A. Kurian, S. Prasad, A. Dhinojwala, *Langmuir* **26**, 17804–17807 (2018)
82. D. Wang, T.P. Russell, T. Nishi, K. Nakajima, *ACS Macro Lett.* **2**, 757–760 (2013)
83. Y. Liao, M.J. Peng, F.Z. Liu, X.L. Xie, *Chinese. J. Polym. Sci.* **31**, 870–878 (2013)
84. K. Akaike, Y. Shimoi, S. Horiuchi, *Langmuir* **39**, 10625–10637 (2023)

85. L. Lyu, Y. Ohnuma, Y. Shigemoto, T. Hanada, T. Fukada, H. Akiyama, N. Terasaki, S. Horiuchi, *Langmuir* **36**, 14046–14057 (2020)
86. R.J. Good, In *Contact Angle, Wettability and Adhesion*, K.L. Mittal, ed. Utrecht, Vol. 3 (1993)
87. J. Washiyama, E.J. Kramer, C.-Y. Hui, *Macromolecules* **26**, 2928–2934 (1993)
88. C. Creton, H.R. Brown, V.R. Deline, *Macromolecules* **27**, 1774–1780 (1994)
89. <https://taiseiplas.jp/nmt/> (accessed 2023–01–28)
90. S. Horiuchi, T. Hanada, T. Miyamae, T. Ymanaka, K. Osumi, N. Ando, M. Naritomi, *J. Adhesion Soc. Japn.* **48**, 322–330 (2012)
91. Composite material of aluminum alloy and resin and production method therefore. Inventors: M. Naritomi, N. Ando, M. Takahashi and M. Shiraishi, EP1459882A1. 2004–09–22
92. International Standardization Organization. *ISO19095:2015: Plastics-Evaluation of the adhesion interface performance in plastic-metal assemblies* (2015)
93. S. Horiuchi, Y. Liu, Y. Shigemoto, T. Hanada, K. Shimamoto, *Inter. J. Adh. Adhes.*, **117**, Part B, 103003 (2022)
94. International Standardization Organization. *ISO 13586:2018: Plastics—Determination of fracture toughness (G_{IC} and K_{IC})—Linear elastic fracture mechanics (LEFM) approach* (2018)
95. S.-S. Yao, F.-L. Jin, K.Y. Rhee, D. Hui, S.-J. Park, *Compos. Part B Eng.* **142**, 241–250 (2018)
96. K. Stoeffler, S. Andjelic, N. Legros, J. Roberge, S.B. Schougaard, *Compos. Sci. Technol.* **84**, 65–71 (2013)
97. B.A. Alshammari, M.S. Alsuhybani, A.M. Almushaikeh, B.M. Alotaibi, A.M. Alenad, N.B. Alqahtani, A.G. Alharbi, *Polymers* **13**, 2474 (2021). <https://doi.org/10.3390/polym13152474>
98. T. Ishikawa, K. Amaoka, Y. Masubuchi, T. Yamamoto, A. Yamanaka, M. Arai, J. Takahashi, *Compos. Sci. Technol.* **155**, 221–246 (2018)
99. M.D. Banea, L.F.M. Da Silva, *Proc. Inst. Mech. Eng.*, L. **223**, 1–18 (2009)
100. M.D. Banea, M. Rosioara, R.J.C. Carbas, L.F.M. Da Silva, *Compos. Part B: Eng.* **151**, 71–77 (2018)
101. O. Haga, H. Koyama, K. Kawada, *Adv. Compos. Mater.* **5**, 139–149 (1996)
102. P. Molitor, V. Barron, T. Young, *Int. J. Adhes. Adhes.* **21**, 129–136 (2001)
103. E.H. Andrews, A.J. Kinloch, *Proc. R. Soc. London. A. Math. Phys. Sci.* **332**, 401–414 (1973)
104. E.H. Andrews, A.J. Kinloch, *Proc. R. Soc. London. A. Math. Phys. Sci.* **332**, 385–399 (1973)
105. B.R.K. Blackman, In *Testing Adhesive Joints*, L.F.M. Da Silva, D.A. Dillard, etc., eds., Wiley-VCH, Weinheim Germany, **12**, p 55–62 (2012)
106. B.R.K. Blackman, *Quasi-Static Fracture Tests. Testing Adhesive Joints*. Eds. by L.F.M. Da Silva, D.A. Dillard, B.R.K Blackman, R.D. Adams, (Wiley-VCH, Weinheim Germany, 2012) pp 169–172
107. F. Xiao, C.Y. Hui, E.J. Kramer, *J. Mater. Sci.* **28**, 5620–5629 (1993)
108. International Standardization Organization. *ISO 25217:2009: Adhesives-Determination of the mode I adhesive fracture energy of structural adhesive joints using double cantilever beam and tapered double cantilever beam specimens* (2009)
109. N. Terasaki, Y. Fujio, S. Horiuchi, H. Akiyama, *Int. J. Adh. Adhes.* **93**, 102328 (2019)
110. V. Tvergaard, J.W. Hutchinson, *J. Mech. Phys. Solids* **40**, 1377–1397 (1992)
111. C.M. Johnson, E. Tyrode, S. Baldelli, M.W. Rutland, C. Leygraf, *J. Phys. Chem. B* **109**, 321–328 (2005)
112. P. Supaphol, C. Mit-uppatham, M. Nithianakul, *Macromol. Mater. Eng.* **290**, 933–942 (2005)
113. K. Sensui, T. Tarui, T. Miyamae, C. Sato, *Chem. Commun.* **55**, 14833–14836 (2019)

Open Access This chapter is licensed under the terms of the Creative Commons Attribution 4.0 International License (<http://creativecommons.org/licenses/by/4.0/>), which permits use, sharing, adaptation, distribution and reproduction in any medium or format, as long as you give appropriate credit to the original author(s) and the source, provide a link to the Creative Commons license and indicate if changes were made.

The images or other third party material in this chapter are included in the chapter's Creative Commons license, unless indicated otherwise in a credit line to the material. If material is not included in the chapter's Creative Commons license and your intended use is not permitted by statutory regulation or exceeds the permitted use, you will need to obtain permission directly from the copyright holder.

